UNIVERSIDADE FEDERAL DO AMAZONAS
PRÓ-REITORIA DE PESQUISA E PÓS-GRADUAÇÃO
PROGRAMA DE PÓS-GRADUAÇÃO EM FÍSICA

EDUARDO DA SILVA CARVALHO

QUANTUM-CHEMICAL INVESTIGATION ON THE PRE-NUCLEATION CLUSTER FORMATION BETWEEN OXALIC ACID CONFORMERS AND ATMOSPHERIC NUCLEATION PRECURSORS

MANAUS/AM
2024

EDUARDO DA SILVA CARVALHO

QUANTUM-CHEMICAL INVESTIGATION ON THE PRE-NUCLEATION CLUSTER FORMATION BETWEEN OXALIC ACID CONFORMERS AND ATMOSPHERIC NUCLEATION PRECURSORS

Dissertation presented to the Graduate Program in Physics at the Federal University of Amazonas as a partial fulfillment of the requirements to obtain the title of Master in Physics.

Advisor: Prof. Dr. Puspitapallab Chaudhuri

MANAUS/AM
2024

Ficha Catalográfica

Ficha catalográfica elaborada automaticamente de acordo com os dados fornecidos pelo(a) autor(a).

C331q Carvalho, Eduardo da Silva
Quantum-chemical investigation on the pre-nucleation cluster formation between oxalic acid conformers and atmospheric nucleation precursors / Eduardo da Silva Carvalho . 2024
80 f.: il. color; 31 cm.

Orientador: Puspitapallab Chaudhuri
Dissertação (Mestrado em Física) - Universidade Federal do Amazonas.

1. oxalic acid. 2. hydrogen bond. 3. dft. 4. molecular cluster. I. Chaudhuri, Puspitapallab. II. Universidade Federal do Amazonas III. Título

ACKNOWLEDGMENTS

I would like to express my deepest gratitude to my parents, Antonia da Silva and Francisco Carvalho, who raised me with humility and wisdom, always encouraging me to pursue my studies. Their unwavering support throughout this journey has been critical in helping me stay strong and focused on my goals. I extend my sincere thanks to my wife, Iasmim Veiga, whose constant encouragement kept me going and whose support was vital in making this work possible.

I am also immensely grateful to the professors who have contributed to my education thus far. I have had the privilege of learning from many brilliant minds, but I would especially like to acknowledge Dr. Puspitapallab Chaudhuri. His dedication to the development and sharing of knowledge, combined with his seriousness, patience, and constant support, have greatly influenced my academic growth during these more than two years of work.

Finally, I acknowledge the financial support provided to the Graduate Program in Physics at UFAM by the CAPES, CNPQ, and FAPEAM foundations.

RESUMO

Partículas de aerossol formadas na troposfera terrestre através do processo de nucleação têm um grande impacto no balanço radiativo do planeta, na formação de nuvens e nos padrões de precipitação. As crescentes preocupações com as mudanças climáticas em diferentes partes do mundo servem como motivação para a comunidade científica estudar os processos de formação e as propriedades físico-químicas dos aerossóis atmosféricos. O ácido oxálico é um dos ácidos dicarboxílicos mais simples e naturalmente presentes na atmosfera, sendo encontrado em abundância e apresentando vários conformações estruturais estáveis. As interações do ácido oxálico, mediadas por ligações de hidrogênio, com outras moléculas atmosféricas são importantes, pois podem influenciar a composição química da atmosfera, impactando assim a físico-química atmosférica e os processos ambientais. Neste trabalho, realizamos cálculos de Teoria do Funcional da Densidade com o modelo M06-2X/6-311++G(3df,3pd) para examinar a interação de diferentes conformações do ácido oxálico com ácido sulfúrico e amônia — duas moléculas amplamente reconhecidas como precursoras da nucleação atmosférica — com o objetivo de observar as características das ligação de hidrogênio das conformações individuais. Uma extensa e sistemática análise químico-quântica foi conduzida para analisar as características estruturais, termodinâmicas, elétricas e espectroscópicas de vários aglomerados binários e ternários mediados por cinco conformações do ácido oxálico. Nossa análise das energias de ligação eletrônica e das variações na energia livre associadas à formação de aglomerados e sua distribuição populacional em temperatura ambiente revela que múltiplas conformações do ácido oxálico têm potencial para formar aglomerados estáveis na atmosfera. De fato, a conformação de ácido oxálico de maior energia contribui de forma mais significativa para a distribuição populacional dos aglomerados. De acordo com os cálculos realizados, os aglomerados de ácido oxálico com ácido sulfúrico apresentam maior estabilidade termodinâmica e maior intensidade de espalhamento de luz em comparação com aqueles formados com amônia. Além disso, a análise da formação sucessiva de aglomerados revela que os aglomerados formados entre o ácido sulfúrico e o ácido oxálico têm maior probabilidade de crescer espontaneamente do que aqueles formados entre a amônia e o ácido oxálico.

Palavras-chave: ácido oxálico, ligação de hidrogênio, DFT, molecular cluster.

ABSTRACT

Aerosol particles formed in the Earth's troposphere through the nucleation process have large impact on the planet's radiative balance, cloud formation and precipitation patterns. The growing concerns about the climate change occurring in different parts of the world serve as a motivation for the scientific community to study the formation processes and physicochemical properties of atmospheric aerosols. Oxalic acid is one of the simplest naturally occurring dicarboxylic acid that is abundantly found in the atmosphere, and it has several stable structural conformers. Hydrogen-bonded interactions of oxalic acid with other atmospheric molecules are important as they might influence the chemical composition of the atmosphere, thereby impacting atmospheric chemistry and environmental processes. In this work, we used Density Functional calculations with the M06-2X/6-311++G(3df,3pd) model to examine the interaction of different oxalic acid conformers with sulfuric acid and ammonia — two widely recognized atmospheric nucleation precursor molecules — with the aim of observing the hydrogen bonding characteristics of the conformers individually. An extensive and systematic quantum-chemical calculation has been conducted to analyze the structural, thermodynamical, electrical, and spectroscopic characteristics of several binary and ternary clusters mediated by five oxalic acid conformers. Our analysis of the electronic binding energies and free energy changes associated with the formation of clusters and its population distribution at ambient temperature reveals that multiple conformations of oxalic acid have the potential to engage in stable cluster formation in the atmosphere. In fact, the highest energy oxalic acid conformer contributes most significantly to the population distribution of the clusters. According to the present calculations, clusters of oxalic acid with sulfuric acid demonstrate greater thermodynamic stability, a higher probability of formation, and more intense light scattering compared to clusters with ammonia. Furthermore, the analysis of successive cluster formation reveals that clusters formed between sulfuric acid and oxalic acid are more likely to grow spontaneously than those formed between ammonia and oxalic acid.

Keywords: Oxalic acid, hydrogen bond, DFT, molecular cluster.

LISTA DE FIGURAS

LISTA DE TABELAS

LIST OF ABBREVIATIONS

AM	Ammonia
ANP	Atmospheric Nucleation Precursors
CCN	Cloud Condensation Nucleus
CLOUD	Cosmics Leaving Outdoor Droplets
CERN	European Council for Nuclear Research
DCA	Dicarboxylic Acid
DFT	Density Functional Theory
DZ	Double-Zeta
ESE	Electronic Spatial Extent
GGA	Generalized Gradient Approximation
GTO	Gaussian-Type Orbital
GWP	Global Warming Potential
HB	Hydrogen Bond
IPCC	Intergovernmental Panel on Climate Change
LDA	Local Density Approximation
NPF	New Particle Formation
OA	Oxalic Acid
PD	Proton Donor
SA	Sulfuric Acid
TZ	Triple-Zeta
ZPE	Zero-point Energy

CONTENTS

1 INTRODUCTION

Climate change is increasingly recognized as a serious threat to life on Earth, particularly, to humanity. The growing frequency and severity of unlikely and extreme weather events, such as hurricanes, wildfires, droughts, heatwaves and floods, along with shifting ecosystems and rising sea levels, over the last few decades in different parts of the world, have become great concern for the human society. This escalating crisis is compounded by the ever-growing world population, which intensifies demand for resources, leading to rapid worldwide industrial growth. This growth, in turn, contributes significantly to deforestation, a practice that not only destroys vital carbon sinks but also releases large amounts of stored carbon into the atmosphere, leading to global warming. Industrial activities further contribute to carbon emissions and other pollutants, driving up greenhouse gas concentrations and worsening the problem.

As climate disasters are multiplying across the globe, the scientific community has reached a strong consensus that the increase in extreme weather events is directly linked to anthropogenic actions [1-4]. Despite the clear scientific consensus, as highlighted by the Intergovernmental Panel on Climate Change (IPCC) in its 2021 report [5], human activities continue to heat the atmosphere, ocean, and land at an alarming rate. Despite the IPCC's findings emphasizing the significant human impact on climate change and the increasing calls from an informed society for urgent action, it seems that the implementation of effective public policies to address this damage remains insufficient [1,6,7]. Many policymakers who are expected to prioritize climate change in their political agenda, often display an unexpected reluctance to do so [1]. The rapid pace of industrialization, particularly in developing nations, often puts a barrier to the implementation of environmental safeguards, leading to unchecked emissions and environmental degradation.

As the IPCC warns, the climate crisis is no more a distant future threat but a current and worsening reality, with the potential for catastrophic impacts if not addressed promptly. Addressing the escalating climate crisis requires a collective effort from all sectors of society with better and improved policy decisions and governance practices. While the politicians are expected to develop and enforce adequate environmental policies, general population must take responsibility of creating public awareness and individual actions to combat climate change. Scientists, on the other hand, have the mission to understand the causal factors that include mechanisms behind pollution accumulation, aerosol formation, transport of pollutants, atmospheric chemical reactions and the complex intermolecular interactions between atmospheric molecules. This involves both observational studies at the macroscopic level and theoretical modeling to explore these phenomena at a microscopic level. Scientific investigations are often important for developing effective strategies to mitigate the impact of pollutants and guide policymakers in making informed decisions that protect the environment and public health.

In fact, the role of atmospheric aerosols is an important issue in the context of climate change discussed above, as the contribute to both global cooling and global warming, often masking one effect with another, regardless of whether they originate from natural sources or human activities. Formation of secondary aerosol in the atmosphere serves as a strong motivation behind the theoretical investigation conducted and reported in this dissertation. Before going into the analysis of results, a brief description of some related concepts are given below to provide context for the work.

1.1 The Climate System

Earth's climate system consists of the atmosphere, oceans, land and cryosphere with the atmosphere is the most volatile component. the atmosphere corresponds to the layer of air that surrounds the entire planet, crucial for sustaining life. It is estimated to have originated approximately four billion years ago and is believed to have developed after the emission of volatile compounds that were trapped on the planet. When these gases, including water vapor and other elements from the Earth's interior, emerged, a portion dissipated into space, however, a significant amount remained bound to the planet due to its gravitational pull. [8].

The primitive atmosphere lacked gases like oxygen (O_2) and was mainly composed of carbon dioxide (CO_2), nitrogen (N_2), water vapor, methane (CH_4), ammonia (NH_3), and traces of other gases. Over time, water vapor condensed to form oceans, and a substantial amount of CO_2, by dissolving in these oceans, formed sedimentary rocks. N_2, being inert, became the atmosphere's dominant component. Oxygen levels began to rise around 2.3 billion years ago, likely due to photosynthesis by emerging cyanobacteria and other primitive organisms. The atmosphere's current composition, established about 65 million years ago, is mainly composed of N_2 (78%), followed by O_2 (21%), and Argon (1%). Water vapor constitutes another significant component, predominantly located in the lower atmosphere (troposphere), where its concentration fluctuates due to evaporation and precipitation, varying notably and occasionally reaching levels of up to 5%. The other gaseous constituents, called trace gases, represent less than 1% of the atmosphere [8-10] and include a wide variety of compounds, such as carbon dioxide (CO_2), methane (CH_4), ozone (O_3), and numerous volatile organic compounds (VOCs). These VOCs are a significant subset of trace gases and consist of organic molecules like alkanes, alkenes, aldehydes, ketones, and carboxylic acids, which play crucial roles in atmospheric chemistry, particularly in the formation of secondary organic aerosols (SOAs) and ozone. Their presence and reactivity can influence the formation of secondary organic aerosols (SOAs), which are critical in cloud condensation nuclei (CCN) formation and thus, impact weather patterns and climate dynamics [11-15]. The interactions of these organic molecules with other atmospheric components, such as nitrogen oxides and sulfur dioxide, contribute to complex chemical reactions that affect air quality and the global climate.

1.2 Atmospheric Aerosols and Radiation Balance

Aerosols are particles found in a gaseous medium, existing in both solid and/or liquid phases. These particles are dispersed across the troposphere and have in shaping the quality of terrestrial life. Atmospheric aerosols exert influence on regional and global climates through direct participation in the radiation balance - either by scattering or absorbing solar radiation — or indirectly, by serving as cloud condensation nuclei (CCN), influencing cloud albedo, precipitation patterns and consequently in the hydrological cycle [16-18].

Aerosols, depending on their chemical composition, can either scatter or absorb solar radiation. Overall, they exhibit negative radiative forcing, which generally leads to a cooling effect on the Earth's surface. This is a direct influence of aerosols on the radiation balance. The optical characteristics of clouds are linked to the sizes and quantities of droplets constituting them, which are, in turn, governed by the availability of atmospheric particles that serve as CCN. The increase of atmospheric aerosols resulting from anthropogenic emissions results in the formation of smaller cloud droplets. This occurs because the same volume of water vapor is distributed among a greater number of CCNs. A cloud characterized by a greater quantity of smaller-sized droplets exhibits a higher albedo compared to one with fewer but larger droplets. This increased albedo implies enhanced reflectivity, causing a greater proportion of incident sunlight to be redirected back into space, resulting in reduced solar radiation reaching the Earth's surface. This phenomenon illustrates the indirect influence of aerosols on the radiation balance [19-21].

Because of their qualitative characteristics and quantitative importance in the atmosphere, aerosols remain one of the primary pollutants monitored by air quality measurement networks. Carbonaceous aerosols are also associated with the darkening of monuments due to the deposition of soot and a reduction in visibility [18]. Ultrafine aerosol particles raise concerns for public health due to their ease of transport through the air and ability to enter the respiratory system. Prolonged exposure to these particles can induce lung inflammation, potentially leading to conditions such as lung cancer and cardiovascular disease, thereby increasing mortality rates [22-24].

Aerosols are mixtures of materials originating from various sources, exhibiting diverse chemical compositions, sizes, and shapes. Their classification remains highly complicated, and even today, predicting the exact mechanism of their formation presents a scientific challenge. In **Figure 1**, images of industrially derived aerosols, captured by an electron microscope, highlight the multitude of sizes and shapes among particles of similar origin.

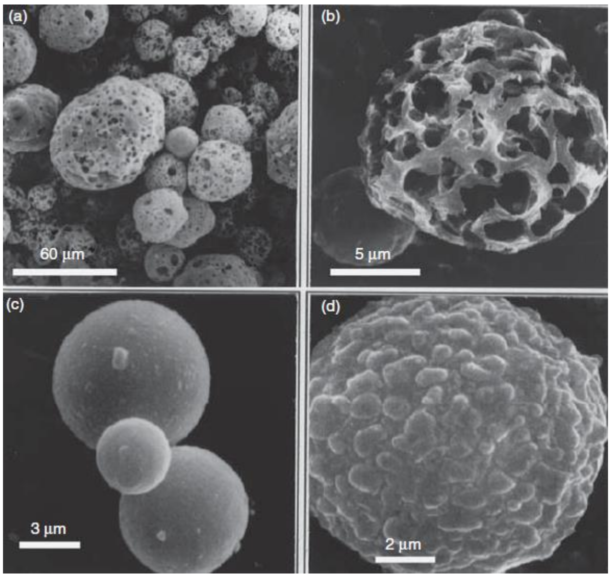

Figure 1: Electron microscope images of industrial particle aerosols: (a, b) particles formed from oil fuel combustion, (c) soot particles from coal combustion, and (d) particles from distillate oil combustion [adapted from Ref. 17].

Atmospheric aerosols can be classified into two main categories based on their origin and formation process: primary and secondary aerosols. Primary aerosols are directly emitted into the atmosphere from various natural and human activities, such as combustion processes, volcanic eruptions, forest fires, industrial emissions, and biological materials. These particles enter the atmosphere in their final form. Secondary aerosols, on the other hand, are not directly emitted. Instead, they form in the atmosphere through chemical reactions, involving the aggregation, nucleation, and condensation of gaseous compounds that transform into particulate matter. These secondary processes are key in creating aerosols from gases that originally existed in the atmosphere.

1.3 Secondary Aerosol Formation

The process of secondary aerosol formation in the atmosphere may be considered to occur in two different stages - pre-nucleation and nucleation. The pre-nucleation stage involves the initial steps where gas-phase molecules undergo reactions, such as oxidation, leading to the formation of low-volatility products. These products often include organic molecules and sulfuric acid that have a propensity to cluster together due to intermolecular forces like hydrogen bonding and van der Waals interactions. At this stage, the clusters formed are relatively small and may not yet be stable enough to grow into larger particles. They are in a dynamic equilibrium with the surrounding gas phase, constantly forming and dissociating. However, the pre-nucleation stage is critical because it sets the conditions for the actual nucleation event. The concentration of low-volatility compounds, temperature, and humidity can influence whether these initial clusters can grow or evaporate back into the gas phase.

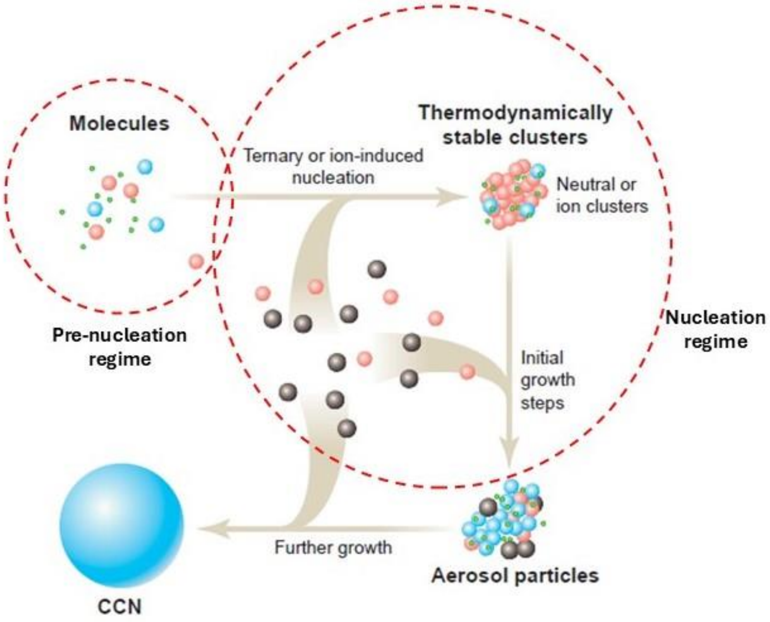

Figure 2: Formation of aerosol particles in the atmosphere [adapted from Ref. 16].

Nucleation is the process by which a critical cluster size is reached, leading to the formation of stable particles that can grow by the condensation of additional gas-phase molecules. Once a cluster reaches this critical size, it can overcome the energy barrier associated with nucleation, making it less likely to evaporate. This leads to the formation of new particles, which are the embryos of secondary aerosols, as illustrated on **Figure 2**. The nucleation process is essential for the new particle formation (NPF) in the atmosphere, which can grow into larger aerosols that impact climate and air quality. Depending on their chemical compositions and local concentrations, these clusters can reach a size range of 50-100 nm in diameter, a particularly important size from a climatic perspective, as they can serve as CCNs [25-28].

The molecules that usually participate in the nucleation process are known as Atmospheric Nucleation Precursors (ANPs). Sulfuric acid, water and atmospheric base molecules such as ammonia, and amines (methylamine, dimethylamine and trimethylamine) are widely recognized as the basic ANPs in terrestrial atmosphere. It is predicted that up to 50% of secondary atmospheric aerosol particles arise from nucleation, but the initial chemical and physical processes of the pre-nucleation stage when certain atmospheric molecules start interacting and form clusters in the gas phase, are still poorly understood [21-23]. In fact, the early stages of particle formation, particularly for electrically neutral molecular clusters, are incredibly challenging to observe directly using experimental methods mainly due to their small size and transient nature [29-32]. In this context, gas-phase quantum-chemical investigations on the intermolecular interactions of small molecular clusters become important as they can give detailed information about the structures, nature of interaction, in particular hydrogen bonding and relative stabilities of the clusters, which can be used in the direct modeling of the particle formation processes.

The importance of organic molecules in NPF is another relevant issue in the mechanism of secondary aerosol formation which has generated some debate within the scientific community [15]. Some early investigations, performed during 2000-2010, showed that organic acid molecules could be involved in the initial particle formation process, and, in fact, they could drastically enhance sulfuric acid-driven NPF in the atmosphere [11, 32-37]. Some controlled laboratory experiments (chamber experiments), performed during the same period, demonstrated gas phase oxidation of volatile organic compounds, particularly of monoterpenes, contribute to the formation and growth of atmospheric aerosol and might also be important for SA-driven NPF [15, 38-42]. In the subsequent years, many theoretical and experimental investigations were conducted to observe the role of organic compounds in the process of atmospheric NPF [42-61]. Several monocarboxylic compounds like benzoic acid [56-58], formic acid [58-60], methanesulfonic acid [61-66], lactic acid [66] and the dicarboxylic ones such as oxalic acids [55, 58, 67-69], maleic acids [58, 70], succinic acid [58, 70, 71], malonic acid [58, 70], Phthalic acid [70] were investigated by theoretical quantum-chemical procedures considering hydrogen-bonded interaction of these organic molecules com ANPs like sulfuric acid, ammonia and amines, both in the context of pre-nucleation and nucleation regimes. Hydrogen bonding interactions play a crucial role in aerosol formation, influencing both the pre-nucleation and nucleation regimes, helping in stabilizing small molecular clusters and facilitating their growth into larger clusters.

1.4 Hydrogen Bond

Hydrogen bonding interactions among organic molecules are of great importance in many different branches of chemical sciences such as biochemistry and molecular biology, medicinal chemistry and drug designing, materials science/polymer chemistry, astrochemistry, atmospheric chemistry and so on. The nature of hydrogen bonds (HBs) may directly influence the stability of molecular structures, reactivities, and functions. In living organisms HBs are fundamental in maintaining the secondary and tertiary structures of biomolecules such as proteins and nucleic acids. Understanding HBs is crucial in materials science for designing and manipulating the properties of polymers, supramolecular assemblies, and other advanced materials. In the atmosphere, organic compounds such as carboxylic acids can interact with other molecules via hydrogen bonding to form small stable clusters. These clusters can grow in size and eventually lead to the formation of secondary organic aerosols.

A hydrogen bond refers to an attractive interaction involving a hydrogen atom from a molecule or a molecular fragment with the formula X-H, where X is more electronegative than hydrogen. This interaction occurs with an atom or a group of atoms within the same molecule or in a different molecule, in which there is evidence of bond formation. A typical representation of a hydrogen bond can be expressed as X-H···Y-Z, where the three dots indicate the bond. Here, X-H is the donor of the hydrogen bond, and Y is the acceptor, which can be an atom, an anion, a molecular fragment, or even a Y-Z molecule, where Y is linked to Z [69].

In traditional hydrogen bonds, both X and Y are electronegative atoms such as Oxygen, Nitrogen, or Fluorine, and in some cases, X and Y can be identical. Typically, hydrogen bonds form when the electronegativity of X relative to H in the X-H covalent bond is such that the electron of H is strongly attracted towards X, leading to the partial deprotection of the proton of H. This establishes conditions for the interaction of the donor atom with it. For the acceptor Y to interact with the donor X-H, Y must possess lone pair electrons (a pair of valence electrons without bonding or sharing with other atoms) or polarizable π electrons [70].

Hydrogen bonds range from very strong, comparable to covalent bonds, to very weak, compared to van der Waals forces. Table 1 displays typical properties of different types of hydrogen bonds, classified as strong, medium and weak. The formation of hydrogen bonds typically results in an elongation of the bond length X-H, causing a red shift in the infrared stretching frequency and an elevation in the infrared absorption cross-section for the stretching vibration of X-H. The strength of the hydrogen bond H⋯Y increases with greater elongation of X-H in X-H⋯Y-Z [70].

Table 1: Classification of hydrogen bonds [70].

PARAMETER	STRONG	INTERMEDIATE	WEAK
Bond length X − H	~1.2-1.5 Å	~1.5-2.2 Å	~2.2-3.2 Å
Bond length H ⋯ Y	2.2-2.5 Å	2.5-3.2 Å	3.2-4.0 Å
Bond angle X− H ⋯ Y	175-180°	130-180°	90-150°
Bond energy	14-40 kcal/mol	< 14 kcal/mol	< 4 kcal/mol
Vibrational frequency change X− H	25%	10%-25%	< 10%

2 OBJECTIVES

2.1 General Objective

The principal objective of the present study is to explore the structural, thermochemical, electrical, and spectroscopic properties of hydrogen-bonded molecular clusters formed by different structural conformations of oxalic acid (OA) with Sulfuric Acid (SA) and Ammonia (AM) utilizing techniques of computational quantum chemistry. This research is conducted within the context of pre-nucleation stage of atmospheric aerosol formation, giving particular attention to the nature of hydrogen bonding of each OA conformer individually.

2.2 Specific Objectives

- Identify and characterize the potential stable conformations of the isolated oxalic acid molecule, following existing literature and optimize the molecular structures by a suitable quantum chemical model based on DFT.
- Identify the potential configurations of binary molecular clusters formed by each oxalic acid conformation with either an ammonia or a sulfuric acid molecule using semi-empirical methods and optimize the geometries using DFT model.
- Identify and optimize the possible configurations of ternary molecular clusters formed by each oxalic acid conformation with either two ammonia molecules or two sulfuric acid molecules.
- Characterize the hydrogen bonds stabilizing the clusters using structural and spectroscopic criteria;
- Analyze the energetics and electric parameters of the clusters, calculated by the DFT method, in the context of atmospheric pre-nucleation interactions;

3 METHODOLOGY

In this study, we will explore how key molecular properties, such as binding energy, average polarizability, polarizability anisotropy, and related Rayleigh parameters, change in response to interactions with their surroundings. Given that we are focusing on molecules and molecular clusters, which are microscopic systems, it is essential to describe them using quantum mechanics. This involves formulating the many-body Schrödinger equation and finding its solution. To address this, we employ Density Functional Theory (DFT) to solve the multi-electron Schrödinger equation and subsequently determine the properties of interest.

3.1 Density Functional Theory

Density Functional Theory is a computational quantum mechanical method widely used to investigate the electronic structure of atoms, molecules, and solids. The method is favored in various fields such as physics, chemistry, and materials science due to its efficiency and ability to provide accurate results for many systems. DFT is built on the principle that all properties of a many-electron system can be determined by its electron density, $\rho(\vec{r})$, rather than the many-body wavefunction $\Psi(\overrightarrow{r_1}, \overrightarrow{r_2}, \cdots, \overrightarrow{r_N})$, significantly simplifying the computational problem [71]

3.1.1 The Hohenberg-Kohn Theorems

The theoretical foundation of DFT lies in two theorems formulated by Pierre Hohenberg and Walter Kohn in 1964. These theorems provided a transformative approach to quantum mechanics by focusing on the electron density as the central quantity [72]. The first Hohenberg-Kohn theorem asserts that the ground-state energy of a many-electron system is a unique functional of the electron density $\rho(\vec{r})$:

$$E[\rho(\vec{r})] = F[\rho(\vec{r})] + \int V_{ext}(\vec{r})\rho(r)d\vec{r}$$

Here, $F[\rho(\vec{r})]$ is a universal functional that includes the kinetic energy of a non-interacting electron system and the electron-electron interaction energy. The term $\int V_{ext}(\vec{r})\rho(r)d\vec{r}$ represents the external potential energy, typically from the nuclei in the system [72]. This theorem implies that the electron density $\rho(\vec{r})$ completely determines the ground-state energy and all other properties of the system.

The second Hohenberg-Kohn theorem establishes that the correct ground-state density minimizes the energy functional:

$$\frac{\delta E[\rho(\vec{r})]}{\delta \rho(\vec{r})} = 0$$

This variational principle states that the ground-state electron density $\rho_0(\vec{r})$ minimizes the energy functional $E[\rho(\vec{r})]$, leading to the ground-state energy E_0 [72].

3.1.2 The Kohn-Sham Formalism

Although the Hohenberg-Kohn theorems provided the theoretical basis for DFT, they did not specify how to construct the functional, $F[\rho(\vec{r})]$. This issue was addressed by Walter Kohn and Lu Jeu Sham in 1965, who introduced the Kohn-Sham formalism, making DFT practical for real systems [73]. The Kohn-Sham formalism involves replacing the complex many-body problem with a system of non-interacting electrons that produces the same ground-state density as the real system. The Kohn-Sham equations are given by:

$$\left(-\frac{\hbar^2}{2m}\nabla^2 + V_{eff}(\vec{r})\right)\psi_i(\vec{r}) = \epsilon_i \psi_i(\vec{r})$$

In these equations, $\psi_i(\vec{r})$ are the Kohn-Sham orbitals, and ϵ_i are the corresponding orbital energies. The effective potential $V_{eff}(\vec{r})$ is defined as:

$$V_{eff}(\vec{r}) = V_{ext}(\vec{r}) + \int \frac{\rho(\vec{r}')}{|\vec{r} - \vec{r}'|} d\vec{r}' + V_{xc}[\rho(\vec{r})]$$

The effective potential consists of three components: $V_{ext}(\vec{r})$ is the external potential due to the nuclei; $V_{xc}[\rho(\vec{r})]$ is the exchange-correlation potential, which accounts for quantum mechanical effects of exchange and correlation between electrons; and $\int(\rho(\vec{r}')/|\vec{r} - \vec{r}'|)d\vec{r}'$ is the Hartree potential, the classical electrostatic interaction between electrons. The Kohn-Sham equations are solved self-consistently, meaning the electron density $\rho(\vec{r})$ is iteratively updated until it converges to a consistent solution.

3.1.3 The Exchange-Correlation Functional

The exchange-correlation functional $V_{xc}[\rho(\vec{r})]$ represents the most challenging part of DFT, as it contains the complex many-body effects of electron-electron interactions. Since the exact form of $V_{xc}[\rho(\vec{r})]$ is unknown, various approximations are used.

The Local Density Approximation (LDA) assumes that the exchange-correlation energy at a point $\vec{r}$ depends only on the electron density $\rho(\vec{r})$ at that point:

$$E_{xc}^{LDA}[\rho(\vec{r})] = \int \epsilon_{xc}\big(\rho(\vec{r}')\big)\rho(\vec{r}')\, d\vec{r}'$$

Here, $\epsilon_{xc}\big(\rho(\vec{r})\big)$ is the exchange-correlation energy per electron in a uniform electron gas of density $\rho(\vec{r})$ [73].

The Generalized Gradient Approximation (GGA) improves upon LDA by considering not only the electron density but also its gradient $\vec{\nabla}\rho(\vec{r})$:

$$E_{xc}^{GGA}[\rho(\vec{r})] = \int f(\rho(\vec{r}'), \vec{\nabla}\rho(\vec{r}'))\, d\vec{r}'$$

GGA captures more of the non-local effects of electron interactions, often providing more accurate results for systems where the electron density varies significantly, such as in molecules and surfaces [74]. The difference between these approximations arises from the choice of the functional f. The most commonly used functionals within this approximation are the one proposed by Perdew, Burke, and Ernzerhof, known as PBE, and the combination of Becke's exchange functional with the correlation functional of Lee, Yang, and Parr, known as BLYP [75].

Over the past four decades, hundreds of density functionals, varying in complexity and application, have been developed by research groups worldwide, reflecting a clear trend of increasing sophistication over time [76]. In this work, we have used the hybrid meta-GGA M06-2X functional, developed by Truhlar and co-workers at the University of Minnesota [77]. It belongs to the broader family of M06 functionals, which were designed to balance accuracy in predicting thermochemistry, non-covalent interactions, and reaction barriers, making them particularly useful for a wide range of chemical applications. M06-2X is composed of 54% Hartree-Fock (HF) exchange, which contributes to its robustness in handling non-covalent interactions such as hydrogen bonding and dispersion forces. The functional is considered to be highly effective for organic chemistry, including atmospheric chemistry, where it has been employed in studies involving complex hydrogen-bonded systems and reactions that involve both main-group elements and transition metals.

3.2 Basis Function Set

In quantum chemical calculations, the basis set plays a fundamental role in the accurate and efficient calculation of the electronic structure of a system. The basis set provides the mathematical framework for representing the wavefunctions, or orbitals, of the electrons within the system. The choice of basis set significantly influences the accuracy, efficiency, and feasibility of DFT calculations.

In quantum mechanics, the state of an electron in an atom or molecule is described by a wavefunction $\psi(\vec{r})$, which depends on the spatial coordinates $\vec{r}$ of the electron [78]. However, the exact wavefunction for a many-electron system is complex and computationally challenging to determine directly. In DFT, we work with Kohn-Sham orbitals, which are single-particle wavefunctions representing an effective non-interacting system [73].

A basis set is a collection of mathematical functions used to approximate these wavefunctions. Each orbital $\psi_i(\vec{r})$ is expressed as a linear combination of basis functions $\phi_i(\vec{r})$, typically represented as:

$$\psi_i(\vec{r}) = \sum_j c_{ij}\phi_j(\vec{r})$$

where $\phi_j(\vec{r})$ are the basis functions, and c_{ij} are the coefficients that are determined during the DFT calculation.

In the Kohn-Sham formalism, the electron density $\rho(\vec{r})$ is expressed as a sum of the squares of the Kohn-Sham orbitals:

$$\rho(\vec{r}) = \sum_i |\psi_i(\vec{r})|^2$$

The accuracy of $\rho(\vec{r})$ depends on how well the Kohn-Sham orbitals $\psi_i(\vec{r})$ are represented by the chosen basis set $\phi_j(\vec{r})$ [73]. The electron density determines all properties of the system in DFT. A well-chosen basis set allows for an accurate approximation of the electron density, leading to precise predictions of physical and chemical properties [71]. The completeness of the basis set is key to achieving convergence. A complete basis set would perfectly describe the orbitals, but in practice, a finite basis set is used, balancing accuracy and computational cost. A larger basis set can describe more subtle features of the electron density but at a higher computational expense [79].

The basis set most commonly used in quantum chemistry are usually composed of Gaussian-Type Orbitals (GTOs) which have the following form:

$$\phi(\vec{r}) = e^{-\alpha r^2}$$

where α is a parameter that controls the width of the Gaussian. GTOs are computationally efficient because the integrals involving these functions can be computed analytically [80].

Plane waves are frequently employed in solid-state physics for periodic systems like crystals. Plane waves are functions of the form:

$$\phi(\vec{r}) = e^{i\vec{k}\cdot\vec{r}}$$

where $\vec{k}$ is the wave vector. Plane waves naturally satisfy periodic boundary conditions, making them ideal for representing electronic states in crystals [81].

Slater-Type Orbitals (STOs) are functions of the form:

$$\phi(r) = e^{-\zeta r}$$

where ζ is a parameter. STOs more closely resemble the actual shape of atomic orbitals but are computationally more challenging to use due to the difficulty in evaluating integrals [82].

Basis sets serve as the foundation for representing the wavefunctions of electrons in atoms and molecules, and different types of basis sets offer varying levels of precision and computational cost. Minimal basis sets are composed of the smallest number of functions necessary to describe the electron distribution within an atom. For example, a minimal basis set for a hydrogen atom includes only one function representing the 1s orbital, while for heavier elements, it includes one function for each occupied atomic orbital, such as 1s, 2s, and 2p for carbon [80]. The primary advantage of minimal basis sets is their computational efficiency, as they use the fewest functions possible, making them particularly suitable for quick calculations on large systems or when high precision is not essential [78]. However, minimal basis sets have significant limitations, particularly in their ability to capture subtle electronic effects such as polarization. Polarization refers to the distortion of an electron cloud in response to external fields or nearby charges, and because minimal basis sets lack the necessary functions to describe such distortions, they often fail to accurately model systems where electron distribution is non-spherical [80].

Double-zeta (DZ) and triple-zeta (TZ) basis sets provide a more sophisticated approach by extending the minimal basis sets through the inclusion of additional functions for each orbital.

In a DZ basis set, each orbital is represented by two functions, while in a TZ basis set, each orbital is represented by three functions [83]. This added flexibility allows the wavefunctions to adapt more precisely to the chemical environment. For instance, in a DZ basis set, the two functions for a 1s orbital might consist of one function that is tightly bound and another that is more diffuse, thereby providing a better description of electron density changes during bonding or in the presence of external fields [79]. While DZ and TZ basis sets offer improved accuracy in describing electron correlation and polarization effects compared to minimal basis sets, this increased precision comes at the cost of higher computational demands. Triple-zeta basis sets, in particular, are more computationally intensive but are essential for systems where electron correlation plays a significant role [83].

Augmented basis sets, on the other hand, are designed to include additional diffuse functions that extend farther from the nucleus, allowing for a more accurate description of electrons in regions of low electron density [84]. These basis sets are particularly important for systems where electron density is spread over a large volume, such as in anions or systems with significant van der Waals interactions. They are also essential for accurately modeling excited states and long-range charge transfer processes [79]. The diffuse functions in augmented basis sets have small exponents, meaning they represent orbitals with low electron density near the nucleus. This is critical for capturing long-range interactions and subtle effects that would be missed by more compact basis sets [83]. Although augmented basis sets significantly improve the accuracy of calculations involving weak interactions or highly polarizable systems, they also increase computational cost. As a result, they are often used selectively, in combination with DZ or TZ sets, to target specific effects without excessively raising computational demands [79].

In summary, the choice between minimal, double-zeta, triple-zeta, and augmented basis sets involves balancing the need for accuracy with the available computational resources. Minimal basis sets are valuable for quick, approximate calculations but may overlook important physical effects. Double-zeta and triple-zeta sets offer enhanced accuracy, particularly in systems with significant electron correlation and polarization. Augmented basis sets are indispensable for capturing diffuse electron distributions and weak interactions, making them crucial for certain chemical and physical systems. A thorough understanding of the strengths and limitations of each type of basis set enables researchers to select the most appropriate one for their specific study.

3.3 Applications and Limitations of DFT

DFT is a widely utilized computational method in materials science, chemistry, and condensed matter physics for calculating properties such as total energies, equilibrium geometries, electronic structures, and vibrational frequencies. By focusing on the electron density rather than the full wavefunction, DFT simplifies quantum mechanical calculations, particularly through the Kohn-Sham formalism, which models non-interacting electrons to match the real system's density. The accuracy of DFT is closely tied to the exchange-correlation functional used, a key area of ongoing research. Proper selection of a basis set is essential for balancing accuracy and computational efficiency, with the choice depending on the system's complexity and the properties of interest.

3.4 Computational Methods

The molecular geometries of the isolated OA, SA and AM molecules and those of the hydrogen-bonded binary and ternary clusters formed with these molecules were fully optimized without any constraint, in gas phase, using the M06-2X functional with Pople’s split-valence triple zeta 6-311++G(3df,3pd) basis set. This M06-2X/6-311++G(3df,3pd) model is well recommended in the literature for quantum-chemical analysis of hydrogen bonding interactions among atmospheric molecules [13, 85-88].

Five structurally different conformers of OA monomer have been considered whose initial geometries were prepared based on previous works [89-99]. The initial structures clusters were then prepared following a multi-step approach, considering the fact that all the monomers (OA, SA and AM) can simultaneously act as proton-acceptor and proton-donor, facilitating the formation of multiple HBs. Moreover, depending on the relative position of COOH groups on either side of the central C–C bond, different forms of intermolecular arrangement for hydrogen bonding are possible. As the main objective of this work is to observe how different conformations of OA influence its hydrogen bonding characteristics, we searched for different possible HB patterns for each OA conformation.

Initially, several binary or ternary clusters were prepared by strategically placing SA and/or AM around the hydrogen bonding sites of OA using the Gaussview molecular visualization program [100], and all of them were optimized using the M06-2X/6-31++G(d,p) model. Some of these optimized structures were then selected based on energy and structural distinctness, and further optimized by the larger M06-2X/6-311++G(3df,3pd) basis set. Finally, a few of the lower energy cluster geometries for each OA monomer were chosen for final analysis. After each geometry optimization, the vibrational frequencies were obtained at the same level of calculation to ensure that all frequencies are positive and the optimized geometry is a local minimum on the potential energy hypersurface.

Thus, in this work, we consider each of the five OA conformers individually interacting with AM and SA to form the (OA)(AM) and (OA)(SA) dimers, as well as the $(OA)(AM)_2$, $(OA)(SA)_2$ trimers. This results in a total of 10 different dimer compositions and 10 trimer compositions. Each cluster composition, on the other hand, contains multiple structural conformations with varying electronic energies in most cases, as we will discuss in the next section.

All calculations were performed using Gaussian 16 [101] computational chemistry software package. Preparation of the initial molecular structures and partial analysis of the calculated results were done by Gaussview interface [100].

3.4.1 Energetics and Thermochemistry

The binding electronic energy (ΔE) and the binding Gibbs free energy of formation (ΔG) were calculated for each cluster considering the usual super-molecular approach:

$$\Delta X = X_{\mathrm{cluster}} - \sum X_{\mathrm{monomer}} \tag{1}$$

where $X = E$ (electronic energy of the system) or G (electronic energy with thermal free energy correction). Both E and G are corrected for zero-point energy (ZPE). As each cluster composition may possess several energetically stable conformers, the effect of multiple conformers on the cluster binding free energy is calculated as [21, 102, 103].

$$\Delta G_{MC} = RT\ln\left[\sum_{k=1}^{n} \exp\left(\frac{-\Delta G_k}{RT}\right)\right] \tag{2}$$

where $R = 8.314\ \mathrm{J/(mol \cdot K)}$ is the universal gas constant and T is the ambient temperature.

When molecules come together to form a cluster or complex, they may undergo changes in their geometries to adapt to the new environment or interactions. The energy required for these structural adjustments is commonly referred to as distortion energy or relaxation energy. In mathematical terms, the distortion energy of a molecule engaged in clustering is determined by subtracting the electronic energy of that molecule (monomer) in its isolated form (E_i) from the energy of the same monomer with its geometry altered and fixed within the cluster (E_i^N). The total distortion energy of the cluster containing N monomers, $\Delta E_D(T)$, is the sum of the individual distortion energies of all monomers within the cluster. Thus,

$$\Delta E_D(T) = \sum_{i=1}^{N} [E_i^N - E_i] \tag{3}$$

In physical terms, ΔE_D, a positive quantity, is a measure of the strain or perturbation introduced into the system due to the molecular clustering process.

Since the probability of a given set of molecules arranging themselves in a particular configuration k with Gibbs free energy change of ΔG_k is proportional to the Boltzmann factor of the cluster formation, $\exp(-\Delta G_k/RT)$, the population fraction, $PF(k)$ of different conformations in a particular cluster composition were calculated by using the following relation:

$$PF(k) = \frac{\exp\left(-\frac{\Delta G_k}{RT}\right)}{\sum_i \exp\left(-\frac{\Delta G_i}{RT}\right)} \times 100\%. \tag{4}$$

3.4.2 Electric and Optical Parameters

The molecules present in the atmosphere do interact with solar radiation. In fact, the elastic and inelastic scattering of solar radiation by atmospheric particles plays a significant role in understanding various phenomena related to visibility and radiative forcing in the atmosphere. Elastic scattering of light, also known as Rayleigh scattering, stands out as the predominant optical phenomenon for small atmospheric molecular clusters, playing a vital role in various atmospheric processes. The intensity of Rayleigh scattering, often referred to as Rayleigh activity, depends on the dipole polarizability of the molecular system and its anisotropy.

Polarizability (α) is a measure of how easily the electron cloud of a molecule can be distorted by an external electric field, that results in the creation of an induced dipole moment in the molecule. Anisotropy of the polarizability refers to the directional dependence of the polarizability. Together, these characteristics govern the extent of interaction between incident radiation and the molecules, thereby influencing the resultant scattering intensity. This fundamental interplay sheds light on the intricate dynamics of light-matter interactions within the atmosphere, providing insights into its complex behavior and processes.

The optical properties, such as the Rayleigh scattering intensities and depolarization ratios for natural light, of the monomers and OA-mediated clusters were obtained, at the same M06-2X/6-311++G(3df,3pd) level, using the following definitions [104-107].

$$\Re_n = 45(\bar{\alpha})^2 + 13\,(\Delta\alpha)^2, \quad \sigma_n = \frac{6\,(\Delta\alpha)^2}{45(\bar{\alpha})^2 + 7\,(\Delta\alpha)^2}, \tag{5}$$

where, $\bar{\alpha}$ and $\Delta\alpha$ are the mean isotropic polarizability and the anisotropy of polarizability of the molecular system,

$$\bar{\alpha} = \frac{1}{3}\left(\alpha_{xx} + \alpha_{yy} + \alpha_{zz}\right)$$

$$(\Delta\alpha)^2 = \tfrac{1}{2}\left[\left(\alpha_{xx} - \alpha_{yy}\right)^2 + \left(\alpha_{yy} - \alpha_{zz}\right)^2 + (\alpha_{zz} - \alpha_{xx})^2\right] + 3\left(\alpha_{xy}^2 + \alpha_{xz}^2 + \alpha_{yz}^2\right) \tag{6}$$

4 RESULTS AND DISCUSSION

4.1 Isolated Molecule of Oxalic Acid ($C_2H_2O_4$)

Oxalic Acid (OA) is a molecule of significant atmospheric importance [89, 108-131]. It is the simplest naturally occurring water-soluble dicarboxylic acid (DCA) found in various environmental sources, such as plants, fungi, and some marine organisms [108, 127, 131-133]. In human body, OA is produced through the metabolism of certain plant-based foods like leafy greens (such as spinach, rhubarb, amaranth), nuts, seeds, tea, sweet potatoes, okra etc. [134-137]. In the atmosphere, OA may be formed via oxidation of larger compounds such as isoprene and monoterpenes, volatile organic compounds emitted by transpiration from plant leaves [118,138. 139]. DCAs, in general, are common organics identified both in the urban and rural areas mainly due to the intense agricultural and industrial activities and are an important constituent of the nucleation process due to their low vapor-pressure [89, 128, 129, 140-143]. Moreover, being water-soluble, DCAs may serve as cloud condensation nuclei becoming relevant in the global climate system.

OA is reported to be the most abundant atmospheric DCA detected in the air as a major constituent of ultrafine and fine aerosol particles [115, 89, 128, 129, 143-146]. Notably, the gas phase concentration of OA is reported to be in the range of 9.3×10^{10} to 5.4×10^{12} molecules/cm^3 [129,130,146] which is much higher than that of ammonia (AM) and sulfuric acid (SA), as the typical concentrations of SA and AM are in the range of 10^4–10^8 molecules/cm^3 and 10^7–10^{11} molecules/cm^3, respectively [67, 62, 129, 130, 147, 148]. OA and SA are two crucial precursor molecules in atmospheric nucleation, contributing significantly to the formation of secondary aerosols [13, 26, 31, 148-152].

The molecular configuration of OA, with two carboxylic (COOH) groups on either side of a C–C bond, imparts substantial rotational flexibility, leading to the possible existence of several conformers, each with distinct structural arrangements. Over the past few decades, several experimental [90, 91, 153-156] and theoretical [89-99] investigations explored the intricate conformational landscape of OA. Theoretical predictions suggest that in gas phase, OA should have at least five different structural conformations. The three lowest energy conformations predicted by theory have been observed experimentally [90, 91, 156]. On the other hand, the presence of two COOH groups enables OA to engage in a greater number of hydrogen bonding interactions, compared to monocarboxylic acids, with two carbonyl (C=O) groups acting as proton acceptors, and the OH groups acting as proton donors.

Recent theoretical investigations on atmospheric nucleation and new particle formation in the context of SOA reveal that OA can generate thermodynamically stable hydrogen-bonded clusters with atmospherically relevant molecules such as SA, water, AM, amines and Methanesulfonic Acid [89, 110-115, 119-126, 130, 157]. While the contribution of hydrogen-bonded interactions of oxalic acid, particularly considering its lowest energy conformations or a few others, in atmospheric aerosol formation is widely studied, the hydrogen bonding characteristics of individual oxalic acid conformers have not yet been fully explored. Quantum chemical calculations on the binary and ternary clusters OA with AM and H_2O [113, 114], hydration of OA dimer [122], OA-catalyzed hydration reaction of SO_3 [89] and dissociation of oxalic acid in water clusters [97] are the few ones that considered all the five OA conformers.

The equilibrium geometries of the five conformers of the isolated molecule of Oxalic Acid (OA), optimized by M06-2X/6-111++G(3df,3pd) model, are illustrated in **Figure 3**, organized in the order of the relative electronic energy, ΔE_R. The conformers are named hereafter as cTc, cTt, tTt, tCt and cCt following earlier works on OA [67, 89, 90, 156, 96, 97].

The nomenclature considers the basis torsional degrees of freedom of the OA structures. The upper-case letters C and T represent the cis and trans configurations, respectively, of the $\mathrm{O} = \mathrm{C} - \mathrm{C} = \mathrm{O}$ dihedral angle corresponding to the internal rotation of the carboxyl COOH groups around the $\mathrm{C} - \mathrm{C}$ bond. The lower-case letters c and t, on the other hand, signify the cis and trans configurations of the two $\mathrm{C} - \mathrm{C} - \mathrm{O} - \mathrm{H}$ dihedral angles, representing the rotation of the OH group about the $\mathrm{C} - \mathrm{O}$ bond in each COOH group.

In the lowest energy conformation of OA (cTc), two carboxyl groups are trans to each other, i.e., $\varphi(\mathrm{O} = \mathrm{C}\text{–}\mathrm{C} = \mathrm{O}) = 180°$ and both OH groups are cis with respect to the $\mathrm{C} - \mathrm{C}$ bond. As a result, cTc is stabilized by the formation of two intramolecular $\mathrm{O} - \mathrm{H} \cdots \mathrm{O}$ HBs of equal bond length (2.12 Å) and bond angle (115.5°). The second most stable conformation (cTt) differs from cTc by the internal rotation of one of the two OH groups about the $\mathrm{C} - \mathrm{O}$ bond, making it trans with respect to the $\mathrm{C} - \mathrm{C}$ bond. As a result, cTt possesses only one intra-molecular HB which has a bond length of $2.09\,\text{Å}$. The energy difference between cTc and cTt is $2.68\,\mathrm{kcal/mol}$. The electronic energy differences between the conformers obtained by M06-2X/6-311++G(3df,3pd) match closely with those obtained by higher level energy calculations with MP2/aug-cc-pVDZ and CCSD(T)/aug-cc-pVTZ//B3LYP/6- 311++G(d,p) models [34]. The cTc, cTt and tTt are the only conformers that have been detected by experiments [78-80].

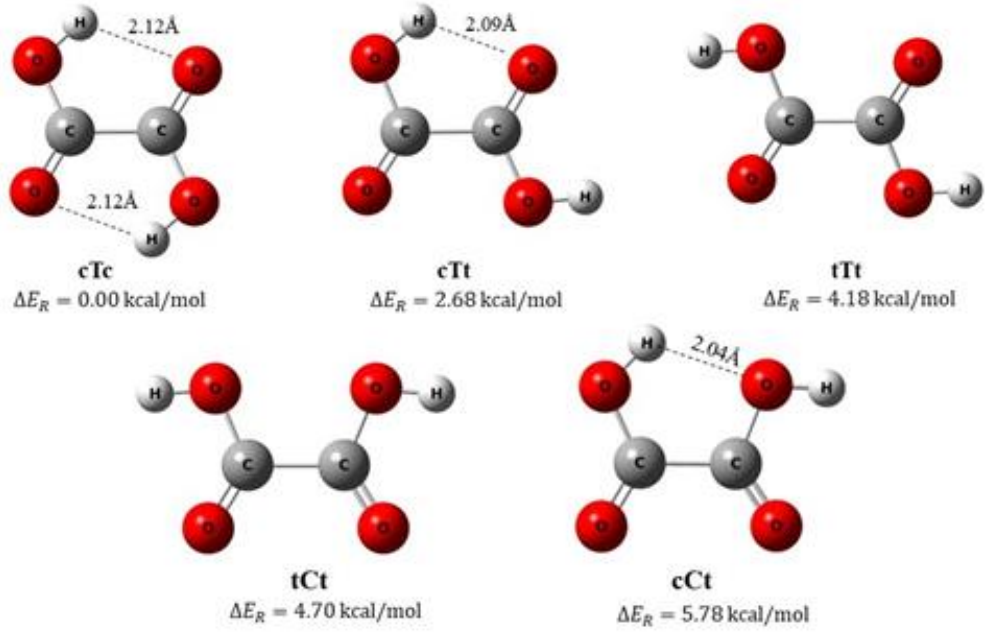

cTc $\Delta E_R = 0.00$ kcal/mol

cTt $\Delta E_R = 2.68$ kcal/mol

tTt $\Delta E_R = 4.18$ kcal/mol

tCt $\Delta E_R = 4.70$ kcal/mol

cCt $\Delta E_R = 5.78$ kcal/mol

Figure 3: Structures of five stable oxalic acid (OA) conformers, optimized at the M06-2X/6-311++G(3df,3pd) level, with intramolecular hydrogen bonds (dotted line) and relative electronic energy, with zero-point energy corrections, (ΔE_R) with respect to the lowest energy conformer, cTc.

The calculated bond lengths and bond angles of the OA conformers agree well with experiments and previous calculations [92, 96]. Detailed discussions on these structures are available in several previous works on OA [92-96]. We provide the structural parameters obtained by our M06-2X/6-311++G(3df,3pd) along with others from the literature in **Table 2.**

Table 2: Optimized bond lengths, r (in Å) and bond angles, δ (in degrees) of different Oxalic Acid conformers, calculated by theoretical models - M1: M06-2X6-311++G(3df,3pd) – present work; M2: B3LYP/6-311++G(d,p) – Ref [92]; M3: MP2/6-311++G(d,p) – Ref [96].

		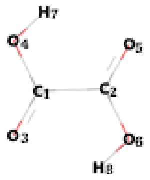 **cTc**			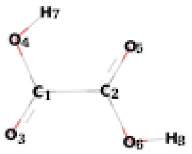 **cTt**			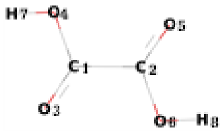 **tTt**	
	M1	M2	M3	M1	M2	M3	M1	M2	M3
$C_1 - C_2$	1.542	1.549	1.543	1.544	1.549	1.543	1.540	1.544	1.537
$C_1 - O_3$	1.194	1.203	1.210	1.186	1.193	1.215	1.190	1.199	1.207
$C_1 - O_4$	1.316	1.325	1.327	1.326	1.338	1.329	1.328	1.339	1.342
$C_2 - O_5$	1.194	1.203	1.210	1.199	1.208	1.201	1.190	1.199	1.207
$C_2 - O_6$	1.316	1.325	1.327	1.317	1.326	1.340	1.328	1.339	1.342
$O_4 - H_7\ (O_6 - H_8)$	0.971	0.975	0.973	0.969	0.973	0.971	0.966	0.970	0.969
$O_3 - C_1 - O_4$	125.5	125.3	125.3	124.9	124.5	124.6	125.7	125.4	125.7
$C_1 - O_4 - H_7$	108.0	107.8	-	108.7	108.3	-	107.6	107.5	-
$C_2 - C_1 - O_4$	113.5	113.5	113.5	111.5	111.3	111.4	110.5	110.2	109.9
$C_2 - O_6 - H_8$	108.0	107.8	-	108.4	108.3	-	107.6	107.5	-

	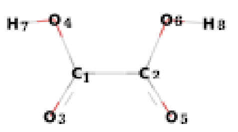 tCt			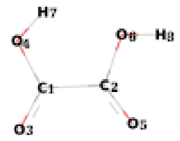 cCt		
	M1	M2	M1	M2	M1	M2
C_1-C_2	1.542	1.545	1.538	1.549	1.554	1.547
C_1-O_3	1.188	1.197	1.205	1.183	1.191	1.200
C_1-O_4	1.332	1.342	1.344	1.333	1.343	1.345
C_2-O_5	1.188	1.197	1.205	1.184	1.191	1.200
C_2-O_6	1.332	1.342	1.344	1.347	1.360	1.361
$O_4-H_7\ (O_6-H_8)$	0.967	0.970	0.969	0.965	0.969	0.969
$O_3-C_1-O_4$	125.5	125.3	125.6	123.8	123.5	123.5
$C_1-O_4-H_7$	107.5	107.5	-	110.7	110.2	-
$C_2-C_1-O_4$	112.6	112.7	112.5	115.3	115.3	115.5
$C_2-O_6-H_8$	107.5	107.5	-	108.5	108.9	-

Now, we discuss briefly some of the electric and spectroscopic parameters, which are also important for characterization of the conformers. As can be seen from **Table 3**, cTc and tTt are the only OA conformers among the five, that have zero dipole moment, as a consequence of their structural feature. Both possess C_{2h} symmetry, with the two COOH groups having trans configuration with respect to each other. So, the dipole moment vectors corresponding to each group acts in opposite direction nullifying the total dipole of the system. The dipole moment of 3.15 D for cTt, calculated by the present M06-2X/6-311++G(3df, 3pd), agrees well with the experimentally measured value of $3.073(6)$ D [91] and B3LYP/aug-cc-pVDZ calculated value of 3.14 D [67].

Table 3: Calculated values of dipole moment (μ), mean dipole polarizabilty ($\bar{\alpha}$), polarizability anisotropy ($\Delta\alpha$), rotational constants (A, B and C)[#], degree of depolarization (σ_n) and Rayleigh activity for natural light ($\Re_n$) of the five OA conformers as obtained by M06-2X/6-311++G(3df, 3pd) model.

	cTc	cTt	tTt	tCt	cCt
μ (D)	0.00	3.15	0.00	2.98	4.89
α (a.u.)	37.36	37.84	38.13	38.16	37.99
$\Delta\alpha$ (a.u.)	20.37	19.72	19.53	19.60	19.72
A (GHz)	5.878	6.027	6.149	6.120	6.000
B (GHz)	3.855	3.708	3.611	3.619	3.672
C (GHz)	2.328	2.296	2.275	2.274	2.278
σ_n (a.u.)	0.044	0.041	0.039	0.039	0.040
$\Re_n$ (a.u.)	68188.7	67140.3	68103.4	68198.4	69983.7

[#] Experimental values of the rotational constants (GHz): $A = 5.951$, $B = 3.684$, $C = 2.276$ [80].

Apart from cTc and cTt, the highest energy conformer cCt also has one intramolecular HB. Curiously, it has the shortest HB length (2.12 Å) and highest dipole moment (4.89 D) among all the clusters. The same observation was also found in B3LYP/6-311++G(d,p) calculation [67].

Since both the OH groups in the lowest energy cTc conformer are oriented inwardly, it has the lowest molecular volume with an electronic spatial extent (ESE) of $479\ \mathrm{a.u.}$ On the other hand, both the tTt and tCt conformers with their OH groups looking outward in opposite directions, have the highest volume with $\mathrm{ESE} \approx 491\ \mathrm{a.u.}$. ESE is a measure of the average size of the electron distribution in a molecule. Molecules with larger ESE have more diffuse electron clouds, which generally leads to greater polarizability, as the extended electron cloud can be more easily distorted by an external field. As a result, tTt and tCt have the highest mean dipole polarizabilities with α=38.13 a.u. and 38.16 a.u., respectively, while cTc has the lowest polarizability (α=37.36 a.u.). However, in general, the difference of polarizability between the conformers is minimum.

In case, of degree of depolarization (σ_n) all the conformers have the same and a very small value with $\sigma_n \approx 0.04\ \mathrm{a.u.}$ which signifies that the polarization state of the incident light will remain almost unaltered during the scattering process with OA conformers. As far as the elastic light scattering (Rayleigh scattering) is concerned, the scattering intensities also do not vary appreciably from one conformer to another, but the highest energy cCt shows the highest Rayleigh activity suggesting most effective scattering of incident radiation by this conformer.

A sequential interconversion among the conformations either in decreasing or increasing order of electronic energy (cCt ⇄ tCt ⇄ tTt ⇄ cTt ⇄ cTc) is possible just by rotation of a single dihedral angle in each confirmation. Figure 4 illustrates a schematic representation of the rotational energy barriers for these interconversions, obtained through the constrained optimizations (energy scan) of the molecule, rotating a selected dihedral angle in small increments of 3° and optimizing the molecular geometry while keeping the dihedral angle fixed at the incremented value. For instance, rotating a COOH group about the central $\mathrm{C-C}$ bond or the $\mathrm{C-C-O-H}$ dihedral allows the transition from the tCt to the tTt conformer. The rotational energy barrier in this case is remarkably low, measuring just $0.86\ \mathrm{kcal/mol}$ for tCt → tTt and $1.48\ \mathrm{kcal/mol}$ for tTt → tCt, representing the minimum barrier encountered by our calculation at the M06-2X/6-311++G(3df, 3pd) level. The highest energy barriers are observed for the cTc → cTt and cTt → cTc interconversions, with values of $13.98\ \mathrm{kcal/mol}$ and $11.07\ \mathrm{kcal/mol}$, respectively. These transitions involve the rotation of a specific $\mathrm{O=C-O-H}$ dihedral, transitioning from a trans to cis configuration. The calculated barriers agree well with previous predictions with different models [97, 98]. As can be observed in the figure, with the exception of tCt ⇄ tTt , the rotational barriers are significantly high, suggesting that cCt, cTt, and cTc conformers possess considerable stability under normal conditions.

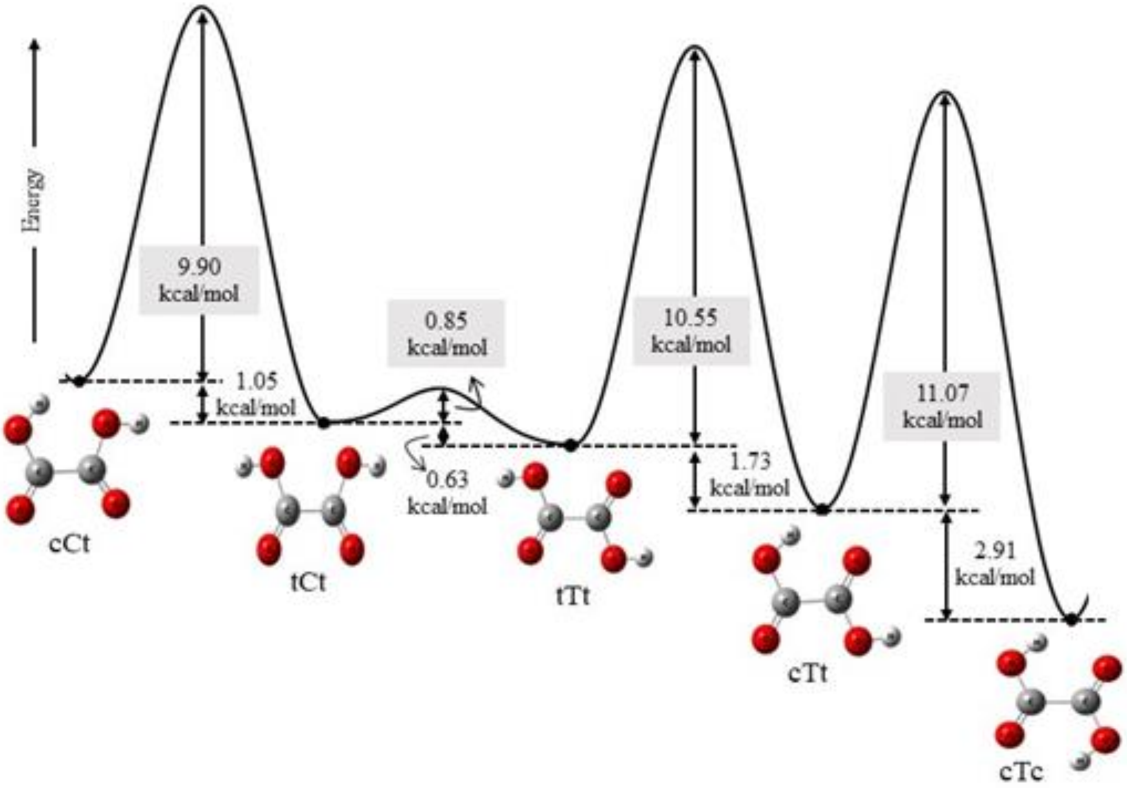

Figure 4: Schematic diagram of the rotational barriers for the possible interconversions among the OA conformers as obtained by M06-2X/6-311++G(3df, 3pd) level.

Among the five OA conformers, cTc, tTt and tCt contain degenerate vibrational stretching modes for the OH group as a consequence of the symmetry of the molecule. In the cTc conformer, the two equivalents OH groups asymmetrically stretch at $3727\,\mathrm{cm}^{-1}$ with an intensity of $306.6\,\mathrm{km/mole}$, while they symmetrically stretch at $3723\,\mathrm{cm}^{-1}$ with an almost negligible intensity of $0.012\,\mathrm{km/mole}$. For both tTt and tCt conformers, the vibrational frequencies for these coupled symmetric and asymmetric stretching modes are practically the same, measuring $3832\,\mathrm{cm}^{-1}$ for tTt and $3821\,\mathrm{cm}^{-1}$ for tCt. However, the intensity of asymmetric vibration is significantly higher the symmetric vibration in both cases. In contrast, for cTt and cCt conformers, the OH groups exhibit independent stretching modes with similar intensities of vibration. The calculated OH stretching frequencies for the cis-CCOH (trans-CCOH) of cTt and cCt are approximately $3773\,(3819)\,\mathrm{cm}^{-1}$ and $3824\,(3830)\,\mathrm{cm}^{-1}$, respectively. Considering the experimentally observed OH stretching frequencies in the range of $3453-3461\,\mathrm{cm}^{-1}$, we notice that the M062X/6-311++G(3df,3pd) level of calculation overestimates the OH stretching frequencies by 7%.

4.2 Clusters of Oxalic Acid and Ammonia

In this section we analyze the structural and thermochemical properties of the binary and ternary clusters formed by one molecule of the five conformers of OA (cTc, cTt, tTt, tCt, cCt) with AM at ambient condition. **Figure 5** exhibits the optimized geometries of the 7 binary (OA)(AM) clusters, with (cTt)(AM) and (cCt)(AM) compositions having two conformations each, while (cTc)(AM), (tTt)(AM) and (tCt)(AM) having a single conformation because of structural symmetry. **Figure 6** displays the optimized structures of 10 ternary $(OA)(AM)_2$ clusters, consider for the present work, with each of the five cluster compositions having two structural conformations. Although more than two conformations were identified for certain $(OA)(AM)_2$ compositions, we have selected the two lowest energy conformations, with distinct structural features, for each ternary composition. The hydrogen bonded interactions occur via the $-\mathrm{OH}$ and $-\mathrm{CO}$ groups of the OA molecule, where it acts simultaneously as proton-donor and proton-acceptor, respectively.

As can be seen from **Figures 5 and 6**, the HB distances of the possible $(\mathrm{N})\mathrm{H}\cdots\mathrm{O}$ type interactions between OA and AM, with the former being the proton acceptor, are in general much larger than the $(\mathrm{O})\mathrm{H}\cdots\mathrm{N}$ HB distances when OA acts as proton donor. The HB bond angles are also larger in case of the $(\mathrm{O})\mathrm{H}\cdots\mathrm{N}$ bonds. Thus, we assume that the formation of $(\mathrm{O})\mathrm{H}\cdots\mathrm{N}$ HBs between OA conformers and AM molecules with OA being the proton-donor via its $\mathrm{O}-\mathrm{H}$ moiety and AM being the proton acceptor via the nitrogen atom is responsible for the energetic stability of the (OA)(AM) clusters in ambient condition. Considering its relevance, we report in **Table 4** some structural and spectroscopic parameters required for the characterization of these $(\mathrm{O})\mathrm{H}\cdots\mathrm{N}$ HBs like the distance between the two electronegative heavy atoms (oxygen and nitrogen) participating in the HB formation ($R_{\mathrm{O-N}}$), The HB length ($R_{(\mathrm{O})\mathrm{H}\cdots\mathrm{N}}$), HB angle ($\angle\mathrm{O}-\mathrm{H}\cdots\mathrm{N}$), elongation of the $\mathrm{O}-\mathrm{H}$ bond due to HB formation ($\Delta R_{\mathrm{O-H}}$), $\mathrm{O}-\mathrm{H}$ stretching frequency in the clusters and its red-shift with respect to the isolated OA molecule. As can be seen, all the five conformers of OA form strong $\mathrm{O}-\mathrm{H}\cdots\mathrm{N}$ type HB with an average HB distance (angle) of 1.67 Å ($168.4°$) in case of binary clusters and 1.64 Å ($171.3°$) in ternary clusters. The average red shift of the OA $\mathrm{O}-\mathrm{H}$ stretching frequency is 934 (1088) cm^{-1} in binary (ternary) clusters. Among the two conformations of (cTt)(AM) and also of (cCt)(AM), the Conf. (1) with AM interacting with the single COOH moiety of OA shows stronger hydrogen bonding.

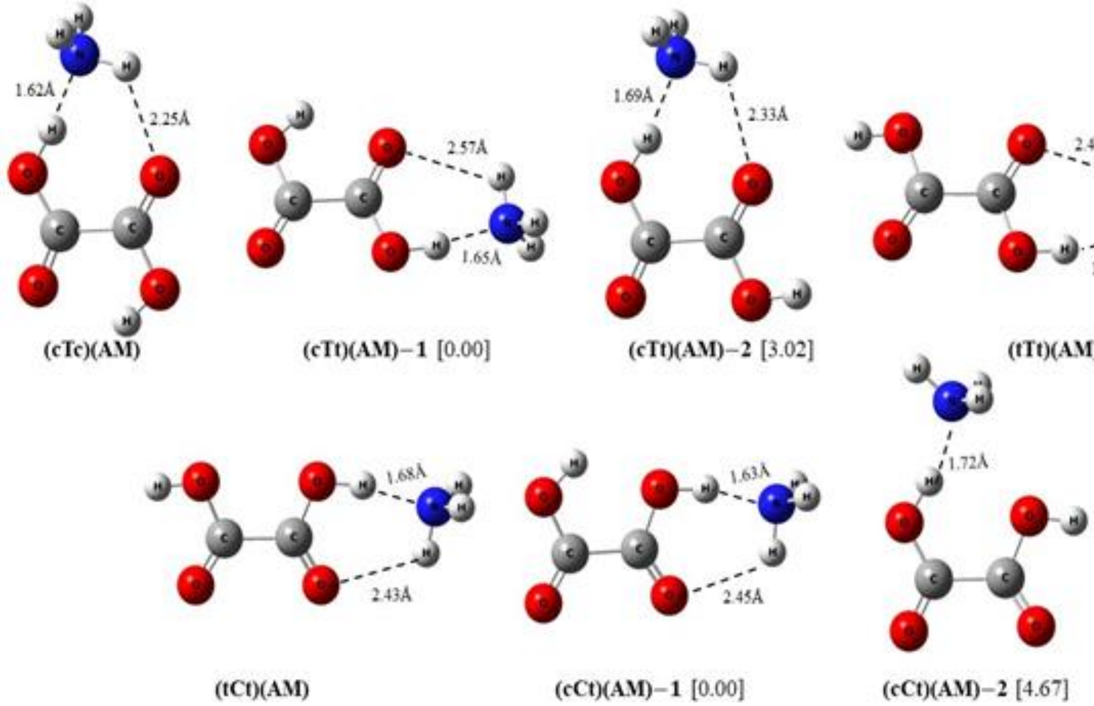

Figure 5: Equilibrium geometries of the stable (OA)(AM) cluster compositions. optimized at the M06-2X/6-311++G(3df,3pd) level. The dashed lines represent the intermolecular hydrogen bonds with respective bond lengths given in angstrom. The numbers in square brackets represent the relative energy differences of the conformations in each cluster composition, in kcal/mol.

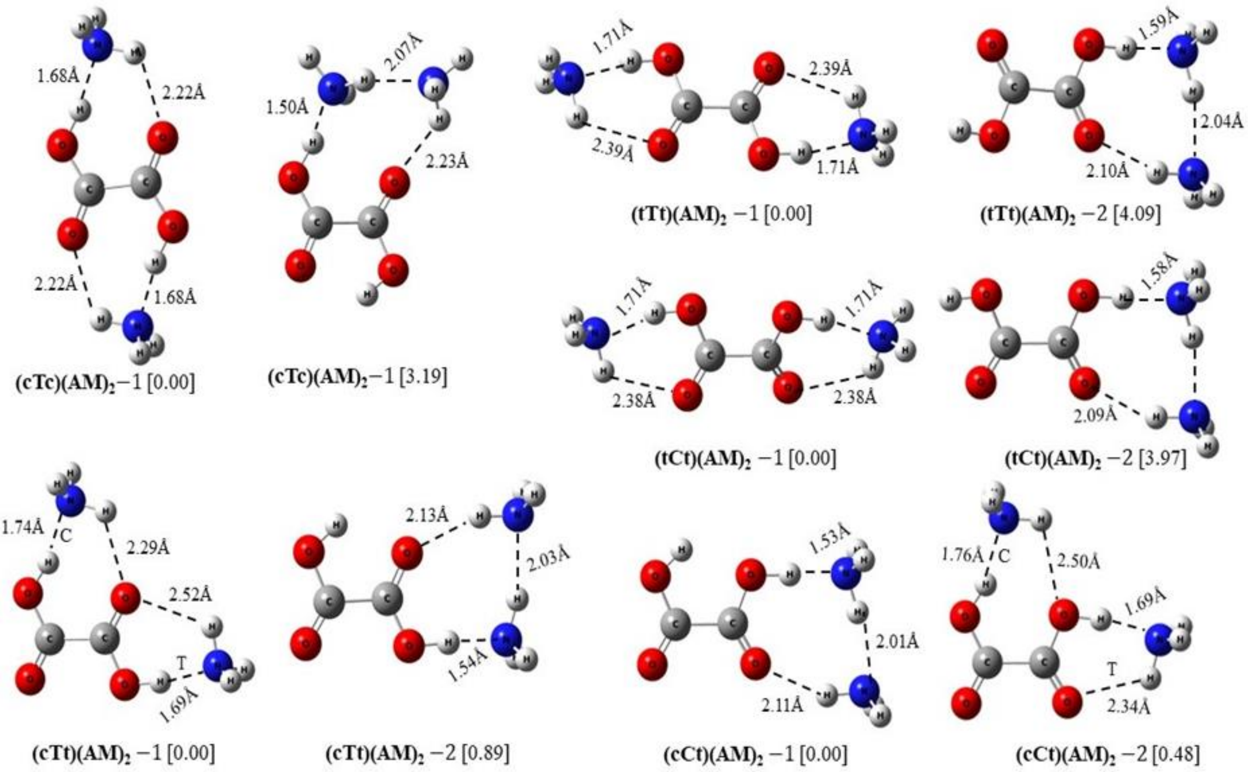

Figure 6: Equilibrium geometries of the stable (OA)(AM)$_2$ cluster compositions. optimized at the M06-2X/6-311++G(3df,3pd) level. The dashed lines represent the intermolecular hydrogen bonds with respective bond lengths given in angstrom. The numbers in square brackets represent the relative energy differences of the conformations in each cluster composition, in kcal/mol.

Table 4: Relevant HB parameters of the binary (OA)(AM) and ternary (OA)(AM)$_2$ clusters including the HB distance, $\mathrm{O-H}$ bond length, variation of the bond length, HB angle, $\mathrm{O-H}$ frequencies and the variation of the $\mathrm{O-H}$ frequencies upon cluster formation. The labels "C" and "T" have been indicated in Figure 6.

		$R_{\mathrm{O-N}}$ (Å)	$R_{\mathrm{(O)H\cdots N}}$ (Å)	$\angle\mathrm{O-H\cdots N}$ (degrees)	$\Delta R_{\mathrm{O-H}}$ (Å)	$\nu_{\mathrm{O-H}}$ ($\mathrm{cm^{-1}}$)	$\Delta\nu_{\mathrm{O-H}}$ ($\mathrm{cm^{-1}}$)
(OA)(AM)							
(cTc)(AM)		2.638	1.619	171.1	0.054	2692	-1035
(cTt)(AM)−1		2.659	1.649	170.7	0.052	2786	-1034
(cTt)(AM)−2		2.685	1.690	167.4	0.040	2974	-799
(tTt)(AM)		2.681	1.682	168.6	0.045	2904	-928
(tCt))(AM)		2.678	1.678	168.2	0.046	2917	-904
(cCt)(AM)−1		2.641	1.632	168.4	0.056	2753	-1071
(cCt)(AM)−2		2.696	1.719	164.1	0.037	3063	-767
(OA)(AM)$_2$							
(cTc)(AM)$_2$ −1		2.678	1.678	168.2	0.042	2894[#1]	-833
(cTc)(AM)$_2$ −2		2.562	1.503	172.1	0.094	2121	-1607
(cTt)(AM)$_2$ −1	C	2.722	1.740	166.4	0.034	3101	-672
	T	2.692	1.693	170.3	0.041	2977	-843
(cTt)(AM)$_2$ −2		2.596	1.545	177.7	0.084	2287	-1532
(tTt)(AM)$_2$ −1		2.704	1.714	167.5	0.039	2997[#2]	-835
(tTt)(AM)$_2$ −2		2.623	1.586	178.2	0.071	2495	-1337
(tCt)(AM)$_2$ −1		2.701	1.710	167.3	0.040	2985[#3]	-836
(tCt)(AM)$_2$ −2		2.622	1.567	178.7	0.072	2478	-1343
(cCt)(AM)$_2$ −1		2.584	1.526	179.8	0.092	2167	-1657
(cCt)(AM)$_2$ −2	C	2.727	1.763	161.8	0.030	3173	-657
	T	2.686	1.690	167.7	0.044	2921	-903

[#1] Asymmetric stretching mode of the two $\mathrm{O-H}$ groups with intensity of $4171\ \mathrm{km/mole}$. The calculated value of the symmetric stretching mode of the same bonds is $2892\ \mathrm{cm^{-1}}$ with an intensity of just $5.2\ \mathrm{km/mole}$.

[#2] Asymmetric stretching mode of the two $\mathrm{O-H}$ groups with intensity of $3785\ \mathrm{km/mole}$. The calculated value of the symmetric stretching mode of the same bonds is $3023\ \mathrm{cm^{-1}}$ with a negligible intensity.

[#3] Asymmetric stretching mode of the two $\mathrm{O-H}$ groups with intensity of $3831\ \mathrm{km/mole}$. The calculated value of the symmetric stretching mode of the same bonds is $3023\ \mathrm{cm^{-1}}$ with an intensity of just $6.6\ \mathrm{km/mole}$.

For ternary clusters involving two AM molecules interacting with OA, we sought configurations that consistently allow interaction with both the OH and CO moieties of OA, originating from either the same or different COOH groups, which yielded two scenarios. The first one involves direct hydrogen bonding between the two AM molecules while both interact with OA. In the second scenario, each AM molecule interacts separately with OA, remaining spatially distant from each other. Clusters formed under the second scenario exhibit higher energy stability for all OA conformers when compared to those formed under the first scenario, as can be verified from the relative electronic energy difference provided in Figure 5. Furthermore, in the second scenario, the vibrational degeneracy of the OH stretching mode persists as the symmetry of the system is maintained. Thus, in the cTc, tTt and tCt conformers, the coupled asymmetric and symmetric stretchings of the two equivalents OH groups continue, both experiencing similar red-shifts. However, in first scenario, where two AM molecules act jointly on one side of OA, the symmetry is altered, and the degeneracy is lifted. In this case, only one of the OH groups directly forms HB by donating proton to nitrogen of AM, resulting a substantial red-sift for that specific OH group.

In **Table 5**, we present the calculated binding electronic energy (ΔE), binding Gibbs free energy (ΔG) at 298.15 K along with the distortion energy (ΔE_D) of the OA monomers and their corresponding binary and ternary clusters with AM. It also reports the population distributions within each cluster compositions, denoted as Relative Population Fraction (RPF), the multiple-conformer cluster binding free energy, ΔG_{MC} in kcal/mol, for each composition and the equilibrium constants (K_{eq}) at 298.15 K for each cluster.

Table 5: Calculated values of binding electronic energies (ΔE), binding free energy ΔG) associated with different (OA)(AM) and (OA)(AM)$_2$ clusters at 298.15 K, in kcal/mol, along with their relative population fraction (RPF), the multi-conformation average binding free energy (ΔG_{MC}) and the equilibrium constants (K_{eq}) of each cluster composition obtained at M06-2X/6-311++G(3df,3pd) level.

	ΔE_B	E_D(OA)	E_D(tot)	ΔG	RPF	ΔG_{MC}	K_{eq}
(OA)(AM)							
(cTc)(AM)	-11.89	4.32	4.39	-3.65	100.00	-3.65	4.8 x 10^2
(cTt)(AM) -1	-12.76	3.16	3.22	-4.51	99.79	-4.51	2.1 x 10^3
(cTt)(AM) -2	-9.73	1.84	1.88	-0.87	0.21		
(tTt)(AM)	-11.72	1.48	1.53	-3.39	100.00	-3.39	3.1 x 10^2
(tCt)(AM)	-11.81	1.50	1.55	-2.71	100.00	-2.71	9.8 x 10^1
(cCt)(AM) -1	-13.57	2.06	2.11	-5.03	99.68	-5.03	4.9 x 10^3
(cCt)(AM) -2	-8.90	2.60	2.63	-1.63	0.32		
(OA)(AM)$_2$							
(cTc)(AM)$_2$ -1	-21.33	5.91	6.05	-5.86	99.92	-5.86	2.0 x 10^4
(cTc)(AM)$_2$ -2	-18.13	8.00	8.18	-1.66	0.08		
(cTt)(AM)$_2$ -1	-20.26	3.53	3.65	-3.68	89.15	-3.75	5.7 x 10^2
(cTt)(AM)$_2$ -2	-19.37	4.65	4.84	-2.43	10.85		
(tTt)(AM)$_2$ -1	-22.42	2.19	2.31	-5.75	99.92	-5.75	1.7 x 10^4
(tTt)(AM)$_2$ -2	-18.33	3.59	3.76	-1.52	0.08		
(tCt)(AM)$_2$ -1	-22.70	2.34	2.46	-5.43	99.88	-5.43	9.7 x 10^3
(tCt)(AM)$_2$ -2	-18.74	3.56	3.73	-1.44	0.12		
(cCt)(AM)$_2$ -1	-21.21	5.12	5.20	-4.51	48.04	-4.95	4.3 x 10^3
(cCt)(AM)$_2$ -2	-20.83	3.30	3.40	-4.56	51.96		

The structural data reported in Table 4 and the large negative electronic binding energies reported in Table 5 demonstrate that all the five conformers of OA form stable hydrogen-bonded molecular clusters with AM under ambient conditions and if the gas-phase molecular concentrations are sufficient, these clusters may further nucleate and grow in size. Among the binary clusters, the lowest binding energy is obtained for the (cCt)(AM)−1 with $\Delta E_B = -13.57\ \mathrm{kcal/mol}$, followed by (cTt)(AM)−1 with $\Delta E_B = -12.76\ \mathrm{kcal/mol}$. Both cCt and cTt have same C_s symmetry and in both cases, AM interacts with one COOH group where the CO and OH are in cis configuration, Notably, neither cCt nor cTt is the lowest energy conformer of OA. In fact, cCt is the highest energy OA conformer with $\Delta E_R = 5.78\ \mathrm{kcal/mol}$ relative to the most stable cTc conformer. The binary cluster formed by the lowest energy cTc conformer ranks third with $\Delta E_B = -11.89\ \mathrm{kcal/mol}$, closely followed by (tCt)(AM) and (tTt)(AM) with $\Delta E_B = -11.81\ \mathrm{kcal/mol}$ and $-11.79\ \mathrm{kcal/mol}$, respectively.

Concerning the total distortion energy, $E_D(T)$, of the binary clusters, it is found that (cTc)(AM) exhibits highest value with $E_D(T) = 4.39\ \mathrm{kcal/mol}$, which accounts for almost 37% of its binding energy, ΔE_B. In contrast, the most stable (cCt)(AM)−1 binary conformer has $E_D(T) = 2.63\ \mathrm{kcal/mol}$, constituting 19% of its ΔE_B. The (tCt)(AM) binary cluster has the lowest distortion energy with $E_D(T)$ =1.53 kcal/mol, followed very closely by (tCt)(AM) with $E_D(T) = 1.55\ \mathrm{kcal/mol}$. In both clusters, $E_D(T)$ corresponds to 13% of the ΔE_B. Thus, the distortion energy of (cTc)(AM) is nearly three times that of (tCt)(AM), although their ΔE_B has almost the same magnitude. Furthermore, in all the binary clusters, the distortion energies of the individual OA monomers, E_D(OA) contribute to $95 - 99\%$ of E_D(T), which implies that the OA monomers undergo the majority of structural modifications during clustering. So, the lowest energy OA conformer, cTc experiences significantly higher structural strain compared to others, as its $E_D(T)$ is substantially higher than all other conformers. OA conformers with trans-COOH interacting with AM, suffer lesser distortion, benefiting from steric advantages over others.

Upon addition of thermal correction to electronic energy, all binary clusters exhibit negative values of binding free energy (ΔG), signifying the spontaneous formation of the cluster at the ambient temperature and pressure, assuming adequate monomer concentrations at the local. The order of thermodynamic stability aligns with that of ΔE_B, where the (cCt)(AM)−1 conformer demonstrates the highest stability with $\Delta G = -5.03\ \mathrm{kcal/mol}$, followed by (cTt)(AM)−1 and (cTc)(AM) with $\Delta G = -4.51\ \mathrm{kcal/mol}$ and $-3.65\ \mathrm{kcal/mol}$, respectively.

The K_{eq} values were calculated by using the formula: $K_{eq} = e^{-\Delta G_{MC}/RT}$, where $R = 8.314\ \mathrm{J/(mol \cdot K)}$ is the universal gas constant and $T = 298.15\ \mathrm{K}$ is the ambient temperature.

The equilibrium constant of a chemical system is a measure of the proportion of products and reactants present at a given equilibrium state. In atmospheric particle cluster formation, this constant is closely linked to changes in Gibb's free energy, with smaller free energy changes corresponding to larger equilibrium constants. This suggests that clusters are more likely to form and remain stable in the atmosphere. Hence, a higher equilibrium constant indicates a preference for cluster formation over dissociation.

For (cTc)(AM), (tTt)(AM) and (tCt)(AM), each having one conformation, $\Delta G_{\mathrm{MC}} = \Delta G$. On the other hand, (cTt)(AM) and (cCt)(AM) compositions possess two conformations each, but the Gibbs free energy difference between the two conformations exceeds $3\ \mathrm{kcal/mol}$ in both cases. As a result, in these two cases, the value of $\Delta G_{\mathrm{MC}} = \Delta G$ of the more stable conformation, this substantial free energy difference significantly influences the RPF of the clusters. The RPF of (cTc)(AM), (tTt)(AM) and (tCt)(AM) is 100% as they have one conformation each. However, in case of (cTt)(AM) and (cCt)(AM), where the difference between the ΔG values of conformation−1 and conformation−2 exceeds 3 kcal/mol, conformation−1 is the dominant fraction retaining over 99% of the total population. Furthermore, as can be observed from Table 3, the (cCt)(AM) binary cluster has the highest equilibrium constant (K_{eq}= 4.9×10^{3}), followed by (cTt)(AM) with $K_{eq} = 2.1 \times 10^{3}$, while (tCt)(AM) has the lowest value with $K_{eq} = 9.8 \times 10^{1}$ which implies that, under ambient conditions, the population of (cCt)(AM) cluster should be approximately 2.3 times greater than that of (cTt)(AM), and about 100 times greater than that of (tCt)(AM).

In case of ternary clusters of OA with AM, a total of 10 clusters is considered, with each cluster composition having two conformations. Similar to the previous case, all clusters exhibit large negative values of ΔE_B. However, they have a different profile this time, as the cCt and cTt conformers with C_s symmetry no longer constitute the most stable clusters in terms of binding energy. Instead, the ternary cluster with the lowest ΔE_B is (tCt)(AM)$_2$−1 with $\Delta E_B = -22.70\ \mathrm{kcal/mol}$, closely followed by (tTt)(AM)$_2$−1 with $\Delta E_B = -22.42\ \mathrm{kcal/mol}$. In both of these clusters the two AM monomers interact separately with the COOH moieties of OA, with no direct hydrogen bonding between them. The lower energy conformation, i.e., conformation−1 of the ternary clusters formed by cTc (the lowest energy OA conformer) and cCT (the highest energy OA conformer) have practically the same ΔE_B (around -21 kcal/mol), but the corresponding higher energy conformations, i.e., conformation−2 differ by almost 3 kcal/mol, with (cCt)(AM)$_2$−2 having higher stability.

The total distortion energy, $E_D(T)$, of the two conformations of (cTc)(AM)$_2$ generally have higher magnitudes compared to others, while the ternary clusters of tTt and tCt, both with C_{2v} symmetry, exhibit the lowest $E_D(T),$ as can be verified from **Table 5**. Similar to the binary clusters, distortion of the OA monomer alone in each ternary cluster contributes to $95 - 98\%$ of $E_D(T)$. Regarding the Gibb's free energy variation, all ternary clusters show negative values, with those of cTc, tTt and tCt, in particular, having the ΔG's closely similar in magnitudes. Specifically, (cTc)(AM)$_2$−1, (tTt)(AM)$_2$−1 and (tCt)(AM)$_2$−1 have ΔG in the range of -5.43 to -5.86 kcal/mol. On the other hand, the lower energy conformations, (cTc)(AM)$_2$−2, (tTt)(AM)$_2$−2 and (tCt)(AM)$_2$−2 exhibit ΔG's varying between -1.44 and -1.66 kcal/mol. Since the difference of ΔG between conformation−1 and conformation−2 of these cluster compositions exceeds 3 kcal/mol, it strongly impacts the RPF, rendering the population of conformation−2 negligible. However, in the case of (cCt)(AM)$_2$, where the ΔG values of the two conformations differ only by 0.05 kcal/mol with conformation−2 having the lower value, the RPF reflects a more balanced distribution, with conformation−1 occupying approximately 48% and conformation−2 around 52%. Regarding the equilibrium constants of the ternary clusters, (cTc)(AM)$_2$ exhibits the highest value ($K_{eq} = 2.0 \times 10^4$), closely followed by (tTt)(AM)$_2$ with $K_{eq} = 1.7 \times 10^4$, suggesting that both should have similar relative populations under ambient conditions. Further considering the K_{eq} values of the other ternary clusters, it is evident that the population of (cTc)(AM)$_2$ should be nearly double of that of (tCt)(AM)$_2$ and about five times greater than that of (cCt)(AM)$_2$.

4.3 Clusters of Oxalic Acid and Sulfuric Acid

In this section we analyze the structural and thermochemical properties of the binary and ternary clusters formed by each of the five OA conformers (cTc, cTt, tTt, tCt, cCt) with SA at ambient condition. The configurational space of OA-SA system is larger than that of OA-AM since SA offers higher number of options for hydrogen bonding and we have larger numbers of cluster conformations for each OA conformation in this case. In general, we have obtained three to five different cluster conformations for each OA-SA binary compositions and six to eight conformations for each (OA)(SA)$_2$ trimer compositions, However, to be concise, we have selected three conformations of each binary cluster composition and five conformations of each ternary composition, primarily on the basis of lowest electronic energy. The variation of Gibbs free energy or structural distinction have also been considered in one or two cases. In order to exemplify, we illustrate in **Figure 7**, the all the conformers that we could obtain for (CTt)(SA)$_2$ cluster composition, out of which five were chosen for analysis.

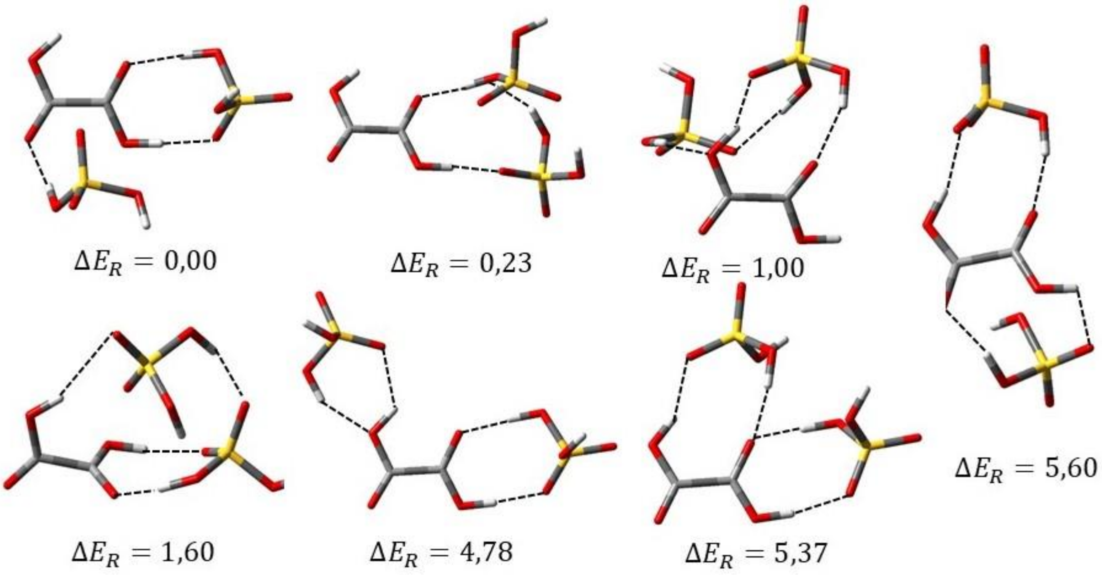

Figure 7: Equilibrium geometries of the (CTt)(SA)$_2$ conformers, optimized at the MO6-2X/6-311++G(3df,3pd) level. The dashed lines represent the intermolecular hydrogen bonds. ΔE_R is the relative energy difference, in $\mathrm{kcal/mol}$, with respect to the lowest energy conformation.

Figure 8 exhibits the optimized geometries of the 15 binary (OA)(SA) clusters, with each OA conformer having three conformations. **Figure 9** displays the optimized structures of 25 ternary (OA)(SA)$_2$ cluster conformations with five for each OA conformer. Each row in the figures corresponds to the conformations of a particular composition, labeled according to the respective OA conformer nomenclature. The relative energy differences of the conformations, in $\mathrm{kcal/mol}$, are indicated in square bracket. The intermolecular HBs are indicated by black dashed lines, as in previous figures, with respective calculated bond lengths mentioned in the units of angstroms.

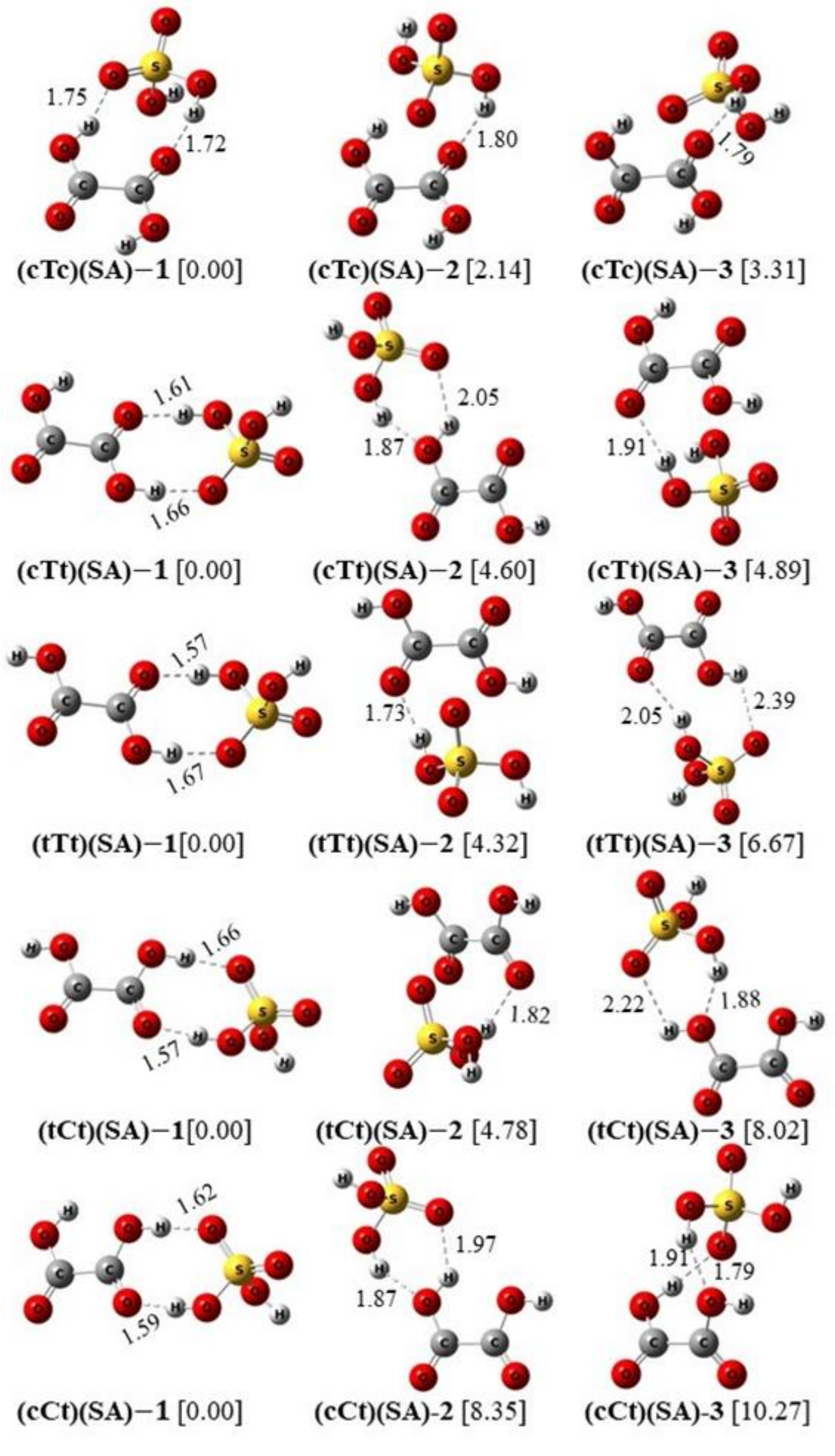
(cTc)(SA)−1 [0.00] (cTc)(SA)−2 [2.14] (cTc)(SA)−3 [3.31]
(cTt)(SA)−1 [0.00] (cTt)(SA)−2 [4.60] (cTt)(SA)−3 [4.89]
(tTt)(SA)−1[0.00] (tTt)(SA)−2 [4.32] (tTt)(SA)−3 [6.67]
(tCt)(SA)−1[0.00] (tCt)(SA)−2 [4.78] (tCt)(SA)−3 [8.02]
(cCt)(SA)−1 [0.00] (cCt)(SA)-2 [8.35] (cCt)(SA)-3 [10.27]

Figure 8: Equilibrium geometries of the stable (OA)(SA) cluster compositions. optimized at the MO6-2X/6-311++G(3df,3pd) level. The dashed lines represent the intermolecular hydrogen bonds with respective bond lengths given in angstrom. The numbers in square brackets represent the relative energy differences of the conformations in each cluster composition, in kcal/mol.

As can be seen from Figure 8, the $\mathrm{O-H\cdots O}$ HB lengths vary between 1.57 Å and 2.39 Å, with more than 80% of them remaining below 2.00 Å. Unlike the binary (OA)(AM) clusters, the HBs in (OA)(SA) clusters, with OA being the proton donor, are larger than those where OA acts as proton acceptor. Moreover, the differences between the bond lengths of these two types of HBs are also considerably smaller than those in (OA)(AM) systems. For example, in (cTc)(AM), we observe $R_{\mathrm{O-H\cdots N}} = 1.62$ Å (OA as proton donor) and $R_{\mathrm{N-H\cdots O}} = 2.25$ Å (OA as proton acceptor), while in (cTc)(SA), considering its lowest energy conformation, $R_{\mathrm{O\text{-}H\cdots O}} = 1.75$ Å (OA as proton donor) and $R_{\mathrm{O-H\cdots O}} = 1.72$ Å (OA as proton acceptor), with R denoting the HB length. Similar trend is observed in other clusters as well. The HB bond angles are also similar in case of the two $\mathrm{O-H\cdots O}$ HBs in the latter case. Thus, in case of (OA)(SA) clusters, both OA and SA contribute equivalently acting as simultaneous proton donor and acceptor.

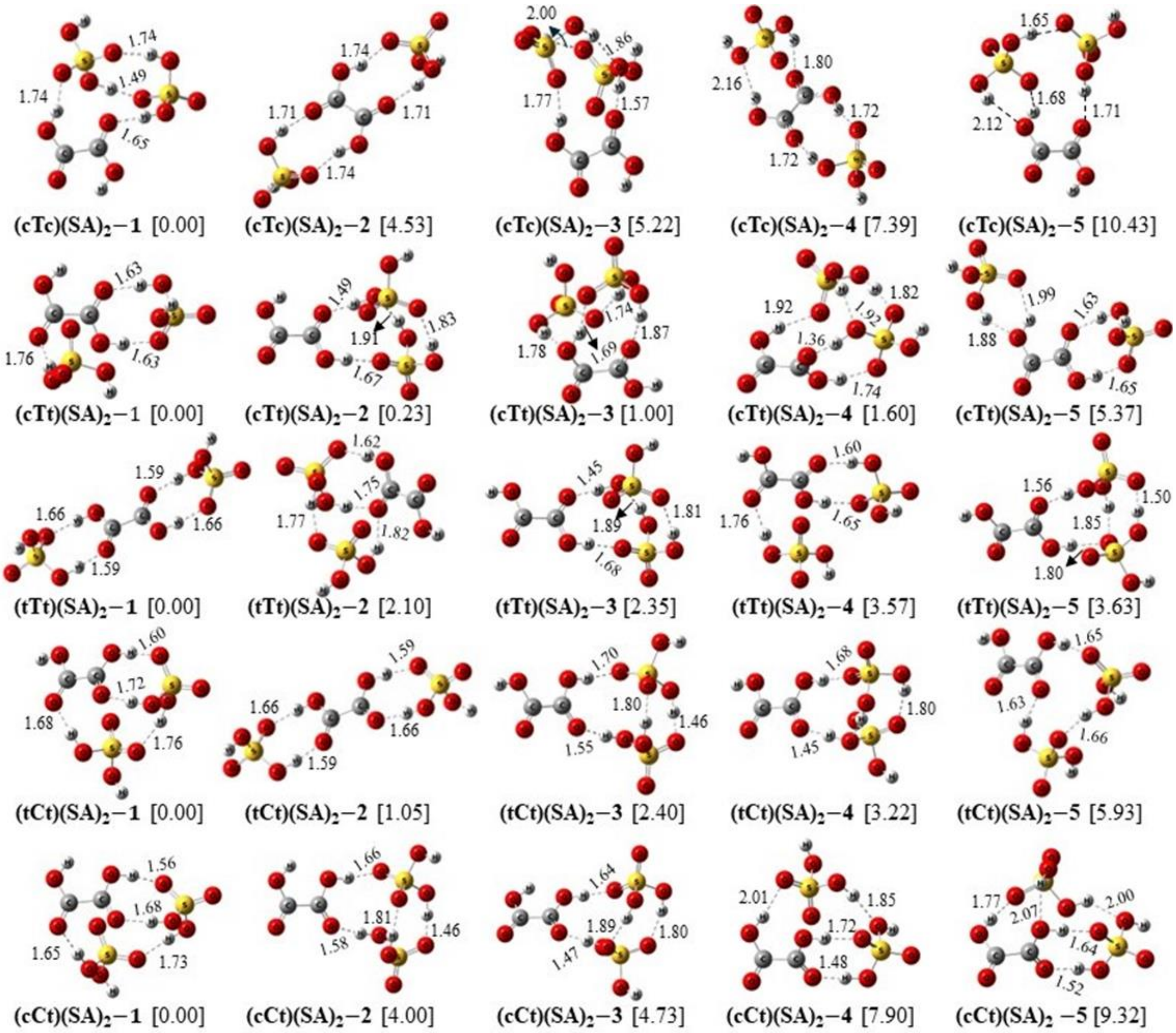

(cTc)(SA)$_2$−1 [0.00] **(cTc)(SA)$_2$−2** [4.53] **(cTc)(SA)$_2$−3** [5.22] **(cTc)(SA)$_2$−4** [7.39] **(cTc)(SA)$_2$−5** [10.43]

(cTt)(SA)$_2$−1 [0.00] **(cTt)(SA)$_2$**−2 [0.23] **(cTt)(SA)$_2$**−3 [1.00] **(cTt)(SA)$_2$**−4 [1.60] **(cTt)(SA)$_2$**−5 [5.37]

(tTt)(SA)$_2$−1 [0.00] **(tTt)(SA)$_2$**−2 [2.10] **(tTt)(SA)$_2$**−3 [2.35] **(tTt)(SA)$_2$**−4 [3.57] **(tTt)(SA)$_2$**−5 [3.63]

(tCt)(SA)$_2$−1 [0.00] **(tCt)(SA)$_2$**−2 [1.05] **(tCt)(SA)$_2$**−3 [2.40] **(tCt)(SA)$_2$**−4 [3.22] **(tCt)(SA)$_2$**−5 [5.93]

(cCt)(SA)$_2$−1 [0.00] **(cCt)(SA)$_2$**−2 [4.00] **(cCt)(SA)$_2$**−3 [4.73] **(cCt)(SA)$_2$**−4 [7.90] **(cCt)(SA)$_2$** −5 [9.32]

Figure 9: Equilibrium geometries of the stable (OA)(SA)$_2$ cluster compositions. optimized at the MO6-2X/6-311++G(3df,3pd) level. The dashed lines represent the intermolecular hydrogen bonds with respective bond lengths given in angstrom. The numbers in square brackets represent the relative energy differences of the conformations in each cluster composition, in kcal/mol.

As illustrated in **Figure 9**, the ternary (OA)(SA)$_2$ clusters, in general, are stabilized by the formation of three to five intermolecular HBs. Depending on the positions of the two SA molecules around OA, the later may have direct participation in the formation of two to four HBs. The $\mathrm{O-H\cdots O}$ HB lengths range between 1.35 Å and 2.16 Å, with 93% of them remaining below 2.00 Å and almost 70% below 1.80 Å. The average HB angles of the ternary cluster compositions, except (cTc)$(SA)_2$, are larger than that of corresponding binary clusters. For example, the average HB angle of the binary (tCt)(SA) conformers is $154.8°$, while in (tCt)$(SA)_2$, it is $174.2°$. In (cTc)(SA) and (cTc)$(SA)_2$ the average bond angle remains around $161°$.

The proton-donor $\mathrm{O-H}$ groups of both OA and SA suffer strong red-shift upon cluster formation. If we consider the lowest energy conformation of each binary (OA)(SA) cluster compositions, the average red-shift suffered by OH of OA is $504\ \mathrm{cm^{-1}}$, with cTc being the only OA conformer having a red-shift below this average. On the other hand, the average red-shift experienced by the OH of SA in these same systems is $712\ \mathrm{cm^{-1}}$. Thus, although cTc is the lowest energy OA monomer, its binary clusters with SA demonstrate weaker HB strength compared to others and in all clusters, SA appears as stronger proton-donor. However, in ternary (OA)$(SA)_2$ clusters, the average red-shift OH of OA ($\sim 630\ \mathrm{cm^{-1}}$) is almost same as that of OH of SA ($\sim 620\ \mathrm{cm^{-1}}$) showing that OA participates more effectively in HB formation in ternary clusters.

In general, the red shifts observed in the OH stretching frequencies of OA in the (OA)(AM) and (OA)$(AM)_2$ clusters are significantly greater than those in the (OA)(SA) and (OA)$(SA)_2$ clusters. As an example, **Figure 10** illustrates the IR vibrational frequencies along with the corresponding relative intensities of the OH groups of the cTc monomer, both in its isolated form and when integrated into the binary and ternary clusters. Notably, the cTc conformer of OA has two OH groups, and they exhibit simultaneous symmetric and asymmetric stretching modes. The symmetric stretching mode, where both OH groups stretch in phase (simultaneously outward or inward), occurs at $3723\ \mathrm{cm^{-1}}$ with a minimal relative intensity of $0.01\ \mathrm{km/mol}$. The asymmetric stretching mode, where one OH group expands while the other contracts, occurs at $3727\ \mathrm{cm^{-1}}$ with a much stronger relative intensity of 307 km/mol. In other OA conformers also similar trend is observed.

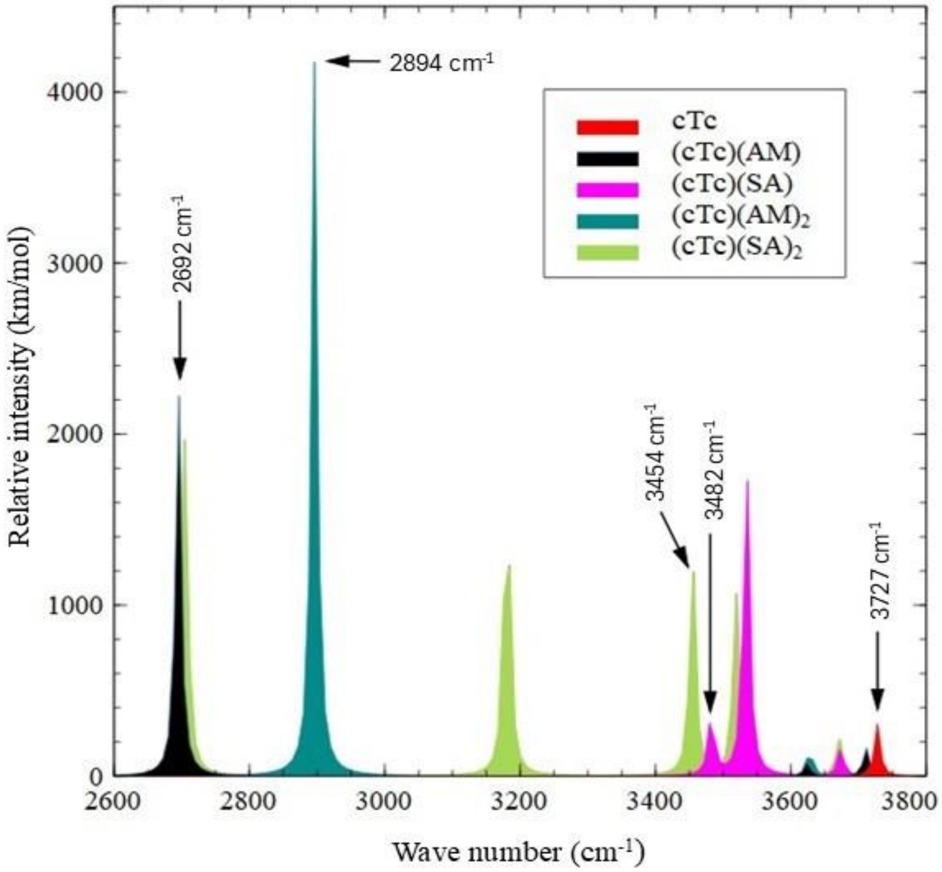

Figure 10: OH stretching frequencies of the cTc monomer, both in its isolated state and within binary and ternary clusters, with relative intensities.

In **Table 6** and **Table 7**, we report the relevant structural and spectroscopic parameters for the HBs present in (OA)(SA) binary clusters and $(OA)(SA)_2$ ternary clusters, respectively. The PD column indicates which molecule makes the role of proton donor, whether it is OA donating proton via its OH bond or SA donating proton via its OH bond. In **Table 7**, additional labelling "I" and "II" have been used to distinguish between multiple proton donor groups of OA and SA monomers, as illustrated in **Figure 11**. $R_{\mathrm{O-O}}$ is the distance between the oxygen atom of OA and that of SA forming the $\mathrm{O-H\cdots O}$ HB. $R_{\mathrm{(O)H\cdots O}}$ is the hydrogen bond length of the $\mathrm{O-H\cdots O}$ HB, indicated by the three dots. $\angle\mathrm{O-H\cdots O}$ is the HB angle of the $\mathrm{O-H\cdots O}$ HB. $\Delta R_{\mathrm{O-H}}$ is the elongation of the proton-donor $\mathrm{O-H}$ bond due to HB formation in cluster with respect to the corresponding monomer. $\nu_{\mathrm{O-H}}$ is the vibrational frequency (wave number) of the proton-donor $\mathrm{O-H}$ stretching mode. $\Delta\nu_{\mathrm{O-H}}$ is the frequency shift of the proton-donor $\mathrm{O-H}$ stretching mode as a result of HB formation. $\Delta\nu_{\mathrm{O-H}}(\mathrm{SA})$ is calculated with respect to the $\nu_{OH}^{as}(\mathrm{SA}) = 3821\ \mathrm{cm}^{-1}$ which has stronger intensity.

Table 6: Relevant structural parameters related to hydrogen bond formation in (OA)(SA) binary clusters obtained at the MO6-2X/6-311++G(3df,3pd) level of calculation.

	PD	$R_{\mathrm{O-O}}$ (Å)	$R_{\mathrm{(O)H\cdots O}}$ (Å)	$\angle \mathrm{O-H\cdots O}$ (degrees)	$\Delta R_{\mathrm{O-H}}$ (Å)	$\nu_{\mathrm{O-H}}$ (cm^{-1})	$\Delta\nu_{\mathrm{O-H}}$ (cm^{-1})
(cTc)(SA) −1	OA	2.695	1.746	161.2	0.012	3482	-246
	SA	2.679	1.719	164.8	0.016	3533	-288
(cTc)(SA) −2	SA	2.699	1.798	150.9	0.015	3520	-301
(cTc)(SA) −3	SA	2.736	1.790	160.8	0.016	3511	-310
(cTt)(SA) −1	OA	2.646	1.656	174.3	0.026	3269	-551
	SA	2.608	1.606	177.1	0.036	3065	-756
(cTt)(SA) −2	OA	2.709	2.052	122.8	0.008	3649	-124
	SA	2.768	1.866	152.1	0.011	3604	-217
(cTt)(SA) −3	SA	2.807	1.913	150.3	0.014	3561	-260
(tTt)(SA) −1	OA	2.659	1.671	174.5	0.024	3301	-531
	SA	2.581	1.573	177.4	0.042	2975	-846
(tTt)(SA) −2	SA	2.693	1.728	164.3	0.022	3359	-462
(tTt)(SA) −3	OA	2.676	2.390	96.4	0.001	3812	-20
	SA	2.922	2.053	146.9	0.012	3629	-192
(tCt)(SA) −1	OA	2.652	1.662	174.8	0.025	3280	-541
	SA	2.579	1.571	177.0	0.043	2971	-850
(tCt)(SA) −2	SA	2.740	1.817	154.8	0.018	3501	-320
(tCt)(SA) −3	OA	2.704	2.225	109.2	0.004	3760	-61
	SA	2.776	1.883	150.5	0.012	3624	-197
(cCt)(SA) −1	OA	2.614	1.619	174.9	0.031	3173	-651
	SA	2.592	1.589	175.4	0.040	3002	-819
(cCt)(SA) −2	OA	2.716	1.857	144.5	0.014	3553	-271
	SA	2.929	2.048	149.6	0.007	3708	-113
(cCt)(SA) −3	OA	2.692	1.972	128.8	0.010	3679	-151
	SA	2.763	1.869	150.6	0.012	3597	-224

Table 7: Relevant structural parameters related to hydrogen bond formation in (OA)(SA)$_2$ ternary clusters obtained at the MO6-2X/6-311++G(3df,3pd) level of calculation.

	PD	$R_{\mathrm{O-O}}$ (Å)	$R_{\mathrm{(O)H\cdots O}}$ (Å)	$\angle \mathrm{O-H\cdots O}$ (degrees)	$\Delta R_{\mathrm{O-H}}$ (Å)	$\nu_{\mathrm{O-H}}$ (cm^{-1})	$\Delta\nu_{\mathrm{O-H}}$ (cm^{-1})
(cTc)(SA)$_2$ −1	OA I	2.694	1.743	161.6	0.012	3454	-274
	SA I	2.641	1.647	175.7	0.029	3178	-643
(cTc)(SA)$_2$ −2	OA I	2.679	1.736	158.7	0.015	3501	-226
	OA II	2.679	1.736	158.7	0.015	3501	-226
	SA I	2.667	1.714	162.6	0.017	3417	-404
	SA II	2.667	1.714	162.6	0.017	3417	-404
(cTc)(SA)$_2$ −3	OA I	2.716	1.770	161.3	0.008	3581	-146
	SA I	2.571	1.574	171.4	0.038	3037	-784
(cTc)(SA)$_2$ −4	OA I	2.945	2.156	137.4	0.002	3701	-26
	OA II	2.667	1.715	160.7	0.017	3381	-346
	SA I	2.672	1.718	162.8	0.016	3536	-285
	SA II	2.694	1.795	150.4	0.016	3547	-274
(cTc)(SA)$_2$ −5	OA I	2.588	1.682	149.5	0.021	3277	-450
	SA I	2.920	2.115	139.3	0.005	3761	-60
	SA II	2.667	1.709	162.9	0.020	3413	-408
(cTt)(SA)$_2$ −1	OA I	2.625	1.631	173.9	0.030	3214	-605
	SA I	2.622	1.625	174.8	0.033	3091	-730
	SA II	2.706	1.745	163.5	0.021	3387	-434

(cTt)(SA)$_2$ −2	OA I	2.653	1.666	175.6	0.022	3376	-443
	OA I	2.517	1.491	152.1	0.062	2652	-1169
(cTt)(SA)$_2$ −3	OA I	2.616	1.690	154.1	0.023	3317	-456
	OA I	2.728	1.777	161.1	0.019	3435	-386
	SA II	2.767	1.865	152.7	0.008	3696	-125
(cTt)(SA)$_2$ −4	OA I	2.850	1.920	158.7	0.005	3684	-89
	OA II	2.740	1.740	165.8	0.017	3467	-352
	SA I	2.427	1.354	169.9	0.114	2010	-1811
(cTt)(SA)$_2$ −5	OA I	2.690	1.987	126.9	0.008	3596s, 3639as	-177,-134
	OA II	2.640	1.649	173.7	0.024	3133s, 3271as	-686,-548
	SA I	2.774	1.879	150.9	0.011	3596s, 3639as	-225,-182
	SA II	2.627	1.631	174.5	0.032	3133s, 3271as	-688,-550
(tTt)(SA)$_2$ −1	OA I	2.597	1.594	176.1	0.039	3260	-572
	OA II	2.597	1.594	176.1	0.039	3260	-572
	SA I	2.647	1.658	174.3	0.027	3012	-809
	SA II	2.647	1.658	174.3	0.027	3012	-809
(tTt)(SA)$_2$ −2	OA I	2.616	1.616	173.5	0.038	3032	-800
	OA I	2.706	1.764	159.2	0.017	3496s, 3446as	-336,-386
	SA II	2.711	1.817	149.2	0.020	3496s, 3446as	-336,-386
(tTt)(SA)$_2$ −3	OA I	2.665	1.680	174.4	0.021	3407	-424
	OA I	2.489	1.449	176.8	0.075	2451	-1370
(tTt)(SA)$_2$ −4	OA I	2.641	1.649	174.0	0.029	3240	-592
	OA I	2.598	1.595	175.5	0.038	3029	-792
	SA II	2.722	1.764	163.2	0.019	3420	-401
(tTt)(SA)$_2$ −5	OA I	2.770	1.797	170.6	0.043	3491	-341
	OA I	2.561	1.555	174.6	0.016	2966	-855
(tCt)(SA)$_2$ −1	OA I	2.599	1.595	173.5	0.041	2991	-830
	OA I	2.671	1.716	161.5	0.022	3385	-436
	SA II	2.652	1.667	168.0	0.032	3157	-664
(tCt)(SA)$_2$ −2	OA I	2.645	1.655	174.3	0.027	3257	-564
	OA II	2.645	1.655	174.3	0.027	3257	-564
	SA I	2.591	1.586	176.7	0.040	2993	-828
	SA II	2.591	1.586	176.7	0.040	2993	-828
(tCt)(SA)$_2$ −3	OA I	2.686	1.703	172.1	0.021	3362	-459
	OA I	2.557	1.552	173.9	0.042	2952	-869
(tCt)(SA)$_2$ −4	OA I	2.662	1.677	174.3	0.021	3383	-438
	OA I	2.486	1.445	177.2	0.076	2430	-1391
(tCt)(SA)$_2$ −5	OA I	2.639	1.653	170.8	0.028	3264	-557
	OA I	2.585	1.626	158.9	0.036	3108	-713
(cCt)(SA) −1	OA I	2.547	1.556	165.9	0.044	2954	-870
	SA I	2.665	1.681	172.4	0.024	3305	-516
	SA II	2.642	1.654	168.5	0.035	3102	-719
(cCt)(SA) −2	OA I	2.645	1.659	172.1	0.026	3267	-557
	SA I	2.573	1.576	171.6	0.037	3597	-224
(cCt)(SA) −3	OA I	2.627	1.637	175.5	0.026	3287	-537
	SA I	2.501	1.468	176.9	0.068	2548	-1273
(cCt)(SA) −4	OA I	2.697	1.720	170.2	0.020	3393	-431
	OA II	2.898	2.005	151.9	0.006	3734	-96
	SA I	2.513	1.482	178.5	0.065	2611	-1210
(cCt)(SA) −5	OA I	2.638	1.643	178.9	0.030	3213	-611
	OA II	2.734	1.766	171.7	0.010	3631	-199
	SA I	2.542	1.521	175.8	0.057	2746	-1075
	SA II	2.875	2.069	140.0	0.006	3737	-84

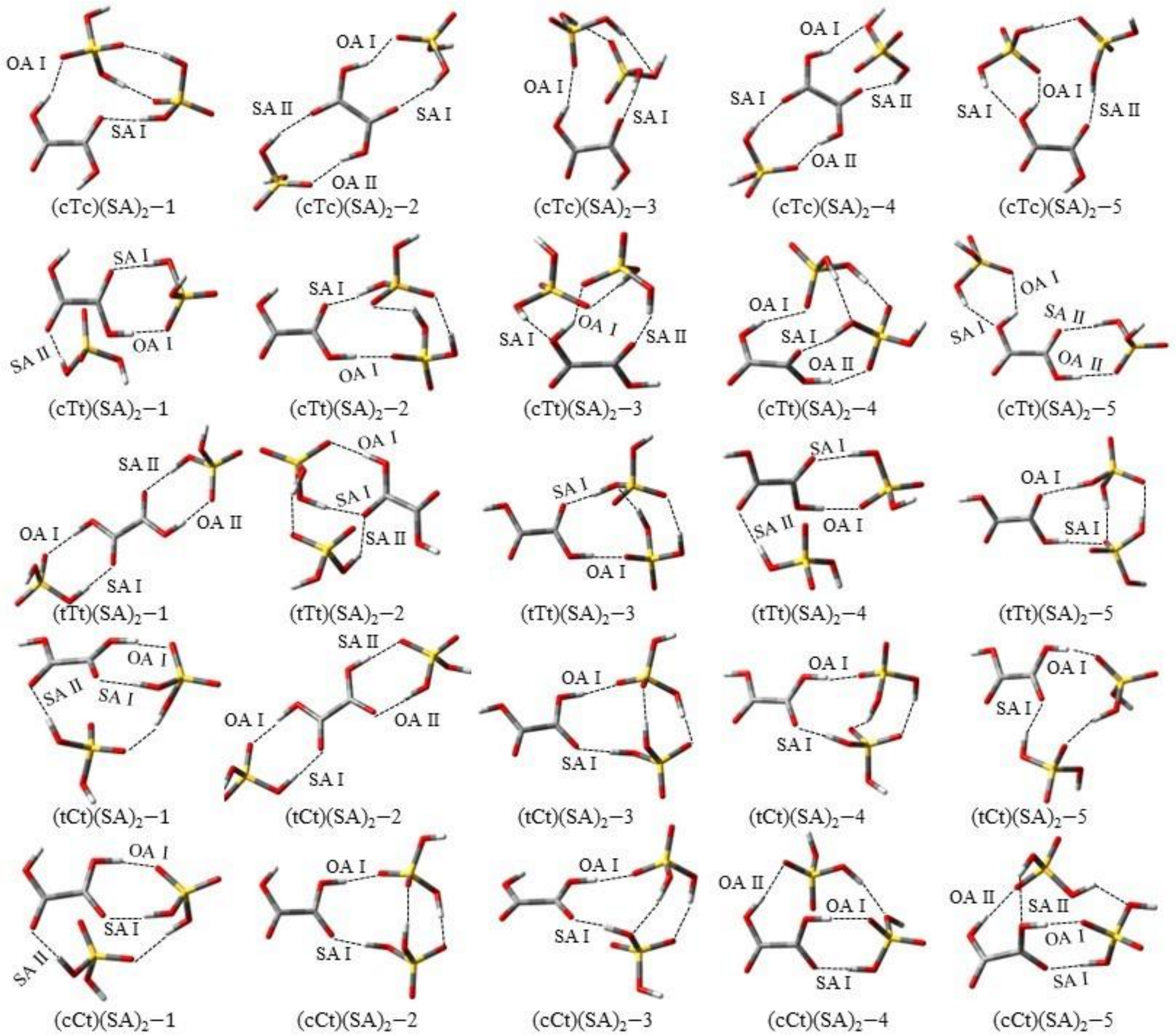

(cTc)(SA)$_2$−1 (cTc)(SA)$_2$−2 (cTc)(SA)$_2$−3 (cTc)(SA)$_2$−4 (cTc)(SA)$_2$−5

(cTt)(SA)$_2$−1 (cTt)(SA)$_2$−2 (cTt)(SA)$_2$−3 (cTt)(SA)$_2$−4 (cTt)(SA)$_2$−5

(tTt)(SA)$_2$−1 (tTt)(SA)$_2$−2 (tTt)(SA)$_2$−3 (tTt)(SA)$_2$−4 (tTt)(SA)$_2$−5

(tCt)(SA)$_2$−1 (tCt)(SA)$_2$−2 (tCt)(SA)$_2$−3 (tCt)(SA)$_2$−4 (tCt)(SA)$_2$−5

(cCt)(SA)$_2$−1 (cCt)(SA)$_2$−2 (cCt)(SA)$_2$−3 (cCt)(SA)$_2$−4 (cCt)(SA)$_2$−5

Figure 11: Geometries of the (OA)(SA)$_2$ ternary clusters obtained at the MO6-2X/6-311++G(3df,3pd) level of calculation with HB labels.

We now discuss the energetics of the different binary (OA)(SA) and ternary (OA)SA)$_2$ clusters, using the same approach as for the (OA)(AM) clusters. Calculated values of binding electronic energies (ΔE), binding free energy (ΔG) associated with different (OA)(SA) clusters at 298.15 K, in kcal/mol, along with their relative population fraction (RPF), the multi-conformation average binding free energy (ΔG_{MC}) and the equilibrium constants (ΔK_{eq}) of each cluster composition, obtained at M06-2X/6-311++G(3df,3pd) level, are reported in **Table 8** and **Table 9**, for the the binary and ternary clusters, respectively.

Table 8: Calculated values of binding electronic energies (ΔE), binding free energy ΔG) associated with different (OA)(SA) clusters at 298.15 K, in kcal/mol, along with their relative population fraction (RPF), the multi-conformation average binding free energy (ΔG_{MC}) and the equilibrium constants (K_{eq}) of each cluster composition obtained at M06-2X/6-311++G(3df,3pd) level.

	ΔE_B	$E_D(OA)$	$E_D(\mathrm{tot})$	ΔG	RPF	ΔG_{MC}	K_{eq}
(cTc)(SA) -1	-13.69	1.76	2.70	-3.39	99.10	-3.39	3.1×10^2
(cTc)(SA) -2	-11.54	1.09	1.96	-0.58	0.88		
(cTc)(SA) -3	-7.91	0.34	0.62	1.67	0.02		
(cTt)(SA) -1	-16.10	1.39	3.42	-5.30	99.70	-5.30	7.8×10^3
(cTt)(SA) -2	-11.50	1.62	2.27	-1.84	0.29		
(cTt)(SA) -3	-11.21	1.55	3.99	0.24	0.01		
(tTt)(SA) -1	-17.28	1.48	3.94	-6.69	99.99	-6.69	8.1×10^4
(tTt)(SA) -2	-12.97	0.66	1.61	-1.30	0.01		
(tTt)(SA) -3	-10.61	1.05	1.98	-0.26	0.00		
(tCt)(SA) -1	-17.61	1.53	4.13	-6.26	99.99	-6.26	3.9×10^4
(tCt)(SA) -2	-12.83	0.49	1.17	-0.41	0.01		
(tCt)(SA) -3	-9.58	0.61	0.95	2.41	0.00		
(cCt)(SA) -1	-18.03	1.74	4.40	-7.04	100.00	-7.04	1.5×10^5
(cCt)(SA) -2	-9.68	0.35	0.81	0.13	0.00		
(cCt)(SA) -3	-7.76	4.25	5.07	2.95	0.00		

All clusters of OA with SA display large negative ΔE_B values, as can be verified from the data reported in Tables 8 and 9. Among the conformations within each cluster composition, there is considerable variation in ΔE_B. Considering the average binding energy, $\langle \Delta E_B \rangle$ of each cluster composition in Table 8, the binary (OA)(SA) clusters can be arranged in the following order of increasing $\langle \Delta E_B \rangle$: (tTt)(SA) $[-13.62]$ < (tCt)(SA) $[-13.34]$ < (cTt)(SA) $[-12.94]$ < (cCt)(SA) $[-11.82]$ < (cTc)(SA) $[-11.05]$, where the numbers in the square brackets represent the values of $\langle \Delta E_B \rangle$ in kcal/mol. In case of ternary (OA)(SA)$_2$ clusters, this order is different, and it is as follows from Table 9: (cCt)(SA)$_2$ $[-35.51]$ < (tCt)(SA)$_2$ $[-33.24]$ < (tTt)(SA)$_2$ $[-31.92]$ < (cTt)(SA)$_2$ $[-28.74]$ < (cTc)(SA)$_2$ $[-27.33]$.

However, when considering the lowest energy conformer of each cluster composition, among the binary clusters, (cCt)(SA)-1 exhibits the least binding energy with $\Delta E_B = -18.03$ kcal/mol, while (cTc)(SA)-1 shows the highest value with $\Delta E_B = -13.69$ kcal/mol. Notably, among the five OA conformers, cTc has the lowest electronic energy while cCt has the highest. Thus, similar to the case of (OA)(AM) clusters, the highest energy OA conformer also forms a binary cluster with SA that has the lowest binding energy among all cluster compositions. The binding energy of (cCt)(SA)-1 is closely followed by (tCt)(SA)-1 and (tTt)(SA)-1 with ΔE_B values of -17.61 kcal/mol and -17.28 kcal/mol, respectively. In case of the ternary clusters also, the highest energy OA conformer forms the cluster (cCt)(SA)$_2$−1, that possesses the least binding energy with $\Delta E_B = -37.70\ \mathrm{kcal/mol}$.

Table 9: Calculated values of binding electronic energies (ΔE), binding free energy (ΔG) associated with different (OA)(SA)$_2$ clusters at $298.15\ \mathrm{K}$, in $\mathrm{kcal/mol}$, along with their with their relative population fraction (RPF), the multi-conformation average binding free energy (ΔG_{MC}) and the equilibrium constants (ΔK_{eq}) of each cluster composition obtained at M06-2X/6-311++G(3df,3pd) level.

	ΔE_B	$E_D(OA)$	$E_D(T)$	ΔG	RPF	ΔG_{MC}	K_{eq}
(cTc)(SA)$_2$−1	-32.84	1.92	12.57	-9.65	96.61	-9.67	1.3 x 10^7
(cTc)(SA)$_2$−2	-28.32	2.95	5.02	-7.67	3.38		
(cTc)(SA)$_2$−3	-27.62	2.19	7.23	-4.20	0.01		
(cTc)(SA)$_2$−4	-25.46	2.76	4.79	-2.92	0.00		
(cTc)(SA)$_2$−5	-22.42	2.00	7.45	-0.32	0.00		
(cTt)(SA)$_2$−1	-30.38	1.98	5.12	-7.01	60.15	-7.31	2.3 x 10^5
(cTt)(SA)$_2$−2	-30.15	1.91	8.58	-6.66	33.10		
(cTt)(SA)$_2$−3	-28.78	1.71	6.41	-5.26	3.15		
(cTt)(SA)$_2$−4	-29.38	10.39	23.55	-5.28	3.23		
(cTt)(SA)$_2$−5	-25.01	1.64	4.01	-4.00	0.37		
(tTt)(SA)$_2$−1	-34.25	2.96	7.56	-11.82	99.43	-11.83	4.8 x 10^8
(tTt)(SA)$_2$−2	-32.15	3.28	11.42	-7.70	0.10		
(tTt)(SA)$_2$−3	-31.90	2.17	9.81	-8.56	0.40		
(tTt)(SA)$_2$−4	-30.68	1.89	5.09	-7.11	0.03		
(tTt)(SA)$_2$−5	-30.63	1.25	10.04	-7.19	0.04		
(tCt)(SA)$_2$−1	-35.76	3.29	13.57	-10.08	6.53	-11.70	3.9 x 10^8
(tCt)(SA)$_2$−2	-34.71	2.90	7.59	-11.65	92.27		
(tCt)(SA)$_2$−3	-33.36	1.63	17.43	-8.91	0.91		
(tCt)(SA)$_2$−4	-32.54	2.26	10.05	-8.25	0.30		
(tCt)(SA)$_2$−5	-29.83	1.71	7.28	-5.22	0.00		
(cCt)(SA)$_2$−1	-37.70	4.36	13.19	-13.31	99.41	-13.31	5.9 x 10^9
(cCt)(SA)$_2$−2	-33.70	1.81	17.50	-10.16	0.49		
(cCt)(SA)$_2$−3	-32.98	2.40	9.77	-9.24	0.10		
(cCt)(SA)$_2$−4	-29.80	2.92	8.67	-5.83	0.00		
(cCt)(SA)$_2$−5	-28.38	5.78	11.18	-4.57	0.00		

Considering the thermal correction to electronic energy, we observe that not all binary cluster conformers show thermodynamic stability at ambient temperature. In case of the three conformers of (cCt)(SA) composition, for example, only (cCt)(SA)−1 has negative ΔG, and it is also the one with lowest binding free energy among all the binary clusters considered here, with $\Delta G = -7.04\ \mathrm{kcal/mol}$. Only binary composition whose all conformations show thermodynamic stability at room temperature is (tTt)(SA), with (tTt)(SA)−1 having the binding free energy very close to (cCt)(SA)−1 with $\Delta G = -6.69\ \mathrm{kcal/mol}$. The binary cluster of cTc, the lowest energy

OA monomer, with SA shows least thermodynamic stability. The ternary clusters of OA with SA, however, show a different nature where all the five conformations of each cluster composition show stability at room temperature with negative ΔG values of varying magnitudes. The lowest energy conformation of each cluster composition has the lowest ΔG of the respective group except (tCt)(SA)$_2$ where second lowest conformer (tCt)(SA)$_2$−2 shows lowest value with $\Delta G = -11.65$ kcal/mol, followed by (tCt)(SA)$_2$−1 with $\Delta G = -10.08$ kcal/mol.

Considering the ΔG_{MC} values, the ternary clusters can be arranged in the order of increasing thermodynamical stability as follows: (cTt)(SA)$_2$ $<$ (cTc)(SA)$_2$ $<$ (tCt)(SA)$_2$ $<$ (tTt)(SA)$_2$ $<$ (cCt)(SA)$_2$. Thus, in both the binary and ternary clusters of OA with SA, cCt, the highest energy OA conformer, forms the most thermodynamically stable interaction. Overall, the ΔG values of the (OA)(SA)$_2$ clusters are much lower than those of the binary (OA)(SA) clusters, indicating higher stability for the ternary clusters.

Regarding the relative population fraction (RPF) of the binary (OA)(SA) clusters, a similar trend to that observed in (OA)(AM) clusters is observed, with the lowest energy conformer of each cluster dominating the population with an RPF of nearly 100%. In the case of (OA)(SA) trimers, a similar trend is observed, with the lowest ΔG conformer of each cluster composition having the dominant RPF. This dominance is over 90% in all cases except for (cTt)(SA)$_2$, where due to the small difference in ΔG values between (cTt)(SA)$_2$−1 and (cTt)(SA)$_2$−2, the RPFs of these two conformers are 60.15% and 33.10%, respectively. Both in the binary and ternary clusters of OA with SA, the conformers cCt , tTt and tCt of OA form the three most stable clusters, as indicated by their low ΔG values, which correspond to the highest equilibrium constants. Among the binary clusters, (cCt)(SA) shows the highest equilibrium constant ($K_{eq} = 1.5 \times 10^5$), followed by (tTt)(SA) and (tCt)(SA) with K_{eq} values of 8.1×10^4 and 3.9×10^4, respectively. Therefore, under ambient conditions, (cCt)(SA) population should be nearly double that of (tTt)(SA) and about three times greater than that of (tCt)(SA). For the ternary clusters, [(cCt)(SA)$_2$ shows the highest equilibrium constant ($K_{eq} = 5.9 \times 10^9$) which is 13 and 15 times higher than those (tTt)(AM)$_2$ and (tCt)(AM)$_2$, respectively.

4.4 Successive Cluster Formation

The previous discussions on the binding free energy of the clusters assumed that monomers interact simultaneously to form clusters. However, clusters can also form through successive interactions, where a pre-formed molecular cluster interacts with another free molecule to create a larger cluster. In our case, a ternary $(OA)(AM)_2$ cluster may form from the interaction of a binary (OA)(AM) cluster with an AM monomer. Similarly, a ternary $(OA)(SA)_2$ cluster may form out of the interaction between any conformation (OA)(SA) and SA. Since successive cluster formation refers to the sequential process by which molecular clusters form, grow, and evolve in the atmosphere, it is relevant to atmospheric nucleation and new particle formation.

Table 10 presents the different possible pathways for forming $(OA)(AM)_2$ through successive cluster formation, which is relevant to the growth of cluster size. Successive binding free energies (ΔG_S) are calculated for all the five ternary $(OA)(AM)_2$ clusters, corresponding to the five OA conformers, assuming that any conformation of a ternary cluster composition can be formed from the hydrogen bonded interaction of one AM monomer with any of the corresponding binary composition.

Table 10: Successive binding free energies (ΔG_S) for the formation of various $(OA)(AM)_2$ ternary clusters, derived from the addition of an AM monomer to pre-existing (OA)(AM) binary clusters.

Final channel (ternary cluster)	Initial channel (binary cluster + AM)	ΔG_S (kcal/mol)
$(cTc)(AM)_2-1$	(cTc)(AM) + AM	-2.21
$(cTc)(AM)_2-2$		1.99
$(cTt)(AM)_2-1$	(cTt)(AM)-1 + AM	-2.81
	(cTt)(AM)-2 + AM	0.83
$(cTt)(AM)_2-2$	(cTt)(AM)-1 + AM	-1.56
	(cTt)(AM)-2 + AM	2.08
$(tTt)(AM)_2-1$	(tTt)(AM) + AM	-2.36
$(tTt)(AM)_2-2$		1.87
$(tCt)(AM)_2-1$	(tCt)(AM) + AM	-2.72
$(tCt)(AM)_2-2$		1.27
$(cCt)(AM)_2-1$	(cCt)(AM)-1 + AM	0.52
	(cCt)(AM)-2 + AM	-2.88
$(cCt)(AM)_2-2$	(cCt)(AM)-1 + AM	0.47
	(cCt)(AM)-2 + AM	-2.93

In the case of simultaneous cluster formation, as shown in **Table 10**, all 10 ternary structures show negative ΔG values, with conformation−1 consistently having a significantly lower ΔG than conformation−2, except in $(cCt)(AM)_2$. However, in successive cluster formation, not all binding free energies (ΔG_S) are negative, indicating some selectivity or preference. For binary compositions with a single conformation − (cTc)(AM), (tTt)(AM) and (tCt)(AM) − only for the formation of (cTc)$(AM)_2$−1, (tTt)$(AM)_2$−1 and (tCt)$(AM)_2$−1 shows negative ΔG_S values. These are the ternary conformations with lower ΔG of simultaneous cluster formation within their respective compositions. On the other hand, for binary compositions with two conformations, only the one with lower ΔG is capable of forming a ternary cluster with negative ΔG_S. For example, theoretically, both (cCt)$(AM)_2$−1 and (cCt)$(AM)_2$−2 could be formed from either (cCt)(AM)−1 or (cCt)(AM)−2 via successive cluster formation. However, since ΔG[(cCt)(AM)−2] $<$ ΔG[(cCt)(AM)−1], the thermodynamically favorable cluster formation pathways are (cCt)(AM)-2 + AM → (cCt)$(AM)_2$−1 with $\Delta G = -2.88$ kcal/mol and (cCt)(AM)-2 + AM → (cCt)$(AM)_2$−2 with $\Delta G = -2.93$ kcal/mol. Thus, (cCt)(AM)-2 can spontaneously grow in size through successive cluster formation, while (cCt)(AM)-1 cannot. Similarly, (cTt)(AM)−1 can grow through successive cluster formation due to its lower ΔG value, while (cTt)(AM)−2 cannot.

Similarly, to the (OA)$(AM)_2$ clusters, an analysis of successive cluster formation was conducted for the (OA)$(SA)_2$ clusters, under the same theoretical assumption that any conformation of a ternary cluster composition can form through the hydrogen-bonded interaction between an SA monomer and any corresponding binary cluster conformer. Considering that we have five ternary and three binary conformations for each OA monomer, we have a large number of possibilities of cluster formation channels. The calculated values of successive binding free energies (ΔG_S) for all conformations of the five ternary (OA)$(SA)_2$ cluster compositions, corresponding to the five OA conformers, are presented in Table 11. As seen from the table, unlike the case of (OA)$(AM)_2$ clusters, selectivity is much less pronounced in the successive formation of (OA)$(SA)_2$ clusters, with the majority of successive interactions yielding negative ΔG_S values. This suggests that clusters of SA with any OA conformer can grow in size more readily than the corresponding AM clusters.

Table 11: Successive binding free energies (ΔG_S), in kcal/mol, for the formation of various (OA)(SA)$_2$ ternary clusters, derived from the addition of an SA monomer to the pre-existing (OA)(SA) binary clusters.

Final Channel	Inicial Channel	ΔG_S	Final Channel	Final Channel	ΔG_S
(cTc)(SA)$_2$−1	(cTc)(SA)−1 + SA	-6.27	(cTt)(SA)$_2$−1	(cTt)(SA)−1 + SA	-1.71
	(cTc)(SA)−2 + SA	-9.07		(cTt)(SA)−2 + SA	-5.17
	(cTc)(SA)−3 + SA	-11.32		(cTt)(SA)−3 + SA	-7.25
(cTc)(SA)$_2$−2	(cTc)(SA)−1 + SA	-4.28	(cTt)(SA)$_2$−2	(cTt)(SA)−1 + SA	-1.36
	(cTc)(SA)−2 + SA	-7.08		(cTt)(SA)−2 + SA	-4.81
	(cTc)(SA)−3 + SA	-9.34		(cTt)(SA)−3 + SA	-6.90
(cTc)(SA)$_2$−3	(cTc)(SA)−1 + SA	-0.82	(cTt)(SA)$_2$−3	(cTt)(SA)−1 + SA	0.04
	(cTc)(SA)−2 + SA	-3.62		(cTt)(SA)−2 + SA	-3.42
	(cTc)(SA)−3 + SA	-5.87		(cTt)(SA)−3 + SA	-5.51
(cTc)(SA)$_2$−4	(cTc)(SA)−1 + SA	0.47	(cTt)(SA)$_2$−4	(cTt)(SA)−1 + SA	0.02
	(cTc)(SA)−2 + SA	-2.34		(cTt)(SA)−2 + SA	-3.44
	(cTc)(SA)−3 + SA	-4.59		(cTt)(SA)−3 + SA	-5.52
(cTc)(SA)$_2$−5	(cTc)(SA)−1 + SA	3.06	(cTt)(SA)$_2$−5	(cTt)(SA)−1 + SA	1.30
	(cTc)(SA)−2 + SA	0.26		(cTt)(SA)−2 + SA	-2.16
	(cTc)(SA)−3 + SA	-1.99		(cTt)(SA)−3 + SA	-4.24
(tTt)(SA)$_2$−1	(tTt)(SA)−1 + SA	-5.13	(tCt)(SA)$_2$−1	(tCt)(SA)−1 + SA	-3.82
	(tTt)(SA)−2 + SA	-10.53		(tCt)(SA)−2 + SA	-9.67
	(tTt)(SA)−3 + SA	-11.56		(tCt)(SA)−3 + SA	-12.49
(tTt)(SA)$_2$−2	(tTt)(SA)−1 + SA	-1.01	(tCt)(SA)$_2$−2	(tCt)(SA)−1 + SA	-5.39
	(tTt)(SA)−2 + SA	-6.41		(tCt)(SA)−2 + SA	-11.24
	(tTt)(SA)−3 + SA	-7.44		(tCt)(SA)−3 + SA	-14.06
(tTt)(SA)$_2$−3	(tTt)(SA)−1 + SA	-1.87	(tCt)(SA)$_2$−3	(tCt)(SA)−1 + SA	-2.65
	(tTt)(SA)−2 + SA	-7.26		(tCt)(SA)−2 + SA	-8.51
	(tTt)(SA)−3 + SA	-8.30		(tCt)(SA)−3 + SA	-11.32
(tTt)(SA)$_2$−4	(tTt)(SA)−1 + SA	-0.42	(tCt)(SA)$_2$−4	(tCt)(SA)−1 + SA	-1.99
	(tTt)(SA)−2 + SA	-5.81		(tCt)(SA)−2 + SA	-7.84
	(tTt)(SA)−3 + SA	-6.85		(tCt)(SA)−3 + SA	-10.66
(tTt)(SA)$_2$−5	(tTt)(SA)−1 + SA	-0.50	(tCt)(SA)$_2$−5	(tCt)(SA)−1 + SA	1.03
	(tTt)(SA)−2 + SA	-5.89		(tCt)(SA)−2 + SA	-4.82
	(tTt)(SA)−3 + SA	-6.93		(tCt)(SA)−3 + SA	-7.63
(cCt)(SA)$_2$−1	(cCt)(SA)−1 + SA	-6.26			
	(cCt)(SA)−2 + SA	-16.25			
	(cCt)(SA)−3 + SA	-13.44			
(cCt)(SA)$_2$−2	(cCt)(SA)−1 + SA	-3.12			
	(cCt)(SA)−2 + SA	-13.10			
	(cCt)(SA)−3 + SA	-10.29			
(cCt)(SA)$_2$−3	(cCt)(SA)−1 + SA	-2.20			
	(cCt)(SA)−2 + SA	-12.19			
	(cCt)(SA)−3 + SA	-9.38			
(cCt)(SA)$_2$−4	(cCt)(SA)−1 + SA	1.22			
	(cCt)(SA)−2 + SA	-8.77			
	(cCt)(SA)−3 + SA	-5.96			
(cCt)(SA)$_2$−5	(cCt)(SA)−1 + SA	2.47			
	(cCt)(SA)−2 + SA	-7.52			
	(cCt)(SA)−3 + SA	-4.71			

4.5 Atmospheric Relevance of the Binding Free Energies

Determining the concentrations of various binary and ternary clusters of OA with AM and SA under realistic atmospheric conditions is of interest regarding the atmospheric relevance of these systems. These concentrations can serve as potential indicators of their presence in the atmosphere. The equilibrium constants (K_{eq}) for the formation of these clusters from simultaneous agglomeration of the respective monomers, derived from their standard multiple-component binding free energies (ΔG at 298.15K and 1 atm.) and presented in Tables 5, 8 and 9, can be utilized for this analysis.

As has been discussed previously in the literature [112-115], K_{eq} can also be defined for a cluster formation reaction like $\mathrm{OA} + n\mathrm{X} \rightarrow (\mathrm{OA})(\mathrm{X})_n$ as:

$$K_n = \frac{[(\mathrm{OA})(\mathrm{X})_n]}{[\mathrm{OA}] \cdot [X]^n}$$

In the present case, $\mathrm{X} = \mathrm{AM}$ or SA and $n = 1, 2$. [OA], [X] and $[(\mathrm{OA})(\mathrm{X})_n]$ are the vapor pressures of OA, X and their cluster $(\mathrm{OA})(\mathrm{X})_n$, respectively. With this we can determine the percentage population fraction (%PF) of the OA clusters with respect to the OA monomer as:

$$\%PF = \frac{[(\mathrm{OA})(\mathrm{X})_n]}{[\mathrm{OA}]} \times 100\% = K_n[\mathrm{X}]^n \times 100\%$$

Based on the reported atmospherically relevant gas-phase concentrations of OA, AM and SA, which are 5.0×10^{11}, 2.5×10^{10} and 5.0×10^{7} molecules/cm^3, respectively [112-115], we determine the $\%PF$ and the concentration of all the binary and ternary OA-clusters at the standard atmospheric condition of 298.15K and 1 atm. which are reported in Table 12.

As can be seen from the table, the binary clusters show some relevant concentrations and it varies in the range of 10^4-10^6 molecules/cm^3 for (OA)(AM) and 10^2-10^5 molecules/cm^3 for (OA)(SA) compositions. Thus, some of the binary cluster concentrations are comparable to gas-phase SA concentrations. The estimated concentration of 2.39×10^5 molecules/cm^3 for (cTc)(AM) is also comparable with 8.02×10^5 molecules/cm^3 obtained for the same system previously by PW91PW91/6-311++G(3df,3pd) level of theory [114]. Calculated concentrations of the ternary clusters are considerably smaller, with the (cCt)(SA)$_2$ composition showing the maximum value.

Table 12: Calculated values of the percentage population fraction (%PF) and estimated concentrations, in molecules/cm^3, for different binary and ternary (OA)(AM) and (OA)(SA) cluster compositions at 298.15 K and 1 atm.

AM-containing cluster	%PF	[C] (molecules/cm^3)	SA-containing cluster	%PF	[C] (molecules/cm^3)
(cTc)(AM)	4.77×10^{-5}	2.39×10^{5}	(cTc)(SA)	6.24×10^{-8}	3.12×10^{2}
(cTt)(AM)	2.04×10^{-4}	1.02×10^{6}	(cTt)(SA)	1.57×10^{-6}	7.87×10^{3}
(tTt)(AM)	3.08×10^{-5}	1.54×10^{5}	(tTt)(SA)	1.65×10^{-5}	8.25×10^{4}
(tCt)(AM)	9.75×10^{-6}	4.87×10^{4}	(tCt)(SA)	7.98×10^{-6}	3.99×10^{4}
(cCt)(AM)	4.92×10^{-4}	2.46×10^{6}	(cCt)(SA)	2.98×10^{-5}	1.49×10^{5}
(cTc)(AM)$_2$	2.00×10^{-12}	9.99×10^{-3}	(cTc)(SA)$_2$	5.15×10^{-15}	2.58×10^{-5}
(cTt)(AM)$_2$	5.85×10^{-14}	2.83×10^{-4}	(cTt)(SA)$_2$	9.55×10^{-17}	4.77×10^{-7}
(tTt)(AM)$_2$	1.66×10^{-12}	8.30×10^{-3}	(tTt)(SA)$_2$	1.98×10^{-13}	9.91×10^{-4}
(tCt)(AM)$_2$	9.66×10^{-13}	4.83×10^{-3}	(tCt)(SA)$_2$	1.59 × 10-13	7.96×10^{-4}
(cCt)(AM)$_2$	4.29×10^{-13}	2.15×10^{-3}	(cCt)(SA)$_2$	2.42 × 10-12	1.21×10^{-2}

Although the binding free energies calculated at standard atmospheric conditions are useful to assess the thermodynamical stability of the molecular clusters from quantum thermochemistry point of view, they may not be sufficient to evaluate their atmospheric relevance as no atmospherically relevant molecules actually have a partial pressure of 1 atm [15]. Correction of ΔG by considering the effect of partial pressure of the reactant species may provide more realistic insight regarding the atmospheric relevance of these interactions which can be accomplished by the following general expression [15]:

$$\Delta G(p_1,\, p_2, \cdots,\, p_n) = \Delta G_{\text{ref}} - k_B T\left(1 - \frac{1}{n}\right)\sum_i^n \ln\left(\frac{p_i}{p_{\text{ref}}}\right)$$

Here n is the number of different monomers in the cluster, and p_i is the partial pressure of monomer i. In the present case, $n = 2$ as we consider the clusters of OA conformers either with AM or with SA, $p_{\text{ref}} = 1$ atm. and $\Delta G_{\text{ref}} = \Delta G_{\text{MC}}$, calculated at standard temperature and pressure and reported in **Tables 5, 8 and 9**. The above expression then reduces to:

$$\Delta G(p_{\text{OA}},\, p_{\text{X}}) = \Delta G_{\text{MC}} - \frac{1}{2}k_B T\left[\ln\left(\frac{p_{\text{OA}}}{p_{\text{ref}}}\right) + \ln\left(\frac{p_{\text{X}}}{p_{\text{ref}}}\right)\right]$$

where X is represents AM or SA monomer, p_{OA} is the partial pressure of OA and p_{X} is the partial pressure of either AM or SA. $\Delta G_{\text{MC(X)}}$ denotes the ΔG_{MC} values for clusters containing either AM or SA, depending on whether X corresponds to AM or SA. For the gas-phase concentrations of OA, AM and SA, mentioned above, the second term of the above equation figures out to be -11.3 kcal/mol and -13.1 kcal/mol, when X is AM and SA, respectively. Thus, at 298,15 K,

$\Delta G(p_{OA}, p_X)$ to be negative, which indicates a spontaneous cluster formation reaction in an atmospherically realistic condition, ΔG_{MC} values of the (OA)(AM)$_n$ and (OA)(SA)$_n$ clusters should be lower than -11.3 kcal/mol and -13.1 kcal/mol, respectively. Thus, from the ΔG_{MC} values for simultaneous cluster formation reported in **Tables 5, 8 and 9**, we observe that (cCt)(SA)$_2$, with $\Delta G_{MC} = -13.31$ kcal/mol, is the only cluster composition that is capable of having thermodynamical stability in realistic atmospheric condition at 298.15K. This is the same composition that showed highest concentration among the ternary clusters.

4.6 Interaction with Solar Radiation

The formation of hydrogen-bonded molecular clusters can significantly affect the Rayleigh scattering intensity compared to their respective monomers due to variations in polarizability and anisotropy besides different cooperative effects.

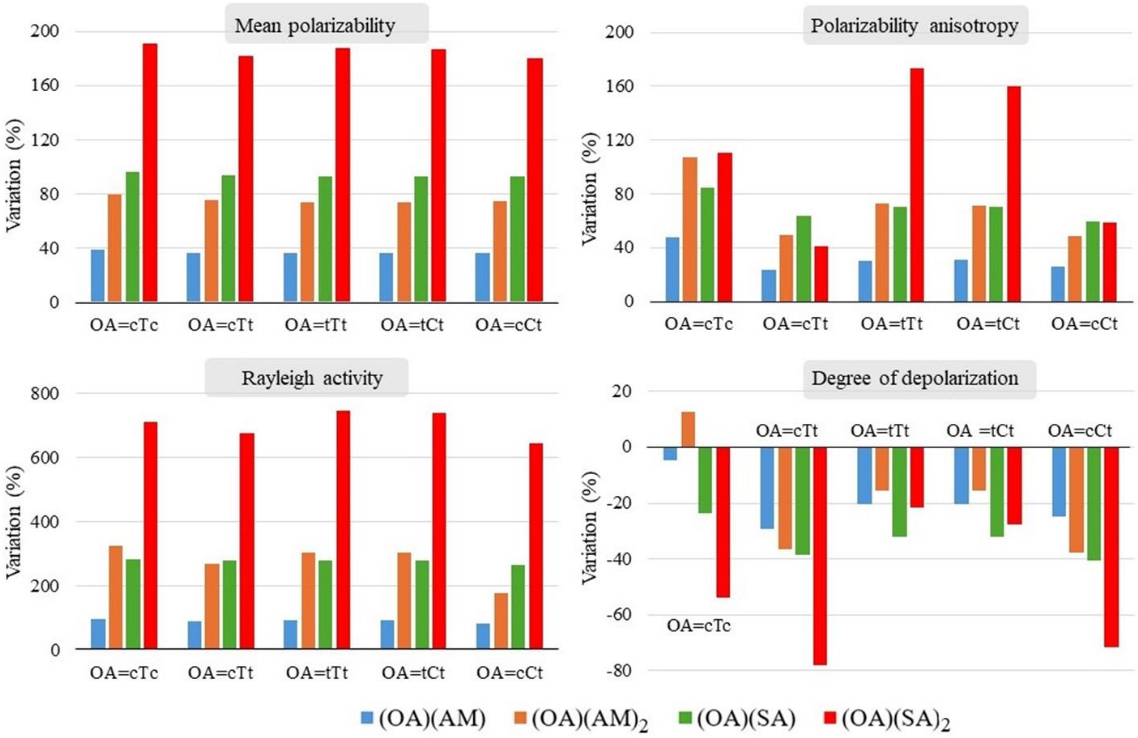

Figure 12: Percentage variation of mean dipole polarizability, anisotropy of the polarizability, Rayleigh activity and degree of depolarization for natural light in all the clusters, relative to respective OA monomers.

In Figure 12, we present the percentage variation of mean dipole polarizability ($\bar{\alpha}$), anisotropy of the polarizability ($\Delta\alpha$), Rayleigh Activity ($\Re$) and degree of depolarization (σ) for natural light in all the clusters, relative to respective OA monomers. The values of these parameters for the OA monomers are reported in **Table 3**.

Given that the clusters exhibit multiple conformations, we calculated the weighted average of each parameter for each cluster composition by considering the Boltzmann factor of the respective members, $\exp(-\Delta G_k/RT)$ and using the formula:

$$<x> = \frac{\sum_k x_k \exp\left(-\frac{\Delta G_k}{RT}\right)}{\sum_i \exp\left(-\frac{\Delta G_i}{RT}\right)}.$$

These average values, which are reported in **Table 13**, were then used to evaluate the percentage variations.

Table 13: Boltzman-averaged values of polarizability ($<\bar{\alpha}>$), anisotropy of polarizability ($<\Delta\alpha>$), Rayleigh scattering intensities ($<\mathfrak{R}>$) and degree of depolarization ($<\sigma>$), in $\mathrm{a.u.}$, of the OA conformers and their binary and ternary clusters with AM and SA

SYSTEM	$\bar{\alpha}$ $(\mathrm{a.u.})$	$\Delta\alpha$ $(\mathrm{a.u.})$	$\mathfrak{R}$ $(\mathrm{a.u.})$	σ $(\mathrm{a.u.})$
cTc	37.36	20.37	68189	0.044
(cTc)(AM)	52.03	30.07	133571	0.042
(cTc)(AM)$_2$	62.24	42.22	289888	0.050
(cTc)(SA)	73.51	37.64	261626	0.034
(cTc)(SA)$_2$	108.46	42.85	553347	0.020
cTt	37.84	19.72	67140	0.041
(cTt)(AM)	51.72	24.39	128106	0.029
(cTt)(AM)$_2$	66.33	29.54	247836	0.026
(cTt)(SA)	73.26	32.35	255091	0.025
(cTt)(SA)$_2$	106.62	27.81	521593	0.009
tTt	38.13	19.53	68103	0.039
(tTt)(AM)	52.09	25.43	130516	0.031
(tTt)(AM)$_2$	66.17	33.80	274999	0.033
(tTt)(SA)	73.56	33.34	257981	0.027
(tTt)(SA)$_2$	109.59	53.40	577597	0.031
tCt	38.16	19.60	68198	0.039
(tCt)(AM)	52.14	25.71	130950	0.031
(tCt)(AM)$_2$	66.30	33.61	276249	0.033
(tCt)(SA)	73.64	33.38	258540	0.027
(tCt)(SA)$_2$	109.44	50.98	573019	0.028
cCt	37.99	19.72	69983	0.040
(cCt)(AM)	51.84	29.94	129003	0.030
(cCt)(AM)$_2$	66.32	29.36	193433	0.025
(cCt)(SA)	73.32	31.39	254713	0.024
(cCt)(SA)$_2$	106.37	31.29	521897	0.011

Since polarizability depends on molecular volume, it is expected that polarizability will increase upon cluster formation. This is confirmed by the figure, which shows an almost linear increase in mean polarizability as we progress from OA to (OA)(AM) or (OA)(SA) and then to (OA)(AM)$_2$ or (OA)(SA)$_2$ with OA representing any of the five OA monomers. Given that SA has a larger volume than AM, clusters of OA with SA show much higher increase in mean polarizability compared to clusters of AM with OA. For all OA monomers, polarizability increases by nearly 37% when they form binary clusters with AM and by almost 94% when forming binary clusters with SA. Similarly, in ternary clusters, the increase in mean polarizability is almost 75% for interaction with AM and 185% when interacting with SA. Considering the weighted average value of mean polarizability, $<\bar{\alpha}>$, for each cluster composition individually, we find that the values are quite similar for five OA conformers. However, the anisotropy of polarizability does not exhibit the same regular and linear increase pattern as polarizability, although it increases upon cluster formation in all cases. Maximum increase of anisotropy, compared to the OA monomer, is observed for $(tTt)(SA)_2$, followed very closely by $(tCt)(SA)_2$. Conversely, the binary clusters formed between OA conformers and AM show less variation in $\Delta\alpha$, consistently remaining below 50% in all cases. The increase in Rayleigh intensity in the ternary clusters of OA conformers with SA (exceeding 600%) is significantly higher than that of all other clusters. For the $(OA)(AM)_2$ and (OA)(SA) cluster configurations, the increase of Rayleigh intensity ranges from 250% to 350% compared to the respective OA monomers, while in all (OA)(AM) binary clusters, the increase is limited to 100% or less. The degree of depolarization decreases in all clusters, except $(cTc)(AM)_2$, when compared to the respective OA monomers. Among the ternary $(OA)(AM)_2$ clusters, $(cTc)(AM)_2$ possesses the highest polarizability with $\alpha = 67.24\ \mathrm{a.u.}$ as well as the highest anisotropy with $\Delta\alpha = 42.23\ \mathrm{a.u}$, while the average α and $\Delta\alpha$ for this ternary group are $66.51\ \mathrm{a.u.}$ and $31.76\ \mathrm{a.u.}$, respectively. Consequently, the σ_n value of $(cTc)(AM)_2$ is high compared to others.

On a different perspective, comparison of $<\Re>$ values among the four cluster families (OA)(AM), $(OA)(AM)_2$, (OA)(SA) and $(OA)(SA)_2$, each having five members (compositions corresponding to the five OA conformers), either by composition or size, also reveals appreciable variations, as can be verified from the data reported in Table 12. For example, considering the increase in cluster size, the average increase in $\Re$ is 97% for $(OA)(AM)_2$ ternary clusters and 114% for $(OA)(SA)_2$ ternary clusters compared to their respective binary clusters, (OA)(AM) and (OA)(SA). Among the (OA)(AM) clusters, the highest increase (117%) is observed in $(cTc)(AM)_2$, while the lowest (50%) occurs in $(cCt)(AM)_2$. In case of $(OA)(SA)_2$, all compositions show over 100% increase in $\Re$ values going from binary to ternary cluster, with $(tTt)(SA)_2$, showing the highest increase (124%) while $(cTt)(SA)_2$ and $(cCt)(SA)_2$, showing lowest increase, both with 105%.

When comparing the compositions, clusters of OA with SA consistently show higher Rayleigh intensity than the clusters of OA with AM due to their larger molecular volume. On average, the $\mathfrak{R}$ values in binary (OA)(SA) and ternary (OA)(SA)$_2$ clusters are higher than their corresponding (OA)(AM) and (OA)(AM)$_2$ counterparts by 98% and 118%, respectively. However, there is a big difference in the individual behavior of the members. However, significant variation is observed among individual members. In the binary clusters, the largest difference is seen between (cTt)(SA) and (cTt)(AM), with the former's $\mathfrak{R}$ value being 99% higher, while the smallest variation of 96% is found between (cTc)(SA) and (cTc)(AM), indicating a consistent behavior with only a 3% difference between the maximum and minimum increases. On the other hand, for ternary clusters, the largest difference is observed between (cCt)(SA)$_2$ and (cCt)(AM)$_2$, with the former having 170% higher $\mathfrak{R}$ value, while the smallest difference, 91%, is observed between (OAA)(SA)$_2$ and (OAA)(AM)$_2$. Other ternary clusters in this series, (cTt)(SA)$_2$, (tTt)(AM)$_2$ and (tCt)(AM)$_2$, show increases of 111%, 110% and 107%, respectively, with respect to their corresponding (OA)(AM)$_2$ counterparts. These variations reflect considerable variation in molecular volume among ternary (OA)(SA) clusters

We can also analyze the increase in the Rayleigh scattering intensities due to clustering relative to all participating monomers using a supermolecular approach, where the excess Rayleigh intensity ($\Delta\mathfrak{R}$) will be determined by taking the difference in the scattering intensity between the cluster and the sum of the individual molecular intensities. Considering the weighted average value of Rayleigh intensity ($<\mathfrak{R}>$) of the clusters and the $\mathfrak{R}$ of the corresponding monomers, we again observe an appreciable of Rayleigh intensity increase upon clustering in all cases which is illustrated in **Figure 13.**

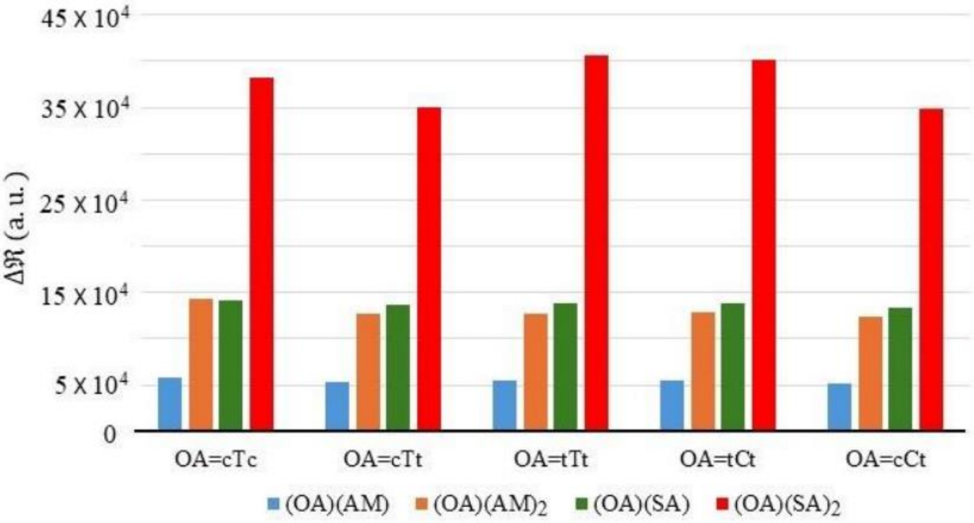

Figure 13: Excess Rayleigh scattering intensity ($\Delta\mathfrak{R}$) due to clustering of OA conformers with AM and SA.

In all the binary (OA)(AM) clusters, $\Delta\mathfrak{R}$ values remain consistently close to an average of 5.4×10^4 a.u., indicating that all the five OA conformer interacting with an ammonia molecule via hydrogen bonding acquire similar molecular volume, which leads to comparable polarizability and thus similar Rayleigh activities. A similar trend is observed in the ternary (OA)(AM)$_2$ clusters, albeit with a higher average $\Delta\mathfrak{R}$ of 13.0×10^4 a.u., reflecting that the intermolecular interaction increase consistently across all the compositions of ternary (OA)(AM)$_2$ clusters. The binary (OA)(SA) clusters also show a consistent increase in Rayleigh activity, with $\Delta\mathfrak{R}$ values are very similar to that those of the (OA)(AM)$_2$ clusters. In fact, (cTc)(AM)$_2$ and (cTc)(SA) exhibit identical increases in Rayleigh activity upon cluster formation, with $\Delta\mathfrak{R} = 14.2 \times 10^4$ a.u., suggesting that sulfuric acid interacts more strongly with oxalic acid than ammonia does. Moreover, this value also represents the highest increase in Rayleigh activity within both the (OA)(AM)$_2$ and (OA)(SA) families. The $\Delta\mathfrak{R}$ values of ternary (OA)(SA)$_2$ clusters are significantly higher than those of all other clusters, with an average value of 37.7×10^4 a.u. Unlike the other cluster families, the $\Delta\mathfrak{R}$ values of (OA)(SA)$_2$ show appreciable composition dependence, with (cCt)(SA)$_2$ having the lowest $\Delta\mathfrak{R}$ (34.8×10^4 a.u.) and (tTt)(SA)$_2$ cluster the highest (40.5×10^4 a.u.). This large increase in $\Delta\mathfrak{R}$ (OA)(SA)$_2$ compared to (OA)(SA) clusters indicates that increase of sulfuric acid molecules leads to significantly stronger intermolecular interactions.

On a different perspective, comparison of $< \mathfrak{R} >$ values among the four cluster families – (OA)(AM), (OA)(AM)$_2$, (OA)(SA) and (OA)(SA)$_2$ – each having five members (compositions corresponding to the five OA conformers), either by composition or size, also reveals appreciable variations, as can be verified from the data reported in **Table 13**. For example, Considering the increase in cluster size, the average increase in $\mathfrak{R}$ is 97% for (OA)(AM)$_2$ ternary clusters and 114% for (OA)(SA)$_2$ ternary clusters compared to their respective binary clusters – (OA)(AM) and (OA)(SA). Among the (OA)(AM) clusters, the highest increase (117%) is observed in (cTc)(AM)$_2$, while the lowest (50%) occurs in (cCt)(AM)$_2$. In case of (OA)(SA)$_2$, all compositions show over 100% increase in $\mathfrak{R}$ values going from binary to ternary cluster, with (tTt)(SA)$_2$, showing the highest increase (124%) while (cTt)(SA)$_2$ and (cCt)(SA)$_2$, showing lowest increase, both with 105%.

When comparing the compositions, clusters of OA with SA consistently show higher Rayleigh intensity than the clusters of OA with AM due to their larger molecular volume. On average, the $\mathfrak{R}$ values in binary (OA)(SA) and ternary (OA)(SA)$_2$ clusters are higher than their corresponding (OA)(AM) and (OA)(AM)$_2$ counterparts by 98% and 118%, respectively.

However, there is a big difference in the individual behavior of the members. However, significant variation is observed among individual members. In the binary clusters, the largest difference is seen between (cTt)(SA) and (cTt)(AM), with the former's $\Re$ value being 99% higher, while the smallest variation of 96% is found between (cTc)(SA) and (cTc)(AM), indicating a consistent behavior with only a 3% difference between the maximum and minimum increases. On the other hand, for ternary clusters, the largest difference is observed between (cCt)(SA)$_2$ and (cCt)(AM)$_2$, with the former having 170% higher $\Re$ value, while the smallest difference, 91%, is observed between (OAA)(SA)$_2$ and (OAA)(AM)$_2$. Other ternary clusters in this series - (cTt)(SA)$_2$, (tTt)(AM)$_2$ and (tCt)(AM)$_2$ - show increases of 111%, 110% and 107%, respectively, with respect to their corresponding (OA)(AM)$_2$ counterparts. These variations reflect considerable variation in molecular volume among ternary (OA)(SA) clusters.

Finally, examining the four cluster families individually, we observe that the OA conformer cTc forms the clusters with the highest Rayleigh activity in all families except for (OA)(SA)$_2$, it is (tTt)(SA)$_2$ that has the highest $\Re$ value in (OA)(SA)$_2$ family. Within the (OA)(AM) and (OA)(AM)$_2$ families, the lowest $\Re$ is observed in (cTt)(AM) and (cCt)(AM)$_2$, respectively, and within the (OA)(SA) and (OA)(SA)$_2$ families, (cCt)(SA) and (cTt)(SA)$_2$ exhibit the lowest values. The difference between the highest and lowest $\Re$ values in the (OA)(AM)$_2$ family is nearly 50%, the most significant variation within any family, followed by the (OA)(SA)$_2$ family, where the highest Rayleigh intensity is approximately 11% greater than the lowest.

5 CONCLUSIONS

In the present work, an extensive DFT calculation, employing the M06-2X/6-311++G(3df,3pd) model, was performed on the hydrogen-boned molecular interactions between five stable structural conformer of OA (cTc, cTt, tTt, tCt and cCt) and two important atmospheric nucleation precursor molecules, SA and AM. Several structural, thermodynamical, electrical, and spectroscopic parameters of the binary and ternary clusters mediated by oxalic acid were analyzed to gain insight into the hydrogen bonding nature of each OA conformers at standard atmospheric conditions. Multiple stable configurations for each kind of cluster composition, obtained by a combination of different quantum-chemical approach and chemical intuition, were considered for the analysis.

All OA conformers form strong hydrogen bonding with AM, showing thermodynamic stability at the ambient temperature, with average red shift of the OA O-H stretching mode of 934 (1088) cm^{-1} in binary (ternary) clusters. In ternary OA-AM clusters, the lowest energy OA conformer, cTc has the lowest binding free energy, followed very closely by other conformers like tTt and tCt. In OA-SA binary clusters also, this same conformer exhibits the lowest binding energy. Although some of the binary OA-SA clusters lack thermodynamic stability at ambient temperature, the ternary clusters of OA with SA, however, show a different nature where all the conformations of each cluster composition show stability with negative ΔG values of varying magnitudes. Considering the Multiple-conformation binding free energy, ΔG_{MC}, the ternary OA-SA clusters can be arranged in the order of increasing thermodynamical stability as follows: $(cTt)(SA)_2 < (cTc)(SA)_2 < (tCt)(SA)_2 < (tTt)(SA)_2 < (cCt)(SA)_2$, with the highest energy OA conformer, cCt once again showing lowest free binding energy. Overall, the ΔG values of the $(OA)(SA)_2$ clusters are much lower than those of the binary (OA)(SA) clusters, indicating higher stability for the ternary clusters. In general, OA-SA clusters have lower ΔG than the OA-AM clusters according to the present calculations. Comparing the ΔGs values for successive cluster formation both for $(OA)(AM)_2$ and $(OA)(SA)_2$, it is observed that the clusters of SA with OA are more likely to grow spontaneously.

Consideration of partial pressures of the monomers in the calculation of binding free energy reveals that the ΔG values of the (OA)(AM)n and (OA)(SA)n clusters should be lower than -11.3 kcal/mol and -13.1 kcal/mol, respectively, in order to have a thermodynamical stability in a atmospheric relevant condition at 298.15K. Among all the clusters considers, only $(cCt)(SA)_2$ satisfies this condition.

When comparing the Rayleigh activity of the clusters to that of the OA monomer, a notable increase in Rayleigh scattering intensity is observed due to the hydrogen-bonded molecular interactions present in all OA-mediated clusters. Specifically, the Rayleigh activity in the ternary $(OA)(SA)_2$ clusters shows a variation exceeding 600% with respect to OA, which is the highest and significantly greater than that observed in all other clusters. The determination of excess Rayleigh activity due to clustering, calculated using a supermolecular approach, also shows a significant increase in all cases. Notably, the $(OA)(SA)_2$ clusters exhibit considerably superior activity compared to other clusters. A less pronounced, but appreciable variation of Rayleigh activities is also observed when comparing the cluster among themselves, considering both size and composition. The average increase in Rayleigh scattering intensities observed going from binary to ternary clusters of OA, either with AM or SA, is close to 100%. Rayleigh intensities in $(OA)(SA)_2$ clusters exceed those of $(OA)(SA)_2$ clusters also by 100%, on average.

The results obtained provide insights into the behavior of each stable structural conformer of oxalic acid, particularly in terms of their interaction potential with key atmospheric molecules under standard atmospheric conditions. We believe that this information may be relevant in the studies of environmental processes, given that oxalic acid is one of the most abundant naturally occurring dicarboxylic acids in the atmosphere.

REFERENCES

[1] ZUHAD, R.; PERLMAN, R. L. Extreme weather events and the politics of climate change attribution. **Science Advances**, v. 8, n. 36, p. eabo2190, 2022.

[2] TRENBERTH, K. E. Climate change caused by human activities is happening and it already has major consequences, **Journal of Energy & Natural Resources Law**, v. 36, n. 4, p. 463-481, 2018.

[3] ABATZOGLOU, J. T.; WILLIAMS, A. P. Impact of anthropogenic climate change on wildfire across western US forests. **Proceedings of the National Academy of Sciences of the United States of America**, v. 113, n. 42, p. 11770–11775, 2016.

[4] MASSON-DELMOTTE, V. *et al*. Global Warming of 1.5 ºC. An IPCC Special Report on the impacts of global warming of 1.5 C above pre-industrial levels and related global greenhouse gas emission pathways, in the context of strengthening the global response to the threat of climate change. Sustainable development, and efforts to eradicate poverty. Available from: https://www.ipcc.ch/site/assets/uploads/sites/2/2019/06/SR15_Full_Report_High_Res.pdf, Access in: 10 december 2024, **Technical Report Intergovernmental Panel on Climate Change**, 2018.

[5] Climate Change 2021: The Physical Science Basis, Available from: https://www.ipcc.ch/report/ar6/wg1/, Access in: 10 december 2024, **Technical Report Intergovernmental Panel on Climate Change**, 2021**.**

[6] DUPUIS, J; KNOEPFEL, P. The adaptation policy paradox: the implementation deficit of policies framed as climate change adaptation. **Ecology and Society**, v. 18, n. 4, p. 31, 2013.

[7] ALDUNCE, P.; HANDMER, J.; BEILIN, R.; HOWDEN, M. Is climate change framed as ‘business as usual’ or as a challenging issue? The practitioners' dilemma. **Environment and Planning C: Government and Policy**, v. 34, n. 5, p. 999–1019, 2016.

[8] SEINFELD, J. H.; PANDIS, S. N. Atmospheric Chemistry and Physics: From Air Pollution to Climate Change. New York: Wiley, 1997.

[9] WALLACE, J. M.; HOBBS, P. V. Atmospheric Science: An Introductory Survey. Oxford: Elsevier, 2006.

[10] JACOB, D. J. Introduction to Atmospheric Chemistry. New Jersey: Princeton University Press, 1999.

[11] KULMALA, M. *et al*, Formation and growth rates of ultrafine atmospheric particles: a review of observations**. Journal of Aerosol Science**, v. *35*, n. 2, p. 143-176, 2004.

[12] KANAKIDOU, M., *et al*. Organic aerosol and global climate modelling: a review. **Atmospheric Chemistry and Physics**, v. 5, n. 4, p. 1053-1123, 2005.

[13] ELM, J. *et al*. Modeling the formation and growth of atmospheric molecular clusters: A review. **Journal of Aerosol Science**, v. 149, p. 105621, 2020.

[14] LEE, S.-H.; GORDON, H.; YU, H.; *et al*. New particle formation in the atmosphere: From molecular clusters to global climate. **Journal of Geophysical Research: Atmospheres**, v. 124, n. 13, p. 7098–7146, 2019.

[15] ELM, J. *et. al.* Quantum chemical modeling of organic enhanced atmospheric nucleation: A critical review. **WIREs Computational Molecular Science**, v. 13, n. 5, p. e1662, 2023.

[16] TOMASI, C.; FUZZI, S.; KOKHANOVSKY, A. (Eds.). Atmospheric aerosols: Life cycles and effects on air quality and climate. Weinheim: John Wiley & Sons, 2017.

[17] BOUCHER, O. Atmospheric Aerosols: Properties and Climate Impacts. Springer, 2015.

[18] ALVES, C. Aerossóis Atmosféricos: Perspectiva histórica, fontes, processos químicos de formação e composição orgânica. **Química Nova**, v. 28, n. 5, p. 859-870, 2005.

[19] CHARLSON, R. J. SEINFELD, J. H. NENES, A. *et al*. Reshaping the theory of cloud formation. **Science**, v. 292, n. 5524, p. 2025-2026, 2001.

[20] KAZIL, J. STIER, P. ZHANG, K. *et al*. Aerosol nucleation and its role for clouds and Earth's radiative forcing in the aerosol-climate model ECHAM5-HAM. **Atmospheric Chemistry and Physics**, v. 10, n. 22, p. 10733-10752, 2010.

[21] MAKKONEN, R.; ASMI, A.; KERMINEN, V. M. *et al*. Air pollution control and decreasing new particle formation lead to strong climate warming. **Atmospheric Chemistry and Physics**, v. 12, n. 3, p. 1515-1524, 2012.

[22] SAXON, A.; SANCHEZ, D. Air pollution and allergy: you are what you breathe. **Nature Immunology**, v. 6, n. 3, p. 223-226, 2005.

[23] PENTTINEN, P.; TIMONEN, K. L.; TIITTANEN, P. *et al*. Ultrafine particles in urban air and respiratory health among adult asthmatics. **European Respiratory Journal**, v. 17, n. 3, p. 428-435, 2001.

[24] OBERDORSTER, G.; UTELL, M. J. Ultrafine particles in the urban air: to the respiratory tract--and beyond? **Environmental Health Perspectives**, v. 110, n. 8, p. 440-441, 2002.

[25] KUANG, C.; RIIPINEN, I.; SIHTO, S. L. *et al.* An improved criterion for new particle formation in diverse atmospheric environments. **Atmospheric Chemistry and Physics**, v. 10, n. 17, p. 8469-8480, 2010.

[26] ZHANG, R.; KHALIZOV, A.; WANG, L. *et al*. Nucleation and growth of nanoparticles in the atmosphere. **Chemical Reviews**, v. 112, n. 3, p. 1957-2011, 2012.

[27] BZDEK, B. R.; JOHNSTON, M. V. New particle formation and growth in the troposphere. **Analytical Chemistry**, v. 82, n. 19, p. 7871-7878, 2010.

[28] NOVAKOV, T.; PENNER, J. E. Large contribution of organic aerosols to cloud-condensation-nuclei concentrations. **Nature**, v. 365, n. 6449, p. 823-826, 1993.

[29] HENSCHEL, H.; KURTÉN, T.; VEHKAMÄKI, H. Computational study on the effect of hydration on new particle formation in the sulfuric acid/ammonia and sulfuric acid/dimethylamine systems. **The Journal of Physical Chemistry A**, v. 120, n. 11, p. 1886-1896, 2016.

[30] KULMALA, M., *et al*. Direct observations of atmospheric aerosol formation from biogenic vapors. **Science**, v. 339, n. 6122, p. 943-946, 2013.

[31] KIRKBY, J., *et al*. Role of sulphuric acid, ammonia and galactic cosmic rays in atmospheric aerosol nucleation. **Nature**, v. 476, n. 7361, p. 429-433, 2011.

[32] ZHANG, R. Getting to the critical nucleus of aerosol formation. **Science**, v. 328, n. 5984, p. 1366-1367, 2010.

[33] ZHANG, R., *et al*. Atmospheric new particle formation enhanced by organic acids. **Science**. v. 304, n. 5676, p. 1487–90, 2004.

[34] NADYKTO, A. B.; YU, F. Strong hydrogen bonding between atmospheric nucleation precursors and common organics. **Chemical Physics Letters**, v. 435, n. 1-3, p.14-18, 2007.

[35] ZHAO, J.; KHALIZOV, A.; ZHANG, R.; MCGRAW, R. Hydrogen-bonding interaction in molecular complexes and clusters of aerosol nucleation precursors. **The Journal of Physical Chemistry A**, v. 113, n. 4, p. 680-689, 2009.

[36] MCGRAW, R.; ZHANG, R. Multivariate analysis of homogeneous nucleation rate measurements. Nucleation in the p-toluic acid/sulfuric acid/water system. **The Journal of Chemical Physics**, v. 128, n. 6, 2008.

[37] JIMENEZ, J. L. *et al*. Evolution of organic aerosols in the atmosphere. **Science**, v. 326, n. 5959, p. 1525–1529, 2009.

[38] ZHANG, R. *et al*. Formation of nanoparticles of blue haze enhanced by anthropogenic pollution. **Proceedings of the National Academy of Sciences of the United States of America**, v. 106, n. 42, p. 17650-17654, 2009.

[39] METZGER, A. *et al*. Evidence for the role of organics in aerosol particle formation under atmospheric conditions. **Proceedings of the National Academy of Sciences of the United States of America**, v. 107, n. 15, p. 6646-6651, 2010.

[40] SCHOBESBERGER, S. JUNNINEN, H. BIANCHI, F. *et al*. Molecular understanding of atmospheric particle formation from sulfuric acid and large oxidized organic

molecules. **Proceedings of the National Academy of Sciences**, v. 110, n. 43, p. 17223-17228, 2013.

[41] RICCOBONO, F. *et al*. Oxidation products of biogenic emissions contribute to nucleation of atmospheric particles. **Science**, v. 344, n. 6185, p.717-721, 2014.

[42] SELLEGRI, K.; HANKE, M.; UMANN, B.; ARNOLD, F.; KULMALA, M. Measurements of organic gases during aerosol formation events in the boreal forest atmosphere during QUEST. **Atmospheric Chemistry and Physics**, v. 5, p. 373–384, 2005.

[43] RIIPINEN, I., *et al*. The contribution of organics to atmospheric nanoparticle growth. **Nature Geoscience**, v. 5, n. 7, p. 453-458, 2012.

[44] DONAHUE, N. M., *et. al*. How do organic vapors contribute to new-particle formation? **Faraday Discuss**, v. 165, p. 91–104, 2013.

[45] EHN, M., *et. al*. A large source of low-volatility secondary organic aerosol. **Nature**, v. 506, p. 476 – 479, 2014.

[46] GE, P., *et al*. Molecular understanding of the interaction of amino acids with sulfuric acid in the presence of water and the atmospheric implication. **Chemosphere**, v. 210, p. 215-223, 2018.

[47] KILDGAARD, J. V. *et al*. Hydration of atmospheric molecular clusters ii: Organic acid–water clusters. **The Journal of Physical Chemistry A**, v. 122, p. 8549-8556, 2018.

[48] TAN, S.; CHEN, X.; YIN, S. Comparison results of eight oxygenated organic molecules: unexpected contribution to new particle formation in the atmosphere, **Atmospheric Environment**, v. 268, p. 118817, 2022.

[49] TROSTL, J. *et. al*. The role of low-volatility organic compounds in initial particle growth in the atmosphere. **Nature**, v. 533, p. 527- 531, 2016.

[50] CHEN, J., *et al*. Interaction of oxalic acid with dimethylamine and its atmospheric implications. **RSC Advances**. v. 7, n. 11, p. 6374-6388, 2017.

[51] LIN, Y., *et. al*. Interaction between dicarboxylic acid and sulfuric acid-base clusters enhances new particle formation. **Atmospheric Chemistry and Physics**, v. 19, n. 12, p. 1–46, 2018.

[52] PENG, X-Q.; LIU, Y-R.; HUANG T.; JIANG, S.; HUANG, W. Interaction of gas phase oxalic acid with ammonia and its atmospheric implications. **Physical Chemistry Chemical Physics**, v. 17, n. 14, p. 9552–9563, 2015.

[53] SCHNITZLER, E. G.; JÄGER, W. The benzoic acid–water complex: A potential atmospheric nucleation precursor studied using microwave spectroscopy and ab initio calculations. **Physical Chemistry Chemical Physics**, v. 16, n. 6, p. 2305-2314, 2014.

[54] WANG, H., *et. al*. A molecular understanding of the interaction of typical aromatic acids with common aerosol nucleation precursors and their atmospheric implications, **RSC Advances**, v. 9, n. 42, p. 36171-36181, 2019.

[55] LI, Y.; ZHANG, H.; ZHANG, Q.; XU, Y.; NADYKTO, A. B. Interactions of sulfuric acid with common atmospheric bases and organic acids: Thermodynamics and implications to new particle formation, **Journal of Environmental Sciences**, v. 95, p. 130-140, 2020.

[56] LEE, X., *et al*. Underrated primary biogenic origin and lifetime of atmospheric formic and acetic acid. **Scientific Reports**, v. 11, p. 7176, 2021.

[57] LIU, J. Y.; LONG, Z. W.; MITCHELL, E.; LONG, B. New Mechanistic Pathways for the Reactions of Formaldehyde with Formic Acid Catalyzed by Sulfuric Acid and Formaldehyde with Sulfuric Acid Catalyzed by Formic Acid: Formation of Potential Secondary Organic Aerosol Precursors. **ACS Earth Space Chemistry**, v. 5, p. 1363–1372, 2021.

[58] HODSHIRE, A. L.; *et. al*. The potential role of methanesulfonic acid (MSA) in aerosol formation and growth and the associated radiative forcings**. Atmospheric Chemistry and Physics**, v. 19, p. 3137-3160, 2019.

[59] ZHAO, H.; JIANG, X.; DU, L. Contribution of methane sulfonic acid to new particle formation in the atmosphere. **Chemosphere**, v. 174, p. 689-699 (2017).

[60] GONÇALVES, D. S.; CHAUDHURI, P. Atmospherically relevant hydrogen-bonded interactions between methanesulfonic acid and H2SO4 clusters: A computational study. **The Journal of Physical Chemistry A**, v. 124, p. 11072-11085, 2020.

[61] XU, J.; FINLAYSON-PITTS, B. J.; GERBER, R. B. Proton transfer in mixed clusters of methanesulfonic acid, methylamine, and oxalic acid: Implications for atmospheric particle formation**. The Journal of Physical Chemistry A**, v. 121, p. 2377-2385, 2017.

[62] CHEN, D.; WANG, W.; LI, D. W. WANG, W. Atmospheric implication of synergy in methanesulfonic acid–base trimers: A theoretical investigation. **RSC Advances**, v. 10, p. 5173–5182, 2020.

[63] BORK, N.; ELM, J.; OLENIUS, T.; VEHKAMAKI, H. Methane Sulfonic Acid-Enhanced Formation of Molecular Clusters of Sulfuric Acid and Dimethyl Amine. **Atmospheric Chemistry and Physics**, v. 14, p. 12023-12030, 2014.

[64] LI, H.; KUPIAINEN-MÄÄTTÄ, O.; ZHANG, H.; ZHANG, X.; GE, M. A molecular-scale study on the role of lactic acid in new particle formation: Influence of relative humidity and temperature, **Atmospheric Environment**, v. 166, p. 479-487, 2017.

[65] YANG, Y.; LIU, L.; WANG, H.; ZHANG. X. Molecular-Scale Mechanism of Sequential Reaction of Oxalic Acid with SO3: Potential Participator in Atmospheric Aerosol Nucleation. **The Journal of Physical Chemistry A**, v. 125, p. 4200-4208, 2021.

[66] WEBER, K. H.; MORALES, F. J.; TAO, F. Theoretical study on the structure and stabilities of molecular clusters of oxalic acid with water. **The Journal of Physical Chemistry A**, v. 116, n. 47, p. 11601–17, 2012.

[67] XU, W.; ZHANG, R. Theoretical investigation of interaction of dicarboxylic acids with common aerosol nucleation precursors**. The Journal of Physical Chemistry A**, v. 116, n. 18, p. 4539–4550, 2012.

[68] ARUNAN, E. DESIRAJU, G. R. KLEIN, R. A. *et al*. Definition of the hydrogen bond (IUPAC Recommendations), **Pure and Applied Chemistry**, v. 83, n. 8, p. 1637-1641, 2011.

[69] JEFFREY, G. A. An Introduction to Hydrogen Bond. Oxford University Press, 1997.

[70] PARR, R.; W. YANG, W. Density-functional theory of the electronic structure of molecules, **Annual review of physical chemistry**, v. 46, n. 1, p. 701-728, 1995.

[71] HOHENBERG, P.; KOHN, W., Inhomogeneous electron gas. **Physical Review**, v. 136, n. 3B, p. B864, 1964.

[72] KOHN, W.; SHAM, L. J., Self-consistent equations including exchange and correlation effects. **Physical Review**, v. 140, n. 4A, p. A1133, 1965.

[73] PERDEW, J. P.; BURKE, K.; ERNZERHOF, M., Generalized gradient approximation made simple. **Physical Review Letters**, v. 77, n. 18, p. 3865; 1996.

[74] YANG, W., PARR, R. G.; LEE, C., Various functionals for the kinetic energy density of an atom or molecule. **Physical Review A**, v. 34, n. 6, p. 4586, 1986.

[75] MARDIROSSIAN, N.; HEAD-GORDON, M. Thirty years of density functional theory in computational chemistry: an overview and extensive assessment of 200 density functionals. **Molecular Physics**, v. 115, n. 19, p. 2315, 2017.

[76] ZHAO, Y.; TRUHLAR, D. G. The M06 suite of density functionals for main group thermochemistry, thermochemical kinetics, noncovalent interactions, excited states, and transition elements: two new functionals and systematic testing of four M06-class functionals and 12 other functionals. **Theoretical Chemistry Accounts**, v. 120, n. 1-3, p. 215, 2008.

[77] SZABO, A.; OSTLUND, N., Modern Quantum Chemistry, Introduction to Advanced Electronic Structure Theory, Courier Corporation, 1996.

[78] JENSEN, F. Introduction to computational chemistry. John Wiley & Sons, 2017.

[79] HEHRE, W. J. Ab initio molecular orbital theory. **Accounts of Chemical Research**, v. 9, n, 11, p. 399-406, 1976.

[80] MARTIN, R. M., Electronic structure: basic theory and practical methods. Cambridge University Press, 2020.

[81] SLATER, J. C.; PHILLIPS, J. C. Quantum theory of molecules and solids vol. 4: the self-consistent field for molecules and solids. **Physics Today**, v. 27, n. 12, p. 49-50, 1974.

[82] DUNNING, T. H., Gaussian basis sets for use in correlated molecular calculations. I. The atoms boron through neon and hydrogen. **The Journal of Chemical Physics**, v. 90, n. 2, p.1007-1023, 1989.

[83] KENDALL, R. A., DUNNING, T. H.; HARRISON, R. J., Electron affinities of the first-row atoms revisited. Systematic basis sets and wave functions. **The Journal of Chemical Physics**, v. 96, n. 9, p.6796-6806, 1992.

[84] ELM, J.; MIKKELSEN, K.V. Computational approaches for efficiently modelling of small atmospheric clusters. **Chemical Physics Letters**, v. 615, p. 26-29, 2014.

[85] ELM, J.; BILDE, M.; MIKKELSEN, K. V. Assessment of binding energies of atmospherically relevant clusters. **Physical Chemistry Chemical Physics**, v. 15, n. 39, p. 16442-16445, 2013.

[86] ELM, J.; BILDE, M.; MIKKELSEN K. V. Assessment of Density Functional Theory in Predicting Structures and Free Energies of Reaction of Atmospheric Prenucleation Clusters. **Physical Chemistry Chemical Physics**, v. 8, n. 6, p. 2071-2077, 2012.

[87] HUFF, A. K.; MACKENZIE, R. B.; SMITH, C. J.; LEOPOLD, K. R. A Perfluorinated Carboxylic Sulfuric Anhydride: Microwave and Computational Studies of CF_3COOSO_2OH. **The Journal of Chemical Physics A**, v. 123, n. 11, p. 2237-2243, 2019.

[88] LV, G.; SUN, X.; ZHANG, C.; LI, M. Understanding the catalytic role of oxalic acid in SO3 hydration to form H2SO4 in the atmosphere, **Atmospheric Chemical Physics**, v. 19, n. 8, p. 2833–2844, 2019.

[89] MAÇÔAS, E. M. S.; FAUSTO, R.; PETTERSSON, M.; KHRIACHTCHEV, L.; RASANEN, M. Infrared-Induced Rotamerization of Oxalic Acid Monomer in Argon Matrix. **The Journal of Chemical Physics A**, v. 104, n. 30, p. 6956, 2000.

[90] GODFREY, P. D.; MIRABELLA, M. J.; BROWN, R. D. Structural Studies of Higher Energy Conformers by Millimeter-Wave Spectroscopy: Oxalic Acid. **The Journal of Chemical Physics A**, v. 104, n. 2, p. 258, 2000.

[91] BUEMI, G. DFT study of the hydrogen bond strength and IR spectra of formic, oxalic, glyoxylic and pyruvic acids in vacuum, acetone and water solution. **Journal of Physical Organic Chemistry**, v. 22, n. 10, p. 933–947, 2009.

[92] FELLER, D.; BROSS, D. H.; RUSCIC, B. Enthalpy of Formation of C2H2O4 (Oxalic Acid) from High-Level Calculations and the Active Thermochemical Tables Approach. **The Journal of Physical Chemistry A**, v. 123, n. 16, p. 3481−3496, 2019.

[93] CHEN, C.; SHYU, S.-F. Conformers and intramolecular hydrogen bonding of the oxalic acid monomer and its anions. **International Journal of Quantum Chemistry**, v. 76, n. 4, p. 541–551, 2000.

[94] ALSENOY, C. V.; KLIMKOWSKI, V. J.; SCHAFER, L. Structural and conformational investigations of the dicarbonyls glyoxal, biacetyl and oxalic acid. **Journal of Molecular Structure: THEOCHEM**, v. 109, n. 3-4, p. 321-330, 1984.

[95] MOHAJERI, A.; SHAKERIN, N. The gas-phase acidity and intramolecular hydrogen bonding in oxalic acid**. Journal of Molecular Structure: THEOCHEM**, v. 711, n. 1-3, p. 167, 2004.

[96] HERMIDA-RAMÓN, J. M.; CABALEIRO-LAGO, E. M.; RODRÍGUEZ-OTERO, J. Computational study of the dissociation of oxalic acid in water clusters. **Chemical Physics**, v. 302, n. 1-3, p. 53–60, 2004.

[97] CHANG, J. G.; CHEN, H. T.; XU, S. C.; LIN, M. C. Computational Study on the Kinetics and Mechanisms for the Unimolecular Decomposition of Formic and Oxalic Acids. **The Journal of Physical Chemistry A**, v. 111, n. 29, p. 6789, 2007.

[98] HIGGINS, J.; ZHOU, X.; LIU, R.; Huang T. T.-S. Theoretical Study of Thermal Decomposition Mechanism of Oxalic Acid. **The Journal of Physical Chemistry A**, v. 101, n. 14, p. 2702-2708, 1997.

[99] DENNINGTON, R. D.; KEITH, T. A.; MILLAM, J. M. GaussView 5.0. 9; Gaussian Inc.: Wallingford, CT, USA, 2008.

[100] FRISCH, M. J. ; TRUCKS, G. W.; SCHLEGEL, H. B.; *et al*. Gaussian 16, Rev. C.01, Gaussian, Inc.: Wallingford, CT, USA, 2016.

[101] KUBEČKA, J.; BESEL, V.; KURTÉN, T.; MYLLYS, N.; VEHKAMÄKI, H. Configurational sampling of noncovalent (atmospheric) molecular clusters: Sulfuric acid and guanidine. **The Journal of Physical Chemistry A**, v. 123, n. 28, p. 6022–6033, 2019.

[102] PARTANEN, L.; VEHKAMÄKI, H.; HANSEN, K.; *et al*. Effect of Conformers on Free Energies of Atmospheric Complexes. **The Journal of Physical Chemistry A**, v. 120, n. 43, p. 8613–8624, 2016.

[103] FILETI, E. E.; RIVELINO, R.; CANUTO, S. Rayleigh light scattering of hydrogen bonded clusters investigated by means of ab initio calculations. **Journal of Physics B: Atomic, Molecular and Optical Physics**, v. 36, n. 2, p. 399-408, 2003.

[104] CHAUDHURI, P., CANUTO, S. Rayleigh scattering properties of small polyglycine molecules. **Journal of Molecular Structure**, v. 760, n. 1-3, p. 15-20, 2006.

[105] DA SILVA, A. M.; CHAKRABORTY, S.; CHAUDHURI, P. Rayleigh light scattering from hydrogen-bonded dimers of small astrophysical molecules. **International Journal of Quantum Chemistry**, v. 112, n. 16, p. 2822-2827, 2012.

[106] ELM, J.; NORMAN, P.; BILDE, M.; MIKKELSEN, K. V. Computational study of the Rayleigh light scattering properties of atmospheric prenucleation clusters. **Physical Chemistry Chemical Physics.** v. 16, p. 10883-10890, 2014.

[107] HUANG, X.; HU, M.; HE, L.; TANG, X. Chemical characterization of water-soluble organic acids in PM in Beijing, China. **Atmospheric Environment**, v. 2015, n. 39, p. 2819–2827, 2005.

[108] WAGNER, R.; MÖHLER, O.; SAATHOFF, H.; SCHNAITER, M.; LEISNER, T. High variability of the heterogeneous ice nucleation potential of oxalic acid dihydrate and sodium oxalate. **Atmospheric Chemical Physics**, v. 10, p. 7617–7641, 2010.

[109] XU, Y.; Nadykto, A. B.; YU, F.; JIANG, L.; WANG, W. Formation and properties of hydrogen-bonded complexes of common organic oxalic acid with atmospheric nucleation precursors. **Journal of Molecular Structure: THEOCHEM**, v. 951, p. 28–33, 2010.

[110] XU, W.; ZHANG, R. Theoretical investigation of interaction of dicarboxylic acids with common aerosol nucleation precursors**. The Journal of Physical Chemistry A**, v. 116, n. 18, p. 4539–4550, 2012.

[111] WEBER, K. H.; MORALES, F. J.; TAO, F. Theoretical study on the structure and stabilities of molecular clusters of oxalic acid with water. **The Journal of Physical Chemistry A**, v. 116, n. 47, p. 11601–17, 2012.

[112] WEBER, K.H.; LIU, Q.; TAO, F-M. Theoretical study on stable small clusters of oxalic acid with ammonia and water. **The Journal of Physical Chemistry A**, v. 118, n. 8, p. 1451–1468, 2014.

[113] PENG, X-Q.; LIU, Y-R.; HUANG T.; JIANG, S.; HUANG, W. Interaction of gas phase oxalic acid with ammonia and its atmospheric implications. **Physical Chemistry Chemical Physics**, v. 17, n. 14, p. 9552–9563, 2015.

[114] MIAO, S-K.; JIANG, S.; CHEN, J.; MA, Y.; ZHU, Y-P.; WEN, Y. et al. Hydration of a sulfuric acid-oxalic acid complex: acid dissociation and its atmospheric implication. **RSC Advances**, v. 5, n. 60, p. 48638–48646, 2015.

[115] PAVULURI, C. M.; KAWAMURA, K.; MIHALOPOULOS, N.; SWAMINATHAN, T. Laboratory photochemical processing of aqueous aerosols: Formation and degradation of dicarboxylic acids, oxocarboxylic acids and α- dicarbonyls. **Atmospheric Chemical Physics**, v. 15, n. 14, p. 7999–8012, 2015.

[116] WANG, G.; CHENG, C.; MENG, J.; HUANG, Y.; LI, J.; REN, Y. Field observation on secondary organic aerosols during Asian dust storm periods: Formation mechanism of oxalic acid and related compounds on dust surface. **Atmospheric Environment**, v.113, p. 169–176, 2015.

[117] KAWAMURA, K.; BIKKINA, S. A review of dicarboxylic acids and related compounds in atmospheric 424 aerosols: Molecular distributions, sources and transformation, **Atmospheric Research**, v. 170, p. 140-160, 2016.

[118] PENG, X-Q.; HUANG, T.; MIAO, S-K.; *et al*. Hydration of oxalic acid–ammonia complex: atmospheric implication and Rayleigh-scattering properties. **RSC Advances**, v. 6, p. 46582–47593, 2016.

[119] ZHAO, H.; ZHANG, Q.; DU, L. Hydrogen bonding in cyclic complexes of carboxylic acid–sulfuric acid and their atmospheric implications. **RSC Advances**, v. 6, p. 71733–71743 (2016).

[120] ELM, J.; MYLLYS, N.; KURTÉN, T. What is required for highly oxidized molecules to form clusters with sulfuric acid? **The Journal of Physical Chemistry A**, v. 121, p. 4578–87, 2017.

[121] HU. Y-C.; ZHANG, X-H.; LI, Q-S.; ZHANG, Y-H.; LI, Z-S. Effect of water on the structure and stability of hydrogen-bonded oxalic acid dimer. **ChemPhysChem**. v. 18, p. 3375–3383, 2017.

[122] XU, J.; FINLAYSON-PITTS, B. J.; GERBER, R. B. Proton transfer in mixed clusters of methanesulfonic acid, methylamine, and oxalic acid: implications for atmospheric particle formation. **The Journal of Physical Chemistry A**, v. 121, p. 2377–2385, 2017.

[123] CHEN, J.; JIANG, S.; LIU, Y-R.; HUANG, T.; WANG, C-Y.; MIAO, S-K. et al. Interaction of oxalic acid with dimethylamine and its atmospheric implications. **RSC Advances**, v. 7, p. 6374–6388, 2017.

[124] ARQUERO, K. D.; XU. J.; GERBER, B.; FINLAYSON-PITTS, B. J. Particle formation and growth from oxalic acid, methanesulfonic acid, trimethylamine and water: a combined experimental and theoretical study. **Physical Chemistry Chemical Physics**, v. 19, p. 28286–28301, 2017.

[125] HONG, Y.; LIU, Y-R.; WEN, H.; MIAO, S-K.; HUANG, T.; PENG, X-Q. *et al*. Interaction of oxalic acid with methylamine and its atmospheric implications. **RSC Advances**, v. 8, p. 7225–7234, 2018.

[126] BOREDDY, S. K. R.; KAWAMURA, K. Investigation on the hygroscopicity of oxalic acid and atmospherically relevant oxalate salts under sub- and supersaturated conditions. **Environmental Science: Processes & Impacts**, v. 20, p. 1069–1080, 2018.

[127] DESHMUKH, D. K.; KAWAMURA, K.; GUPTA, T. *et al*. High Loadings of Water-soluble Oxalic Acid and Related Compounds in PM2.5 Aerosols in Eastern Central India: Influence of Biomass Burning and Photochemical Processing, **Aerosol and Air Quality Research**, v. 19, p. 2625–2644, 2019.

[128] ZHAO, Y.; LIU, Y-R.; JIANG, S.; *et al*. Theoretical analysis of sulfuric acid–dimethylamine acid-based ternary homogeneous nucleation: the important role of synergistic effect. **Atmospheric Environment**, v. 233, p. 117609, 2020.

[129] CHEN, J. Theoretical analysis of sulfuric acid–dimethylamine–oxalic acid–water clusters and implications for atmospheric cluster formation, **RSC Advances**, v. 12, p. 2242, 2022.

[130] PALMIERI, F.; ESTOPPEY, A.; HOUSE, G. L. *et al*. Oxalic acid, a molecule at the crossroads of bacterial-fungal interactions. **Advances in Applied Microbiology**, v. 106, p. 49–77, 2019.

[131] RUDNICK, M. B.; VEEN, J. A.; BOER, W. Oxalic acid: A signal molecule for fungus feeding bacteria of the genus Collimonas? **Environmental Microbiology Reports**, v. 7, p. 709–714, 2015.

[132] HSIEH, L.; CHEN, C.; WAN, M.; TSAI, C.; TSAI, Y. Speciation and temporal characterization of dicarboxylic acids in PM2.5 during a PM episode and a period of non-episodic pollution, **Atmospheric Environment**, v. 42, p. 6836−6850, 2008.

[133] RADEK, M.; SAVAGE, G.P. Oxalates in Some Indian Green Leafy Vegetables. **International Journal of Food Sciences and Nutrition**, v. 59, p. 246–260, 2008.

[134] HOLMES, R. P.; KENNEDY, M. Estimation of the Oxalate Content of Foods and Daily Oxalate Intake. **Kidney International**, v. 57, p. 1662–1667, 2000.

[135] SALGADO, N.; SILVA, M.A.; FIGUEIRA, M.E.; COSTA, H.S.; ALBUQUERQUE, T.G. Oxalate in Foods: Extraction Conditions, Analytical Methods, Occurrence, and Health Implications**. Foods**, v. 12, n. 17, p. 3201, 2023.

[136] SIENER, R.; SEIDLER, A.; HÖNOW, R. Oxalate-rich foods, **Food Science and Technology, Campinas**, v. 41, p. 169-173, 2021.

[137] MOCHIZUKI, Tomoki, *et al*. Secondary formation of oxalic acid and related organic species from biogenic sources in a larch forest at the northern slope of Mt. Fuji. **Atmospheric Environment**, v. 166, p. 255-262, 2017.

[138] CLAEYS, M. *et al*. Formation of secondary organic aerosols through photooxidation of isoprene. **Science**, v. 303, p. 1173-1176, 2004.

[139] KAWAMURA K.; IKUSHIMA K. Seasonal changes in the distribution of dicarboxylic acids in the urban atmosphere. **Environmental Science & Technology**, v. 27, p. 2227–2235, 1993.

[140] PRENNI, A. J.; DEMOTT, P. J.; KREIDENWEIS, S. M.; SHERMAN, D. E.; RUSSELL, L. M.; MING, Y. The effects of low molecular weight dicarboxylic acids on cloud formation**. The Journal of Physical Chemistry A**, v. 105, n. 50, p. 11240–11248, 2001.

[141] MAKAR, P.A. The estimation of organic gas vapour pressure. **Atmospheric Environment**, v. 35, n. 5, p. 961–974, 2001.

[142] LIMBECK, A.; PUXBAUM, H.; OTTER, L.; SCHOLES, M. C. Semivolatile behavior of dicarboxylic acids and other polar organic species at a rural background site (Nylsvley, RSA). **Atmospheric Environment**, v. 35, n. 10, p. 1853–1862, 2001.

[143] KHWAJA H. A. Atmospheric concentrations of carboxylic acids and related compounds at a semiurban site. **Atmospheric Environment**, v. 29, p. 127–39, 1995.

[144] CHEBBI, A.; CARLIER, P. Carboxylic acids in the troposphere, occurrence, sources, and sinks: A review. **Atmospheric Environment**, v. 30, n. 24, p. 4233–4249, 1996.

[145] MARTINELANGO, P. K.; DASGUPTA, P. K.; AL-HORR, R. S. Atmospheric production of oxalic acid/oxalate and nitric acid/nitrate in the Tampa Bay airshed: Parallel pathways. **Atmospheric Environment**, v. 41, n. 20, p. 4258–4269, 2007.

[146] MA, X.; SUN, Y.; HUANG, Z.; ZHANG, Q.; WANG, W. A density functional theory study of the molecular interactions between a series of amides and sulfuric acid, **Chemosphere**, v. 214, p. 781-790, 2019.

[147] SIPILA, M. BERNDT, T. PETAJA, T. *et al*. The role of sulfuric acid in atmospheric nucleation. **Science**, v. 327, n. 5970, p. 1243-1246, 2010.

[148] ZHENG, J.; MA, Y.; CHEN, M. *et al.* Measurement of atmospheric amines and ammonia using the high-resolution time-of-flight chemical ionization mass spectrometry. **Atmospheric Environment**, v. 102, p. 249–259, 2015.

[149] NAIR, A. A.; YU, F. Quantification of Atmospheric Ammonia Concentrations: A Review of Its Measurement and Modeling. **Atmosphere**, v. 11, n. 10, p. 1092, 2020.

[150] ELM, J. An Atmospheric Cluster Database Consisting of Sulfuric Acid, Bases, Organics, and Water. **A. C. S. Omega**, v. 4, n. 6, p. 10965- 10974, 2019.

[151] LEE, S.-H.; GORDON, H.; YU, H.; *et al*. New particle formation in the atmosphere: From molecular clusters to global climate. **Journal of Geophysical Research: Atmospheres**, v. 124, n. 13, p. 7098–7146, 2019.

[152] NAHLOVSKA, Z.; NAHLOVSKY, B.; STRAND, T. G. Molecular Structure of Gaseous Oxalic Acid from Electron Diffraction and IR Data. **Acta Chemica Scandinavica**, v. 24, n. 7, p. 2617, 1970.

[153] REDINGTON, R. L.; REDINGTON, T. E. Infrared Matrix-Isolation Spectra of Monomeric Oxalic Acid. **Journal of Molecular Structure**, v. 48, n. 2, p. 165, 1978.

[154] BACK, R. A. The ultraviolet absorption spectrum of oxalic acid vapor. **Canadian Journal of Chemistry**, v. 62, n. 8, p. 1414, 1984.

[155] NIEMINEN, J.; RASANEN, M.; MURTO, J. Matrix Isolation and ab Initio Studies of Oxalic Acid. **The Journal of Physical Chemistry A**, v. 96, n. 13, p. 5303, 1992.

[156] ZHAO, Y.; LIU, Y-R.; JIANG, S.; *et al*. Volatile organic compounds enhancing sulfuric acid-based ternary homogeneous nucleation: the important role of synergistic effect. **Atmospheric Environment**, v. 233, p. 117609, 2020.